Allosteric Disordering of eIF2B Regulates the Integrated Stress Response

Udit Dalwadi[1]¶, Advait Subramanian[1]¶, Aniliese Deal[1], Julia E. Conrad[1], Meera Venkatesh[1], Morgane Boone[1], Pascal F. Egea[1], Lingjie He[1], Nimit Jain[1], D. John Lee[2], Yuwei Liu[1], Lucas C. Reineke[1], Kazuki Saito[1], Nathaniel Talledge[1], Hannah Toutkoushian[1], Maxence Le Vasseur[1], Francesca Zappa[1], Raoul J. de Groot[4], Diego Acosta-Alvear[1], Christopher P. Arthur[2], Jodi Nunnari[1], Mauro Costa-Mattioli[1], James J. Crawford[3], Frank J. M. van Kuppeveld[4], Tristan I. Croll[5], Peter Walter[1]*, Adam Frost[1]*

[1] Institute of Science, Altos Labs, Redwood City, CA, USA

[2] Institute of Technology, Altos Labs, Redwood City, CA, USA

[3] Institute of Medicine, Altos Labs, Redwood City, CA, USA

[4] Virology Division, Department of Infectious Diseases and Immunology, Faculty of Veterinary Medicine, Utrecht University, Utrecht, the Netherlands

[5] Institute of Computation, Altos Labs, Cambridge, UK

*Corresponding authors

E-mail: afrost@altoslabs.com (AF), pwalter@altoslabs.com (PW)

¶These authors contributed equally to this work

Abstract

The ternary complex (TC), composed of translation initiation factor eIF2, GTP, and initiator methionyl tRNA, delivers the first amino acid to the ribosome to initiate protein synthesis. The activity of the decameric eukaryotic initiation factor 2B complex (eIF2B) initiates TC assembly by catalyzing GDP to GTP exchange on eIF2, thereby setting the TC levels in the cell. Stress-induced phosphorylation converts eIF2 from the substrate of the GDP/GTP exchange reaction into an inhibitor (eIF2-P) of eIF2B. This conversion reduces the cell's TC levels and induces the widespread reprogramming of translation known as the Integrated Stress Response (ISR). Here, we chart an allosteric axis running through eIF2B, revealing the importance of a protrusive α-helix in its β-subunit, the 'latch-helix', that locks onto the α-subunit to induce eIF2B activity. eIF2-P binding unhooks the latch-helix, opening eIF2B, which inhibits its GDP/GTP exchange activity. Distinct viral proteins have convergently evolved to bind to eIF2Bα and stabilize the latch-helix-bound active state. Using these insights, we generated ISR-ACTivating compounds, ISRACTs, that stabilize eIF2B in its inhibited, unlatched state. Our study thus highlights how state-transitions in eIF2B are regulated via long-range allostery.

Introduction

The eukaryotic translation initiation factor 2B (eIF2B) is a guanine nucleotide exchange factor (GEF) and gatekeeper of protein synthesis. It is a complex comprised of two tetramers containing the β-, γ-, δ-, and ε-subunits that further assemble into a decamer by binding the homodimeric α-subunit (*1–5*). When fully assembled, the eIF2B decamer catalyzes GDP ejection from its substrate, the heterotrimeric eukaryotic initiation factor 2 (eIF2; composed of α-, β-, and γ-subunits) (*4–7*), allowing for GTP binding to eIF2γ.

By catalyzing eIF2 nucleotide exchange, eIF2B facilitates the formation of the eIF2-GTP-methionyl-initiator tRNA "Ternary Complex" (TC). TC formation is a prerequisite for mRNA translation initiation as it delivers the first aminoacyl-tRNA to 40S ribosomal subunits scanning for AUG initiation codons (*8–12*). Stress-inducing perturbations, such as viral infection (*13*, *14*), ribosome stalling and collisions (*15*, *16*), secretory protein folding (*17*, *18*) and trafficking imbalances (*19*), redox changes (*20*, *21*), mitochondrial dysfunction (*22*, *23*), hypoxia (*24*, *25*), and amino acid/nutrient deficiencies (*26–32*), cause the activation of any of four eIF2 kinases (PKR, GCN2, PERK, and HRI). These kinases all phosphorylate eIF2α at a single site, serine 51, producing eIF2-P – a potent eIF2B inhibitor. This conversion of eIF2B's substrate, eIF2, into its inhibitor, eIF2-P, is the hallmark of the Integrated Stress Response (ISR) (*7*, *21*, *33–37*). As eIF2-P accumulates, TC levels diminish, which leads to a decline in translation initiation rates for all AUG-initiated transcripts.

While the ISR is characterized by a decline in general translation, a subset of transcripts with inhibitory upstream open reading frames (uORFs) are translated at higher rates, leading to enhanced accumulation of their protein products (*31*, *38–41*), such as the transcriptional activator *ATF4* (*39*, *42*, *43*). The translation of these uORF-containing transcripts and the resulting transcriptomic changes enable cells to adapt to and counteract the stressful perturbation (*39*, *44–47*). This broad reprogramming of protein synthesis rates is typically cytoprotective (*48*, *49*), but chronic activation of the ISR can become maladaptive and is associated with pathologies that include leukodystrophy

(*50–54*), cancer (*24*, *55–57*), and cognitive impairments caused by Alzheimer's disease (*58–62*), traumatic brain injuries (*63*), and Down syndrome (*64*).

In these disease contexts, the drug-like small molecule ISRIB (*41*, *49*) and its clinical derivatives maintain protein synthesis rates despite elevated eIF2-P levels. Mechanistically, ISRIB binds to eIF2B in a two-fold symmetric pocket formed at the interface between two eIF2Bβ and two eIF2Bδ subunits proximal to the substrate eIF2 binding site. In doing so, ISRIB stabilizes the active "A"-state of the eIF2B decamer (*4*, *5*, *65–67*). The A-state is defined, in part, by the distance between the β- and δ-subunits from opposing tetramers. When the cleft between these subunits is ~32 Å wide, the α-subunit of eIF2 binds favorably and this positions the GDP-bound γ-subunit over the catalytic eIF2B ε-subunit to drive nucleotide exchange. The inactive "I"-state of eIF2B is induced by eIF2-P binding, which occurs at a distinct allosteric site between the α- and δ-subunits more than 40 Å away from the ISRIB and eIF2 binding sites (*36*, *37*). The I-state is characterized by widening of the eIF2α binding pocket to ~35 Å, reducing substrate binding affinity and guanine nucleotide exchange (*65*, *66*).

ISRIB thus renders eIF2B resistant to inhibition by eIF2-P through allosteric stabilization of the A-state (*65–67*). Although there are no known endogenous or exogenous ligands that engage the ISRIB pocket, viruses inhibit the ISR via effector proteins that engage at other sites on eIF2B (*68–71*). Viral suppression of the ISR promotes synthesis of viral proteins despite activation of the innate sensors that lead to eIF2α phosphorylation (*13*, *14*). The best-characterized example to date comes from studies of the Sandfly fever Sicilian virus (SFSV) protein, NSs (*68–70*). NSs binds to eIF2B at a site that overlaps with the eIF2-P inhibitor binding site, thereby sterically blocking eIF2-P binding. However, rather than inducing the I-state as eIF2-P does, it allosterically promotes the A-state conformation (*67*, *69*, *70*).

These observations inform current models of how eIF2-P activates a long-range allosteric change through the eIF2B core to regulate eIF2B GEF activity, including the discovery of the eIF2Bδ subunit's fulcrum-helix, which acts as a switch for propagating

104 changes in the angle between the eIF2Bα and eIF2Bδ subunits (*67*). However, our
105 understanding of how information is relayed between the site of eIF2-P inhibitor binding,
106 the site of substrate binding, and the ISRIB-binding pocket in eIF2B is incomplete.
107 Furthermore, how diverse eIF2B ligands—including pharmaceuticals and pathogen
108 effector proteins—influence allosteric chain linkage despite their disparate and distant
109 binding sites remains poorly understood. Using structural, biochemical and
110 pharmacological approaches, we map the axis of coupled allosteric changes that
111 transmits information over the 40 Å distance between eIF2B's diverse binding sites. Our
112 analyses reveal a remarkable convergence in viral evolution where unrelated viruses
113 utilize dissimilar proteins to stabilize the A-state of eIF2B. We leverage the new
114 structural understanding of allosteric eIF2B regulation to develop small molecules,
115 ISRACTs, that target the ISRIB binding pocket to activate, rather than inhibit, the ISR.

Results

A short α-helix in eIF2Bβ allosterically competes with eIF2α-P binding

To gain mechanistic understanding of the conformational dynamics that govern eIF2B activity, we segmented and classified 569,415 single-particle cryo-EM images of eIF2B in its apo-form and subjected the images to 3D variability analysis (3DVA) (Table 1). Visualization of 3DVA highlighted motion trajectories of eIF2B consistent with the particle distributions (Fig. S1 and Movie S1). The trajectories included (1) the A- to I-state opening of the eIF2 substrate binding pocket between the two eIF2Bβγδε tetramers (Fig. 1A; Motion 1), (2) rotation of eIF2Bα away from eIF2Bβ/δ (Motion 2), and (3) swiveling of the eIF2Bγ beta-solenoid domains perpendicular to the tetramer rocking motion (Motion 3).

To estimate the probability of particle distribution within these states, and thus the energy barriers associated with conformational transitions, we performed heterogeneous 3D classification of all particles into 10 classes. This procedure yielded 8 distinct reconstructions and 2 noise classes. Unexpectedly, we found that ~10% of the particles yielded eIF2B completely in the I-state conformation, with (i) the substrate interfaces as far apart as eIF2-P bound eIF2B (distance of 35.5 Å versus 32.5 Å observed in the substrate-bound A-state, Fig. 1B-C), (ii) the ISRIB-binding pocket lengthened by 4.3 Å (Fig. S2A), (iii) the eIF2Bδ “fulcrum-helix”, or switch-helix (*67*), positioned in its rotational I-state (Fig. S2B), and (iv) the tetramer-tetramer interface histidine βH160 in its resting I-state-characteristic rotamer position that precludes the A-state-stabilizing interface-zipper interaction (Fig. S2C; Movie S2), as first suggested in an I-state-inducing point mutant, βH160D (*72*).

Further inspection of the minority I-state fraction of eIF2B revealed missing density for a protrusive α-helix at the tip of eIF2Bβ. In the A-state, this short α-helix, henceforth referred to as the “latch-helix”, bridges eIF2Bβ to eIF2Bα (colored in *cyan*, Fig. 1A, 1C; Movie S1). Density for the latch-helix is absent in reconstructions of the eIF2-P-bound I-state (Fig. 1A - C). These observations suggest that latch-helix binding to eIF2Bα could

147 be a driving force in the inactive (I-) to active (A-) state transition that “locks” eIF2B in
148 the A-state and hence must unhook to allow eIF2B to relax into the I-state. Notably, we
149 observed two 3D classes of eIF2B with defined density for the latch-helix only on one
150 half of the decamer; however, these classes are otherwise in the A-state (Fig. S2D,
151 Table 2). Thus, latch-helix ordering on only one of the two halves of eIF2B is sufficient
152 to drive the I- to A-state transition across the rest of the eIF2B complex.
153
154 The latch-helix comprises eIF2Bβ residues ^{108}SLHKLLT^{114} within a flexible loop linking
155 two helices in the eIF2Bβ core (Fig. 1D). Latch-helix side chains of βL109, βL112, and
156 βL113 nestle into a hydrophobic pocket in eIF2Bα burying a surface area of
157 approximately 623 Å^2. Within the pocket, each latch-helix leucine ‘bump’ occupies a
158 unique ‘hole’ created by the specific orientation of eIF2Bα residues, highlighting the
159 importance of both the hydrophobic effect and geometric complementarity as drivers of
160 this interaction. A reanalysis of published hydrogen-deuterium exchange coupled to
161 mass spectrometry (HDX-MS) data (*67*) confirmed that the latch-helix is more solvent
162 protected in the bound A-state than in the unbound eIF2-P-induced I-state (Fig. S3).
163
164 Comparison of the latch-helix binding pocket in A-state eIF2B (*grey*) with an eIF2α-P-
165 bound I-state eIF2B (*red*) reveals the determinants of eIF2α-P-induced latch-helix
166 release (Fig. 1E). Specifically, the pocket occupied by latch-helix amino acid βL109 is
167 occluded by the C-terminus of eIF2Bα rotating inward to place αL303 in this space. Its
168 position is stabilized by the A- to I-state rearrangement of the adjacent fulcrum-helix
169 (*67*) (Movie S3). The rearrangement of eIF2Bα helices α4 and α5 and rotation of αF75
170 remodels the pocket further and precludes binding of latch-helix amino acids βL112 and
171 βL113. Accordingly, latch-helix and eIF2-P binding are mutually exclusive. Moreover,
172 interaction of eIF2α-P sterically blocks eIF2Bα from adopting the A-state conformation.
173 Together, these structures demonstrate how latch-helix engagement and the linked
174 movements in eIF2Bα govern eIF2B activity.
175

176 **Deletion of the latch-helix deactivates eIF2B allosterically and induces the ISR**
177 Next, we asked how the latch-helix regulates the conformation and catalytic GEF
178 activity of eIF2B. We observed that deletion of the latch-helix (ΔeIF2Bβ$_{100\text{-}116}$, hereafter
179 designated as eIF2B$^{\Delta\text{-latch}}$) resulted in an ~8-fold decrease in eIF2B GEF activity as
180 measured by *in vitro* nucleotide exchange ($t_{1/2}$WT = 2.3 +/- 0.3 min vs. $t_{1/2}$Δ-latch = 18.4
181 +/- 2.4 min) (Fig. 2A). We found no difference in the sedimentation velocity between
182 eIF2B^{WT} and eIF2B$^{\Delta\text{-latch}}$ (Fig. 2B), indicating that the loss of catalytic activity was not
183 due to defective eIF2B decamer assembly. We then assessed how eIF2B$^{\Delta\text{-latch}}$ affects
184 ISR activation *in cellula*. To this end, we depleted endogenous eIF2Bβ with small
185 interfering RNA (siRNA) (Fig. 2C) and expressed siRNA-resistant epitope-tagged
186 *eIF2Bβ^{WT}* or *eIF2Bβ$^{\Delta\text{-latch}}$* (Fig. 2D). In line with the *in vitro* results, eIF2Bβ-depleted cells
187 expressing eIF2Bβ$^{\Delta\text{-latch}}$ exhibited a robust ISR, indicated by ATF4 accumulation,
188 whereas eIF2Bβ^{WT} expressing cells did not (Fig. 2D). Together, the *in vitro* and *in*
189 *cellula* experiments demonstrate that the engagement of the latch-helix is required for
190 optimal eIF2B GEF activity.
191
192 Cryo-EM analysis allowed us to obtain a consensus structure of the eIF2B$^{\Delta\text{-latch}}$
193 decamer at 2.1 Å (Fig. S4A-E). Comparison of the latch-helix binding pocket from this
194 structure to the I-state eIF2α-P-bound eIF2B^{WT} structure showed that eIF2B$^{\Delta\text{-latch}}$ adopts
195 the I-state (Fig. 2E) with eIF2Bα and the eIF2Bδ fulcrum-helix in their characteristic I-
196 state conformations (Fig. S4F). Consequently, the eIF2α substrate binding pocket
197 opens by ~3 Å (Fig. 2F), readily explaining the loss of GEF activity described above
198 (Fig. 2A-D).
199
200 We next 3D-classified the refined particles to probe the conformational spectrum of
201 eIF2B$^{\Delta\text{-latch}}$. Reminiscent of the 3D classification results for the eIF2B^{WT} particles (see
202 Fig. 1C), we found that a small fraction of eIF2B$^{\Delta\text{-latch}}$ particles (~12%) classified into the
203 opposing state (A-like) from the majority consensus (I-state) (Fig. 2F). Contrasting this
204 minor class to a canonical A-state structure, we find that while the hallmarks such as
205 the eIF2α substrate-binding cleft distance and the fulcrum-helix are in an A-state

206 conformation, the latch-helix pocket of eIF2Bα remains in the I-state in the absence of
207 latch-helix engagement (Fig. S4E).
208
209 Importantly, comparison of the eIF2B$^{\Delta\text{-latch}}$ α subunit conformation with multiple crystal
210 structures of eIF2Bα [(*73*, *74*); PDB: 3ECS, 7KMA] shows that eIF2Bα adopts the I-
211 state conformation as its *in crystallo* ground state (Fig. S5C). These observations
212 indicate that eIF2B decamer assembly itself does not induce the A-state unless and
213 until the latch-helix locks onto eIF2Bα. Thus, in the absence of the binding energy
214 provided by the eIF2Bβ latch-helix, eIF2Bα remains in its low-energy ground state. In
215 turn, the ground state of eIF2Bα favors the open and inhibited state of eIF2B, which
216 induces the ISR even in the absence of eIF2-P.
217
218 **Viral effector proteins convergently evolved to suppress the ISR**
219 The results presented so far indicate that during ISR activation, eIF2-P binding
220 promotes unbinding of the eIF2Bβ latch-helix by engaging with eIF2Bα (Fig. 1). By
221 contrast, the Sandfly fever Sicilian virus (SFSV) effector protein NSs hijacks the eIF2-P
222 binding pocket between eIF2Bα and eIF2Bδ (*69*, *70*) but stabilizes an eIF2B A-state,
223 suggesting a conformation complicit with latch-helix ordering. Indeed, inspection of the
224 cryo-EM structures of NSs (*69*, *70*) (EMD-24535, EMD-31472) bound to eIF2B
225 confirmed the presence of an ordered eIF2Bβ latch-helix (Fig. S6).
226
227 We next considered if proteins encoded by other viruses might mimic the mechanism
228 exhibited by SFSV NSs to stabilize the latch-helix-bound state of eIF2Bα and eIF2Bβ to
229 suppress the ISR. For example, the Beluga whale coronavirus accessory protein 10
230 (Bw CoV-AcP10) was shown to bind to eIF2B and compete with eIF2-P (*71*). AcP10,
231 however, shares no sequence similarity with NSs, and the precise mechanism by which
232 it inhibits the ISR remained unknown. To address this knowledge gap, we expressed an
233 N-terminal MBP-tagged version of AcP10 in *E. coli* (Fig. S7A-B) and tested the purified
234 protein to see if it bound to eIF2B directly. Pulldown assays with recombinant eIF2Bα
235 dimers (α_2), eIF2B tetramers (βγδε), or eIF2B decamers $(\alpha\beta\gamma\delta\varepsilon)_2$ *in vitro* indicated that
236 MBP-AcP10 bound directly only to fully assembled eIF2B decamers (Fig. 3A), indicating

237 that a competent AcP10-binding interface requires decamer assembly.
238
239 To determine the interaction interface between AcP10 and eIF2B decamers, we solved
240 a 2.9 Å structure of this complex by cryo-EM (Fig S7). The interface was well-resolved
241 (Fig. 3B, Fig. S7C-F), allowing us to model two molecules of AcP10 bound to eIF2B.
242 Like the structurally unrelated SFSV NSs, AcP10 bound at the eIF2-P binding pockets,
243 forming symmetric interfaces between eIF2Bα and eIF2Bδ on either side of the
244 decamer (Fig. 3B-C) (*69*, *70*) (Fig. S7). Cross-linking mass spectrometry confirmed that
245 AcP10 interacts only with eIF2Bα and eIF2Bδ (Fig S8). 3D classification revealed that
246 ~24% of the particles were bound by one molecule of AcP10, while the remaining
247 particles had two AcP10 molecules bound. As expected and akin to NSs, the AcP10-
248 eIF2B structure exhibited an ordered eIF2Bβ latch-helix (Fig. 3B) and the fulcrum-helix
249 in its A-state conformation (Fig. S7F). These hallmarks are indicative of an A-state-
250 stabilized eIF2B with a productive eIF2α substrate-binding interface.
251
252 An intricate set of interactions between eIF2Bα and AcP10 anchors this viral effector to
253 eIF2B. AcP10 adopts a uridine-cytidine kinase fold, comprising a core of five-stranded
254 parallel β-sheets flanked on both sides by a pair of α-helices and additional α-helices
255 sitting above the core sheet structure together with a large β-hairpin loop. eIF2B is
256 engaged by AcP10 in a wedge-like manner by inserting its N and C-termini in-between
257 the concave surface formed by subunits eIF2Bα and eIF2Bδ (Fig. 3D, S9A). A
258 stabilizing edge-to-face π-π interaction between the aromatic rings of AcP10 F30 and
259 Y31 intercalates F30 into the hydrophobic groove formed in eIF2Bα between helices α3
260 and α4. The AcP10 aromatic F30-Y31 dyad further engages eIF2Bα via a strong cation-
261 π interaction with the guanidinium moiety of αR46 on helix α3 (Fig. 3D; top right panel).
262 These interactions, in turn, stabilize the opposite face of helix α4, allowing for strong
263 interaction with the latch-helix.
264
265 A second aromatic dyad within AcP10, composed of Y207 and F210 at the C-terminus,
266 also latches onto eIF2Bα's C-terminal helix (Fig. 3D; bottom right panel). These
267 interactions likely prevent the eIF2Bα C-terminus from moving inward, thereby

268 stabilizing a conformation of the latch-helix pocket in eIF2Bα that is conducive for latch-
269 helix binding. Additionally, the AcP10 C-terminal helix packs parallel to the longest helix
270 in eIF2Bδ forming a large interface stabilized by H-bonds and the hydrophobic effect
271 (Fig. 3D; bottom left panel).
272
273 A salient feature of the AcP10-eIF2B interaction is the use of 'aromatic fingers' that
274 intercalate in between helices α3 and α4 of eIF2Bα (Fig. 3D, S10). This arrangement is
275 reminiscent of interactions observed between NSs and eIF2B. However, diverging from
276 AcP10, NSs projects both sets of its aromatic fingers on either side of the eIF2Bα helix
277 α3, effectively sandwiching this helix. AcP10, by contrast, extends a pair of aromatic
278 fingers to contact the surface patch of eIF2Bα just next to eIF2Bδ, as well as a set of
279 polar residues to contact eIF2Bδ. Indeed, AcP10 buries ~621 $Å^2$ and ~757 $Å^2$ of solvent
280 accessible area against subunits eIF2Bα and eIF2Bδ, respectively, while NSs buries
281 ~995 $Å^2$ and ~149 $Å^2$, explaining their high binding affinities to eIF2B.
282
283 To probe the influence of the eIF2B-contacting amino acids, we purified AcP10 mutants
284 carrying alanine substitutions on key residues and measured their ability to bind eIF2B
285 decamers *in vitro*. Pairwise mutations to AcP10 F30/Y31 and H193/H200, resulted in a
286 strong loss of binding to eIF2B (Fig. S9B; lanes 9-10), while mutations to AcP10 M196
287 and Y207/F210 had partial effects (Fig. S9B; lanes 11-12). An AcP10 D29A mutation
288 had no effect on binding. Next, we explored the functional importance of these residues
289 by measuring competitive eIF2B binding between AcP10 and eIF2α-P. First, we titrated
290 AcP10 against pre-formed BODIPY-GDP-eIF2 complexes in the presence or absence
291 of eIF2α-P and measured nucleotide exchange *in vitro*. As expected, eIF2B GEF
292 activity was strongly inhibited by eIF2α-P [Fig. 3E - condition 2; S9C - condition 6, (*65*,
293 *66*)]. The inhibition was completely reversed upon addition of AcP10 (Fig. 3E - condition
294 3; S9C - conditions 9-10). In accordance with our binding assays, AcP10 carrying
295 F30A/Y31A or H193A/H200A mutations did not rescue the inhibitory effect of eIF2α-P,
296 while mutations to AcP10 Y207/F210 had subtle effects (Fig. 3E). We note here that
297 even in the absence of eIF2α-P, AcP10 stimulated eIF2B GEF activity (Fig. S9C,
298 conditions 1-5). This is consistent with our observation that apo-eIF2B continuously

samples the A- and I-state conformations (Fig. 1, S1), leading us to reason that AcP10 binding strongly shifts the equilibrium to the A-state. Supporting this notion, 3D variability analyses and multi-class cryo-EM reconstructions of eIF2B bound to AcP10 yielded no particles in the I-state (Fig. S7).

Second, we pre-incubated streptavidin-tagged eIF2B decamers with AcP10^{WT} or AcP10$^{H193A/H200A}$ and then added purified eIF2α-P to the respective mixtures. We affinity purified eIF2B-bound complexes and determined the relative amounts of eIF2α-P or AcP10 that co-purified with eIF2B by immunoblotting. As expected, in reaction mixtures containing only eIF2B and eIF2α-P, eIF2B bound efficiently to eIF2α-P (Fig. S9D, lane 4). In reaction mixtures containing eIF2B, AcP10^{WT} and eIF2α-P, eIF2B robustly bound to AcP10 but failed to efficiently co-purify eIF2α-P (Fig. S9D, lane 5). AcP10$^{H193A/H200A}$ did not co-precipitate with eIF2B efficiently and did not prevent the interaction between eIF2α-P and eIF2B (Fig. S9D, lane 6), corroborating the stabilizing role of these polar residues in the AcP10-eIF2B interface (*71*).

Third, we transfected GFP-tagged versions of NSs, AcP10, or the AcP10 interface mutants into HEK293T cells and tested their ability to inhibit the ISR induced by sodium arsenite, a commonly used activator of the ISR-inducing kinase HRI (*20*, *75*). AcP10 and NSs, but not the AcP10 interface mutants, strongly inhibited the accumulation of ATF4 and restored nascent protein synthesis rates even as eIF2-P levels remained high (Fig. 3F).

Together, these results indicate a remarkable convergence of evolutionary constraints that have shaped how structurally unrelated effectors from distinct viruses inhibit the ISR. BwCoV AcP10, like SFSV NSs, leverages molecular interactions involving 'aromatic fingers' combining strong hydrophobic and electrostatic components to engage the same 'hotspot' groove between helices α3 and α4 of eIF2Bα (Fig. S10). In doing so, both AcP10 and NSs hold eIF2Bα in the A-state with an open pocket for latch-helix binding while occluding eIF2-P binding.

AcP10 compensates for the loss of the eIF2Bβ latch-helix.

We next tested whether AcP10 binding could restore the enzymatic function of eIF2B$^{\Delta\text{-latch}}$. To this end, we first established that AcP10 binds to both eIF2B^{WT} and eIF2B$^{\Delta\text{-latch}}$ decamers (Fig. S11), indicating that, as expected, the latch-helix is not required for AcP10 binding. We then incubated wild-type AcP10 or interface mutants of AcP10 with eIF2B$^{\Delta\text{-latch}}$ decamers and assayed for enzymatic function *in vitro*. Remarkably, AcP10 accelerated the guanine-nucleotide exchange rate catalyzed by eIF2B$^{\Delta\text{-latch}}$ (Fig. 4A; $t_{1/2}$Δ-latch = 15.7 +/- 0.2 min vs. $t_{1/2}$Δ-latch + AcP10 = 4.8 +/- 0.7 min). This restorative effect was lost in reactions incubated with the AcP10 interface mutants (Fig. 4A). Corroborating these data, GFP-AcP10, but not GFP-AcP10$^{F30A/Y31A}$, robustly reversed ATF4 accumulation in *EIF2B2* depleted cells expressing eIF2Bβ$^{\Delta\text{-latch}}$ (Fig. 4B-C). Therefore, AcP10 binding compensates for the loss of the latch-helix and inhibits the eIF2B$^{\Delta\text{-latch}}$-induced ISR.

To characterize this reaction, we determined the AcP10-eIF2B$^{\Delta\text{-latch}}$ complex structure by cryo-EM (Fig. S12A-D). These maps revealed that AcP10 bound to eIF2B$^{\Delta\text{-latch}}$ through the eIF2-P binding pocket in the same manner as it did to eIF2B^{WT} (Fig. S12C). Structures of apo-eIF2B$^{\Delta\text{-latch}}$ overlaid onto AcP10-eIF2B$^{\Delta\text{-latch}}$ indicated a pronounced set of conformational changes in eIF2B$^{\Delta\text{-latch}}$ upon AcP10 binding (Fig. 4D-F). First, AcP10 induced a narrowing of the eIF2B$^{\Delta\text{-latch}}$ substrate binding pocket from 36 Å to 33 Å, conducive to productive eIF2 substrate binding (Fig. S12E). Second, by seizing hold of the groove between helices α3 and α4 of eIF2Bα, AcP10 reorients eIF2Bα to adopt an A-state position relative to eIF2Bβ and δ (Fig. 4D). However, the eIF2Bα C-terminal helix does not fully reset the latch-helix binding pocket to the wild-type A-state conformation. Instead, the aromatic ring of αF75 shifts to occupy the hydrophobic pocket of eIF2Bα that remains solvent-accessible upon loss of the latch-helix, thereby mimicking the A-state stabilizing environment created by the latch-helix residue βL113 (Fig 4D-E). This compensatory shift of αF75 is further stabilized by the sidechain of αR96 that reorients to sandwich the phenyl ring of αF75 in a cation-**π**-cation interaction with αR103 (Fig. 4E). Third, the fulcrum-helix on eIF2Bδ rotates back to the A-state conformation where δR517 engages in a salt bridge with αD298 (Fig. 4F).

361

362 Upon analysis of particles by 3D classification, we noted that an AcP10:eIF2B$^{\Delta\text{-latch}}$ ratio
363 of 2:1 in solution yielded ~35% of particles that were bound by two AcP10 molecules,
364 while ~23% of the particles classified into an asymmetric structure decorated by a
365 single AcP10 molecule (Fig. S12B; Class 2). The remaining particles lacked AcP10
366 density. Despite asymmetric AcP10 binding, the reorientation of eIF2Bα and the switch
367 of the eIF2Bδ fulcrum-helix to the A-state conformation was symmetrical on either side
368 of eIF2B$^{\Delta\text{-latch}}$, a conformational state identical to eIF2B$^{\Delta\text{-latch}}$ bound by two molecules of
369 AcP10 (Fig. 4D-F, Fig. S12F). This observation further demonstrates that coaxing the
370 A-state on one side of the decamer cooperatively favors the A-state on the opposite
371 side. Thus, despite the loss of the latch-helix, AcP10 pushes the eIF2Bα$_2$ dimer uphill
372 from its ground I-state into an A-state conformation, leading to stabilization of
373 enzymatically active eIF2B.
374

375 **Pharmacological regulation of eIF2B via the ISRIB pocket depends on latch-helix**
376 **interactions with eIF2Bα**

377 While NSs and AcP10 access the eIF2-P binding pocket to regulate eIF2B, the small
378 molecule ISRIB functions as an ISR inhibitor by binding a distinct pocket formed by the
379 two-fold symmetry interface between the β- and δ- subunits in eIF2B, ~50 Å distant
380 from the binding sites of these viral effectors (*4*, *5*, *65*, *66*). ISRIB enhanced the GEF
381 activity of eIF2B$^{\Delta\text{-latch}}$ three-fold, although it did not restore the activity to eIF2B^{WT} levels
382 (Fig. 5A), prompting us to ask how ISRIB-binding allosterically relates to the latch-helix.
383

384 To this end, we first measured the binding affinities of fluorescein-labeled ISRIB (FAM-
385 ISRIB) to both eIF2B^{WT} and eIF2B$^{\Delta\text{-latch}}$. FAM-ISRIB bound to eIF2B$^{\Delta\text{-latch}}$ with an
386 approximate four-fold affinity decrease as compared to eIF2B^{WT} (eIF2B^{WT} K_d = 26 nM
387 +/- 0.5 nM; eIF2B$^{\Delta\text{-latch}}$ K_d = 95 nM +/- 4.7 nM) (Fig. 5B). The structural basis for this
388 reduction in affinity becomes apparent when comparing the ISRIB-binding pocket
389 between the ISRIB-bound eIF2B^{WT} structure (PDB: 7L7G; *grey*) and the eIF2B$^{\Delta\text{-latch}}$
390 structure (*colored*) (Fig. 5C). Specifically, the length of the binding pocket increases by
391 more than 4 Å, displacing the hydrophobic pockets that receive the two terminal

392 halogenated benzene rings of ISRIB (*76*). βH188 and δL179 from one half of eIF2B
393 also move apart from the other half, disfavoring the centered binding of ISRIB
394 orthogonal to the symmetry axis. The I-state conformation of the ISRIB-binding pocket
395 is further stabilized by the lever-like rotation of the adjacent βH160 from its trans-
396 interface zippering interaction with β'R228 ('prime' indicates an amino acid in the
397 opposing tetramer across the symmetry interface) (Fig. S2C, Movie S2), facilitating
398 opening of the clefts between eIF2Bβ and eIF2Bδ' from the opposite tetramer.
399
400 The lengthening of the ISRIB pocket observed in eIF2B$^{\Delta\text{-latch}}$ suggested that the
401 corresponding lengthening of ISRIB might stabilize the I-state and pharmacologically
402 activate the ISR. Following this idea, we designed and synthesized ISRIB derivatives
403 that conformed to the longer pocket. To this end, we introduced two key modifications to
404 the glycolamide groups within ISRIB: (i) addition of a methylene group between the
405 amide and ether moieties; and (ii) addition of an aromatic group to the amide nitrogen
406 (based upon observations first reported by A. Zyryanova and D. Ron) (Fig. S13A). We
407 rationalized that modification (i) would increase the overall length of the molecule and
408 allow the terminal aryls to contact their cognate binding sites in the extended pocket,
409 while modification (ii) could potentially interact within the cleft that forms between
410 eIF2Bβ and eIF2Bδ' (Fig. 5C). We designed two molecules following this scheme,
411 named ISRACT-01 and ISRACT-02 (Fig. 5D). The primary difference between the two
412 compounds is the addition of the methylene extension on the opposing (ISRACT-01) or
413 same (ISRACT-02) side as the aromatic amide adduct.
414
415 To determine how these compounds fit within the I-state pocket, we determined cryo-
416 EM structures of eIF2B$^{\Delta\text{-latch}}$ bound to both compounds (Fig. S14A-F). Our
417 reconstruction of the ISRACT-01-bound eIF2B$^{\Delta\text{-latch}}$ complex allowed unambiguous
418 modelling of the compound binding pose. Despite stabilizing the Δ-latch I-state
419 conformation as expected, the branching benzyl group that we introduced on ISRACT-
420 01 occupied a shallow surface groove in the space between residues βN162 and
421 βH188 rather than the β/δ' cleft as we had expected (Fig. 5E).
422

423 The consensus structure of eIF2B$^{\Delta\text{-latch}}$ in complex with ISRACT-02 similarly showed
424 prominent density for the compound but required 3D classification to resolve
425 heterogeneous states. We found that ~25% of the particles sorted into an I-state
426 decamer in which ISRACT-02 was bound in the same manner as ISRACT-01. By
427 contrast, reconstruction of the remaining ~75% of the particles revealed ISRACT-02
428 bound, surprisingly, to an A-state decamer with the aromatic pyridine facing the solvent
429 rather than inserting into the β/δ' cleft or occupying the pocket between βN162 and
430 βH188 (Fig. 5F).
431
432 Closer inspection revealed that in the I-state particles, the ISRACT-02 tertiary amide
433 was in the *trans* conformation, while in the unexpected A-state it was in *cis*. In contrast
434 to secondary amides where *trans* is energetically favored, in tertiary amides both *trans*
435 and *cis* states are expected to have similar prevalence in the free ligand and will
436 interconvert in solution. The remarkable dual activity of ISRACT-02 appears to be a
437 result of the *trans*-amide conformation end-to-end length being ~2.3 Å longer, which
438 better fits the I-state pocket (Fig. 5F, right). Conversely, from our observations, the *cis*-
439 amide conformation of ISRACT-01 binds eIF2B$^{\Delta\text{-latch}}$ in the I-state, in which the *trans*-
440 amide conformation would be unable to bind.
441
442 These structures were corroborated by measurements of the binding affinities of the
443 FAM-derivatized ISRACT compounds toward eIF2B^{WT} or eIF2B$^{\Delta\text{-latch}}$ (Fig. S14I): FAM-
444 ISRACT-01 bound eIF2B^{WT} very weakly (K_d = not measurable with confidence), while it
445 bound eIF2B$^{\Delta\text{-latch}}$ with high nanomolar affinity (K_d = 557 nM +/- 97 nM). As expected,
446 FAM-ISRACT-02 bound eIF2B^{WT} (K_d = 174 nM +/- 32.2 nM) with a two-fold higher
447 affinity compared to eIF2B$^{\Delta\text{-latch}}$ (K_d = 385 nM +/- 7.8 nM). Together with the structures,
448 these data indicate that ISRACT-01 represents a *bona fide* ISR ACTivator, while
449 ISRACT-02 can stabilize either the A- or I-state of eIF2B.
450
451 To characterize ISRACT-01 further, we next measured its effect on the GEF activity of
452 either eIF2B^{WT} or eIF2B$^{\Delta\text{-latch}}$ *in vitro*. At saturating concentrations, ISRACT-01 did not
453 have an effect when incubated alone with either the active eIF2B^{WT} or the inactive

454 eIF2B$^{\Delta\text{-latch}}$ complex (Fig. 5G; conditions 2 and 4). However, ISRACT-01 notably
455 potentiated the effect of limiting amounts of eIF2-P to decelerate nucleotide exchange
456 by eIF2B^{WT} (Fig. 5G; condition 6). These results underscore the notion that ISRACT-01
457 binding to eIF2B is facilitated by I-state stabilization, leading to a synergistic inhibition in
458 the presence of both eIF2-P and ISRACT-01.
459
460 When tested in cells, we found that treatment with ISRACT-01 caused an increase in
461 the expression of ATF4 (Fig. 5H; *Eif2s1*$^{S51/S51}$ panel). Furthermore, ISRACT-01
462 protected cells from apoptosis activated by tunicamycin, an N-linked glycosylation
463 inhibitor that causes ER stress and activation of the eIF2 kinase PERK (Fig. S15A). In
464 contrast, eIF2B activation with ISRIB accelerated tunicamycin-induced cell death, as
465 reported previously (*49*) (Fig. S15A). Polysome profiling of cells treated with ISRACT-01
466 showed an increase in the 60S and 80S ribosome subunit fractions accompanied by a
467 concomitant decrease in the heavier polysome fractions, phenocopying protein
468 synthesis defects observed during the ISR (*49*) (Fig. S15B,C). In line with the *in vitro*
469 GEF assays described above, ISRACT-01 treatments of cells deficient for eIF2α
470 phosphorylation (*Eif2s1*$^{S51A/S51A}$) (*77*) did not stimulate strong ATF4 accumulation (Fig.
471 5H; *Eif2s1*$^{S51A/S51A}$ panel). Together, these observations indicate that ISRACT-01
472 binding alone is unable to displace the latch-helix. It is, however, sufficient to stabilize
473 the I-state in the presence of limiting amounts of cellular eIF2-P, thus enhancing a
474 cytoprotective ISR during tunicamycin-induced ER stress.

Discussion

The allosteric communication axes in eIF2B

The regulatory allosteric signaling axes described in this work explain how the antagonistic binding of substrate (eIF2) and inhibitor (eIF2-P) is communicated over the 40 Å distance along eIF2B's central interface. Four conformational elements aligned along two identical, symmetry-related axes operate in concert: (i) the latch-helix docking to its binding pocket in eIF2Bα, (ii) the rotation of the fulcrum-helix in eIF2Bδ, (iii) the βH160 tetramer-tetramer interface zipper, and (iv) the substrate eIF2 binding pocket (Fig. 6). We establish that discrete conformational changes in these four elements, synchronized both within- and across-axes, define the active-to-inactive A- to I-state transition in eIF2B (Movie S4). Two convergently evolved viral effectors exert their effect by locking eIF2Bα, and with it the entire eIF2B complex, into the A-state.

Comparing the parsed structure classes of unliganded eIF2B by cryo-EM 3D variability analysis, we demonstrate that apo-eIF2B exists in an equilibrium of A- and I-states, suggesting a relatively flat energy landscape between the two states. In the absence of an inhibitor, engagement of the eIF2Bβ latch-helix with the eIF2Bα latch-helix pocket biases the conformational equilibrium toward the A-state, which the viral effectors AcP10 and NSs further stabilize. By contrast, eIF2-P binding to eIF2B skews the equilibrium towards the I-state by stabilizing a remodeled latch-helix pocket. This interaction reorients eIF2Bα to drive the series of events along the allosteric axes that results in a widening of the substrate binding pocket to disfavor eIF2 binding. In doing so, eIF2-P binding stabilizes eIF2Bα in its intrinsic ground I-state conformation, as observed in crystal structures of eIF2Bα homodimers (Fig. S5C). Experimentally, the I-state can be further stabilized by a rationally designed ISR activator ISRACT-01 that, due to its increased length over the clinical ISR inhibitors based on ISRIB, buttresses the I-state-induced cleft between tetramer-tetramer interfaces.

Two mirrored allosteric axes connect the symmetry interface of the eIF2B complex. This observation expands the model of allosteric regulation proposed by Monod, Wyman, and Changeux (*78*) to include state-transitions of complexes formed by non-identical

506 subunits. The experiments with the viral effector AcP10 provide first evidence that
507 activation or inhibition of eIF2B on one side synchronizes the symmetry-related other
508 side of the complex (Fig. S12F). We pose that such asymmetric communication is likely
509 mimicked by eIF2B's interactions with its substrate, eIF2, whose binding positions
510 eIF2α as a tether between the two tetramers and hence stabilizes the A-state.
511
512 *Evolutionary considerations of latch-helix mediated regulation*
513 Based on sequence and structural homology, the α, β, and δ subunits of eIF2B are
514 evolutionarily related to archaeal aIF2B proteins (*79*). While eIF2Bδ has a large, flexible
515 N-terminal expansion, only eIF2Bβ evolved the latch-helix containing insertion between
516 helices α4 and α5 (Fig. S5A, S5D). Furthermore, analysis of eIF2Bβ sequences across
517 eukaryotes reveals remarkable conservation of the latch-helix with hydrophobic side
518 chains that likely fit snugly into the latch-helix pocket (Fig. S5B, S5D). Thus, it is
519 plausible that a latch-helix based regulatory node in eIF2B co-evolved with its role as a
520 GEF for eIF2 in eukaryotes. Notably, the amino acids defining the latch-helix binding
521 pocket in eIF2Bα are likewise conserved (Fig. S5E) and thus eIF2Bα emerges from this
522 and other studies (*73*) as a determinant of the allosteric modulation effected by
523 metabolites, viral effectors, and eIF2-P.
524
525 While the function of the closest related aIF2Bs have not been elucidated, two families
526 of proteins that are sequentially and structurally related to a/eIF2B are sugar phosphate
527 isomerases (*79*–*81*), and human eIF2Bα retains the capability to bind sugar phosphates
528 M6P and F6P *in vitro* (*73*). We show here that eIF2Bα dynamically closes its latch-helix
529 binding pocket in response to eIF2-P, inducing the I-state. The consensus structures for
530 M6P-bound eIF2Bα dimers and F6P-bound eIF2B decamers likewise adopt I-state
531 conformations. Indeed, in support of our findings, the latch-helix is unresolved in the
532 F6P-bound decamer, yet paradoxically, both M6P and F6P stimulate eIF2B activity *in*
533 *vitro*—an observation that remains unexplained. In addition to eIF2Bα, eIF2Bβ and δ
534 are also evolutionarily related to sugar phosphate binding proteins and may likewise
535 retain metabolite-binding properties that conceivably regulate eIF2B function.
536

537 Surprisingly, the viral protein AcP10 is agnostic to the presence of the latch-helix in
538 eIF2B (see Figs. 3-4). Through a series of intricate, precise, and evolutionarily
539 convergent interactions that rely on aromatic amino acid “fingers”, both AcP10 and NSs
540 coerce the α-subunit of eIF2B to reorient to the A-state conformation (Figs. 3D; 4D-E,
541 S10). Viral protein use of aromatic fingers emerges as a compelling evolutionary means
542 to force productive interaction surfaces, as often observed in high-affinity interactions,
543 such as those mediated between antigens and antibodies (*82*, *83*). Using this trick to
544 good effect, AcP10/NSs target eIF2B, activate the enzyme, and suppress the ISR.
545
546 *Considerations of small molecule ISR activators*
547 While an increasing body of literature has focused on activating eIF2B for therapeutic
548 benefit with small molecules (*49*, *54*, *63*, *64*, *84*), the characterization of the eIF2B I-
549 state allowed us and others to design eIF2B inhibitors, ISRACTs, that target the same
550 pocket as the ISR inhibitor ISRIB. ISRACT-01, in particular, is a valuable tool to study
551 the ISR in cells by allowing specific ISR activation directly through eIF2B. This mode of
552 action distinguishes ISRACT-01 from other compounds that induce eIF2 kinase-
553 mediated increases in eIF2-P. Since kinases generally phosphorylate a spectrum of
554 substrate proteins, it is unlikely that ISR kinases only phosphorylate eIF2α (*85*, *86*).
555 Rather, ISR kinases likely change the cell’s phospho-proteome in yet uncharacterized
556 ways and hence alter the molecular environment in which the ISR ultimately exerts its
557 effects. Medicinally, further development of ISRACTs may serve as alternatives to ISR-
558 activating phosphatase inhibitors such as salubrinal (*87*) which has shown promise in
559 models of Charcot-Marie-Tooth disease (*88*) and sickle-cell anemia (*89*), and the GCN2
560 kinase activator halofuginone that protects from diabetes in a model of diet induced
561 obesity (*90*).
562
563 We note that the modifications introduced to the ISRIB backbone to generate ISRACT
564 impose some pharmacokinetic penalties. The binding pose of the added benzyl group
565 restricts the movement of residue βH188 on eIF2B, which is generally observed as a
566 mixture of rotamers, thereby potentially imposing an entropic penalty. Since the
567 discovery of ISRIB, the molecule has been optimized into a clinical candidate through

568 structure-activity relationship studies (*54*, *76*). Given their shared backbone, the
569 principles of improving ISRIB's pharmacological properties should be applicable to
570 ISRACT as well. Furthermore, our increased structural understanding of eIF2B and its
571 regulation via its allosteric signaling axes opens new ways to explore drugging
572 alternative pockets, such as the latch-helix binding pocket and/or the eIF2-
573 P/metabolite/viral effector binding pockets of the alpha subunit, for therapeutic benefit
574 as we learn with increasing precision how to modulate the ISR across biological scales.

Acknowledgements

This work was supported by Altos Labs, Inc. We thank Steve McKerrall and Deniz Eismann for helpful conversations, and members of the Altos Labs Institute of Science for comments on the manuscript. We also thank the Altos Labs cryo-EM hub for data collection and analysis, and Josh Lee and She-Rene Chen for support and review of this manuscript.

Funding:

Author contributions:

Conceptualization: TIC, AD, UD, AS, NJ, FZ, FJMvK, JJC, PW, AF

Methodology: UD, AS, TIC, DJL, PFE, CPA, JJC, AF, PW

Investigation: UD, AS, AD, JC, MV, MB, PFE, LH, DJL, YL, LCR, KS, HT, MLV, CPA, TIC

Resources: RJdG, FJMvK

Writing - Original Draft: UD, AS, PFE, TIC, PW, AF

Writing - Review & Editing: All authors

Visualization: UD, AS, PFE, TIC, PW, AF

Supervision: NT, CPA, JN, DAA, MCM, JJC, PW, AF

Competing interests: PW and DAA are inventors of ISRIB. A patent is held by the Regents of the University of California that describes ISRIB and its analogs. Rights to the invention have been licensed by UCSF to Calico. All authors affiliated with Altos Labs are option holders or shareholders in Altos Labs, Inc. All other authors declare no competing interests.

Data and materials availability: Cryo-EM density maps and associated models will be publicly available through the wwPDB with accession codes: PDB: 9Y3P, 9Y3U, 9Y3Q, 9Y3T, 9Y3V, 9Y3W, 9Y4B, 9Y5S, 9Y5R, 9Y5T, 9Y5U; EDM-72462, 72467, 72463, 72466, 72468, 72499, 72477, 72521, 72520, 72522, 72523. All other raw data are available upon request through data transfer agreements.

Supplementary Materials

Materials and Methods

Figs. S1 to S15

Tables S1 to S4

Movies S1 to S4

612 **Main Text Figure Legends**

613

614 **Fig 1. Disordering of a helical latch that bridges eIF2Bβ and eIF2Bα demarcates**
615 **the inactivation of eIF2B.**
616 (A) (Top) Cryo-EM density of wild-type eIF2B$(\alpha\beta\gamma\delta\varepsilon)_2$ in the apo, A-state with the
617 location of the latch-helix highlighted in cyan. (Bottom) Cryo-EM density of eIF2B in an
618 apo, I-state where the latch-helix is no longer resolvable. Direction of three trajectories
619 of motion identified by 3D variability analysis are indicated by **1**, **2**, and **3**, respectively
620 (see Supp movie S1) (B) Zoom-in on the eIF2 binding interfaces defined by residues
621 βN132 and δ'R250 (' indicates a subunit from the opposing half of eIF2B) from the eIF2
622 substrate-bound (PDB: 6O81, top) and the eIF2α-P inhibitor-bound (PDB: 9Y5R,
623 bottom) structures with the model of eIF2α (pink) from 6O81 overlaid. (C) (Left)
624 Distribution of eIF2B particles after 3D classification, as measured by the distance
625 between βN132 and δ'R250 in structures from 8 distinct 3D classes. (Right) Close-up
626 view of the eIF2B α-β interface from the cryo-EM structures of eIF2-eIF2B (EMD-0649),
627 eIF2α-P (EMD-72523), and representative A-state and I-state structures from 3D
628 classification. (D) Zoom-in of the latch-helix and its binding pocket with a transparent
629 surface representation of eIF2Bα colored by molecular hydrophobicity potential. Key
630 residues of eIF2Bα and eIF2Bβ are labeled according to the color of each subunit. (E)
631 The structural model of eIF2α-P (pink)-bound eIF2Bα (maroon) overlaid with a
632 transparent model of A-state apo eIF2Bα (gray) and eIF2Bβ latch-helix (blue).
633 Conformational changes of interest are indicated with dashed arrows and potential
634 steric clashes indicated by curved lines.

635

636 **Fig 2. Removal of the eIF2Bβ latch-helix is sufficient to inactivate eIF2B.**
637 (A) Guanine nucleotide exchange factor (GEF) activity as measured by BODIPY-GDP
638 loading onto eIF2, using 10 nM wild-type ($eIF2B^{WT}$) or β100-116 deletion ($eIF2B^{\Delta\text{-latch}}$)
639 eIF2B as the enzyme and 100 nM eIF2 as the substrate. The left panel shows a
640 representative time course readout of a 60-minute nucleotide exchange reaction. The
641 $t_{1/2}$ of nucleotide loading from three experiments are plotted and averaged in the right
642 panel. Data represent the mean±s.e.m ($n \geq 4$). (B) Sedimentation velocity of WT and Δ-
643 latch eIF2Bβγδε in the presence or absence of $eIF2B\alpha_2$ as measured by analytical
644 ultracentrifugation. (C) Lysates of HEK293T cells transfected for 72 hours with either

645 non-targeting (siNT) or *EIF2B2*-targeting (si*EIF2B2*) siRNA were subjected to
646 immunoblotting using antibodies to eIF2Bβ and vinculin. Densitometry of the eIF2Bβ
647 blot intensity normalized to the intensity of Vinculin and plotted relative to the non-
648 targeting control. Data represent the mean±s.e.m (n=4). (D) Immunoblots and
649 quantifications of lysates of HEK293T cells co-transfected with either non-targeting
650 (siNT) or *EIF2B2*-targeting (si*EIF2B2*) knockdown siRNA and rescue plasmids
651 expressing siRNA resistant and mApple-FLAG tagged $eIF2B\beta^{WT}$ or $eIF2B\beta^{\Delta\text{-}latch}$. ATF4
652 mean fold changes are normalized to the amount of Vinculin measured by
653 densitometry. Data represent the mean±s.e.m (n=4). (E). The I-state cryo-EM structure
654 of $eIF2B^{\Delta\text{-}latch}$ (left) with a zoom-in view of the eIF2Bα latch-helix binding pocket in red
655 overlaid with the eIF2α-P bound I-state conformation in transparent grey (right). (F)
656 Distribution of $eIF2B^{WT}$ (gray) and $eIF2B^{\Delta\text{-}latch}$ (black) particle conformations as
657 measured by the distance between residues βN132 and δ'R250 from structural models
658 fit into cryo-EM maps generated by 3D classification.
659
660 **Fig 3. Viral proteins AcP10 and NSs convergently evolved as activators of eIF2B**
661 **that order the latch-helix and outcompete eIF2-P to suppress the ISR.**
662 (A) *In vitro* pulldowns of purified $eIF2B\alpha_2$ (200 nM), eIF2Bβδγε (400 nM) or
663 $eIF2B(\alpha\beta\delta\gamma\varepsilon)_2$ (200 nM) with MBP-FLAG (1 μM) and MBP-AcP10 (1 μM).
664 Immunoblotting was performed using antibodies to eIF2B subunits and MBP. Data are
665 representative of three independent experiments. (B) Cryo-EM density of the AcP10-
666 $eIF2B^{WT}$ complex showing two copies of AcP10 (orange) bound. (C) Comparison of the
667 binding locations on eIF2Bα/δ occupied by either eIF2α-P (top left), NSs (top right) or
668 AcP10 (bottom left). The bottom right panel depicts the overlay of the interface. eIF2Bα
669 - red; eIF2Bδ - yellow; eIF2α-P - violet; NSs - blue; AcP10 - orange. (D) Zoomed-in view
670 of the entire AcP10-eIF2B interaction interface (top left) with key interactions made by
671 AcP10 residues (clockwise from top right): F30/Y31 with eIF2Bα, Y207/F210 with
672 eIF2Bα, and H193/H200 with eIF2Bδ. Hydrogen bond, electrostatic, or cation–π
673 interactions are denoted by dashed lines. AcP10 - orange; eIF2Bα - red; eIF2Bδ -
674 yellow; eIF2Bβ latch-helix - light blue. (E) GEF activity as measured by BODIPY-GDP
675 unloading from eIF2 (100 nM) by $eIF2B^{WT}$ decamers (10 nM) with or without the addition

676 of eIF2α-P (1 μM), MBP-AcP10 WT (1 μM) or MBP-AcP10 interface mutants (1 μM), as
677 indicated. Shown are mean±s.e.m. of $t_{1/2}$ values derived from a one-phase decay fit of
678 four replicates. (F) HEK293T cells were transfected for 24 hours with plasmids
679 expressing GFP-tagged AcP10, AcP10 interface mutants or NSs and treated with
680 sodium arsenite (50 μM) for 4 hours to induce the ISR. For a set of experiments, cells
681 were subjected to puromycin pulse-chase analyses to assess nascent protein synthesis
682 rates. Immunoblotting of lysates was performed using antibodies to puromycin, vinculin,
683 GFP, ATF4 and eIF2α-P. Puromycin pulse-chase (n=2) and ATF4/eIF2α-P
684 accumulation (n=4) assay samples were processed in parallel on separate gels.
685 Representative blots are shown.
686
687 **Fig 4. AcP10 rescues the activity of eIF2B$^{\Delta\text{-latch}}$ and suppresses ISR activation in**
688 **eIF2B$^{\Delta\text{-latch}}$ mutant cells.**
689 (A) GEF activity as measured by BODIPY-GDP loading onto eIF2 (100 nM) by eIF2B^{WT}
690 (10 nM) with or without the addition of eIF2α-P (1 μM) or eIF2B$^{\Delta\text{-latch}}$ decamers (10 nM)
691 with or without the addition of MBP-AcP10 WT (1 μM) or MBP-AcP10 interface mutants
692 (1 μM), as indicated. Shown are mean±s.e.m. of $t_{1/2}$ values derived from a one-phase
693 association fit for four experimental replicates. (B) Immunoblots of HEK293T cell lysates
694 co-transfected with either non-targeting (siNT) or *EIF2B2*-targeting (si*EIF2B2*) siRNA
695 and rescue plasmids expressing siRNA resistant and mApple-FLAG tagged *eIF2Bβ*$^{\Delta\text{-}}$
696 ^{latch}. (C) Fold changes in the levels of ATF4 normalized to the amount of Vinculin in cells
697 by densitometry. Data represent the mean±s.e.m (n=4). (D - F) The structural models
698 of eIF2Bα (top and middle panels) and eIF2Bδ (bottom panel) when AcP10 (orange) is
699 bound to eIF2B$^{\Delta\text{-latch}}$ (multi-colored) overlaid with A-state apo eIF2B^{WT} (blue) and I-state
700 apo eIF2B$^{\Delta\text{-latch}}$ (gray) with the latch-helix highlighted (cyan). Conformational changes of
701 interest are indicated with dashed arrows and denote I- to A- state-transition. The
702 cation–π–cation interaction in (E) is denoted with dashed lines.
703
704 **Fig 5. The eIF2B pharmacophore is allosterically modulated by latch-helix**
705 **ordering.**

706 (A) Guanine nucleotide exchange factor (GEF) activity as measured by BODIPY-GDP
707 loading, using 10 nM eIF2B^{WT} or eIF2B$^{\Delta\text{-latch}}$ (with and without 1 μM ISRIB pre-
708 incubation) as the enzyme and 100 nM eIF2 as the substrate. (B) Fluorescence
709 polarization based binding assay to measure binding of fluorescein conjugated ISRIB
710 (FAM-ISRIB) to eIF2B^{WT} and eIF2B$^{\Delta\text{-latch}}$. (C) Close-up view of the ISRIB binding pocket
711 of eIF2B$^{\Delta\text{-latch}}$ (colored) overlaid with a model of ISRIB in complex with eIF2B^{WT} (PDB:
712 7L7G) in gray. Key residues are shown as sticks and labeled by subunit color with (‘)
713 indicating residues from the opposite tetramer. The observed widening of the pocket is
714 indicated in red. (1) and (2) indicate major structural differences targeted for rational
715 design of eIF2B inhibitors. (D) Chemical structures of compounds ISRACT-01 and
716 ISRACT-02 with the modifications relative to ISRIB shown in red. Cis/trans
717 isomerization of ISRACT-02 around the amide bond are indicated by arrows. (E) Zoom-
718 in view of the ISRACT/ISRIB binding pocket from cryo-EM structures of eIF2B$^{\Delta\text{-latch}}$
719 bound to ISRACT-01 I-state shown as cartoons (left) and an alternate viewing direction
720 as surface view (right). (F) Structures of ISRACT-02 in complex with eIF2B$^{\Delta\text{-latch}}$ in the I-
721 state (top) and A-state (bottom). Percent of particles per conformation are indicated to
722 the left. Alternate surface views on the right demonstrate the change in amide
723 isomerization and end-to-end length of ISRACT-02. (G) GEF activity of eIF2B^{WT} and
724 eIF2B$^{\Delta\text{-latch}}$ upon treatment with 10 μM of ISRACT-01. eIF2B^{WT} inhibition was also
725 tested upon treatment with 50 nM eIF2-P, or 50 nM eIF2-P + 10 μM ISRACT-01. (H)
726 Immunoblots of mouse embryonic fibroblast lysates of *Eif2fs1*$^{S51/S51}$ or *Eif2fs1*$^{S51A/S51A}$
727 cells treated with the indicated concentrations of ISRACT-01 or the ISRIB analogue
728 2BAct for 3 hours. Panels were cropped from the same gel. Representative blots from n
729 = 4 experiments are shown.
730
731 **Fig 6. Latch-helix ordering propagates along an allosteric axis that links eIF2B’s**
732 **substrate, inhibitor, and pharmacophore sites.**
733 Model of eIF2B A- to I-state transition encompassing shifts in the conformational
734 equilibrium within the α, β, and δ core that are induced by eIF2-P, small molecules, and
735 effector proteins to regulate eIF2B activity. Arrows depict the conformational changes
736 imparted during I-state stabilization.

737 **Supplementary Materials for**

738

739 **Allosteric Disordering of eIF2B Regulates the Integrated Stress Response**

740

741 Udit Dalwadi, Advait Subramanian, *et al.*

742

743 *Corresponding authors: afrost@altoslabs.com, pwalter@altoslabs.com

744

745

746 **The PDF file includes:**

747

748 Materials and Methods
749 Figs. S1 to S15
750 Tables S1 to S4
751 References

752

753 **Other Supplementary Materials for this manuscript include the following:**

754

755 Movies S1 to S4

756

757 **Materials and Methods**

758

759 ***Protein expression and purification***

760 *eIF2Bβγδε tetramers*

761

762 Plasmids containing *E. coli* codon-optimized dual ORFs of eIF2Bβ&δ (His-tagged WT:
763 pAD025, His-Strep tagged WT: pPE-011, His-tagged Δ-latch: pAD028) and eIF2Bγ&ε
764 (pAD024) were transformed into OneShot BL21 Star (DE3) chemically competent cells
765 (Invitrogen). Following 1 h recovery in LB media, the entire transformation mixture was
766 used to inoculate 50 mL of LB media containing chloramphenicol and kanamycin and
767 grown overnight at 37 °C. 6 x 1 L of LB media (+chloramphenicol and kanamycin) were
768 inoculated with 12 mL each of the overnight culture and grown at 37 °C until the culture
769 reached an OD_{600} of 0.8. Expression was then induced by addition of IPTG to a final
770 concentration of 0.8 mM and continued for 20 hours at 16 °C. Cells were harvested by
771 centrifugation (10 minutes at 4000 x g) and stored at -80 °C or used immediately for
772 purification. Pellets were resuspended with 4 mL/g wet pellet of cold lysis buffer (40 mM
773 HEPES KOH pH 7.5, 250 mM KCl, 1 mM TCEP, 5 mM $MgCl_2$, 15 mM Imidazole pH 8,
774 and 1 tablet/50 mL of cOmplete EDTA-free protease inhibitor cocktail (Roche)). *E. coli*
775 were lysed by three consecutive cycles through an EmulsiFlex-C3 (Avestin)
776 homogenizer then cleared by centrifugation at 18,000 x g for 60 minutes at 4 °C. All
777 subsequent steps were carried out using an AKTA Pure FPLC (Cytiva) at 4 °C. The
778 clarified lysate was loaded onto a 5 mL HisTrap HP column equilibrated in HisTrap
779 buffer A (20 mM HEPES KOH pH 7.4, 200 mM KCl, 5 mM $MgCl_2$, 15 mM Imidazole, 1
780 mM TCEP), followed by washing with 5 CV of the buffer. Sample was then eluted from

781 the column over a 0-100% linear gradient into HisTrap buffer B (20 mM HEPES KOH
782 pH 7.4, 200 mM KCl, 5 mM $MgCl_2$, 300 mM Imidazole, 1 mM TCEP). Peak fractions
783 containing eIF2Bβγδε were pooled and applied to a MonoQ 10/100 GL column
784 equilibrated in IEX buffer A (20 mM HEPES KOH pH 7.4, 200 mM KCl, 5 mM $MgCl_2$, 1
785 mM TCEP) and then washed with 5 CV of the buffer. Bound proteins were eluted using
786 a linear 0-100% gradient of IEX buffer B (20 mM HEPES KOH pH 7.4, 500 mM KCl, 5
787 mM $MgCl_2$, 1 mM TCEP) over 10 CV. Peak fractions containing eIF2Bβγδε were
788 pooled, concentrated, and loaded onto a Superdex 200 Increase 10/300 column
789 equilibrated with SEC buffer (20 mM HEPES KOH pH 7.4, 200 mM KCl, 5 mM $MgCl_2$,
790 5% glycerol, 1 mM TCEP). The final purified sample was concentrated using a 100k
791 MWCO spin concentrator (Millipore), flash frozen in liquid nitrogen, and stored at -80 C
792 until use. A typical yield was 3 mg of >95% pure tetramer from 6 L of *E. coli* culture.
793
794 *eIF2Bα dimers*
795
796 eIF2Bα dimers were initially purified as described previously (*65*). The following protocol
797 was employed to increase yield and purity of the final protein. A modified pRSF Duet
798 plasmid containing *E. coli* codon-optimized (His8-MBP-Thrombin cut site) tagged
799 eIF2Bα ORF (pPFE ALTOS-041) was transformed into OneShot BL21 Star (DE3)
800 chemically competent cells (Invitrogen) and grown on LB-Agar containing Kanamycin. A
801 single colony was used to inoculate a 100 mL overnight culture. 20 mL of the overnight
802 culture was used to inoculate 3 x 1 L of TB media (+Kanamycin) and the culture was
803 grown at 37 °C until the culture reached an OD_{600} of 0.8. Expression was then induced
804 by addition of IPTG to a final concentration of 0.8 mM and continued for 20 hours at 17
805 °C. Cells were harvested by centrifugation (17 minutes at 4000 x g) and stored at -80
806 °C or used immediately for purification. Pellets were resuspended with 100 mL of cold
807 lysis buffer (40 mM Tris-HCl pH 7.5, 500 mM NaCl, 5% glycerol, 1 mM TCEP, 1 mM
808 PMSF, and 1 tablet/50 mL of cOmplete EDTA-free protease inhibitor cocktail (Roche)).
809 *E. coli* were lysed by four consecutive cycles through an EmulsiFlex-C3 (Avestin)
810 homogenizer then cleared by centrifugation at 23,000 x g for 60 minutes at 4 °C. The
811 clarified lysate was incubated with 10 mL Cobalt IMAC resin (Takara) (equilibrated in
812 lysis buffer) and incubated for 1 hour with gentle rotation to allow batch binding. The
813 resin was applied to a gravity column and washed with 25 CV of lysis buffer containing
814 12.5 mM imidazole, and bound protein was eluted using 7 CV of lysis buffer containing
815 125 mM imidazole. The elution fraction was next incubated with 10 mL of equilibrated
816 Amylose resin (NEB) for 30 minutes with gentle rotation. The resin was washed with 5
817 CV Amylose wash buffer (40 mM Tris-HCl pH 7.5, 300 mM NaCl, 5% glycerol) then
818 eluted with 5 CV of Amylose wash buffer supplemented with 50 mM maltose. The
819 eluted proteins were concentrated to 1 mL and purified further by size exclusion
820 chromatography using a HiLoad Superdex200 Increase 16/60 column equilibrated in
821 SEC buffer (20 mM HEPES-KOH pH 8, 200 mM KCl, 5 mM $MgCl_2$, 0.5 mM TCEP) on
822 an AKTA Pure instrument (Cytiva). The peak fractions containing His-MBP-eIF2Bα
823 were pooled and the His-MBP tag was then cleaved using thrombin for 96 hours at 4
824 °C. The resultant mixture was purified by size exclusion chromatography using a
825 HiLoad Superdex 75 16/60 column in SEC buffer. The peak fractions containing
826 cleaved protein were pooled and passed over a Cobalt IMAC-Amylose mixed slurry to

827 remove residual His-MBP fusions. The flow-through was collected, concentrated, flash
828 frozen in liquid nitrogen and stored at -80 °C until use. A typical yield was ~25 mg of
829 >99% pure protein from 3 L of *E. coli* culture.
830
831 *AcP10*
832
833 *E. coli* BL21 (DE3) cultures expressing His-MBP-AcP10 or corresponding mutant
834 plasmids were first cultured overnight at 37 °C. These overnight cultures were
835 subcultured (1:100) in LB medium, supplemented with the appropriate antibiotics, to
836 OD600 = 0.6. Protein expression was then induced with 1 mM IPTG and the culture was
837 grown at 16 °C overnight. The next day, the bacteria were centrifuged at 6,000 r.p.m. for
838 5 min at 4 °C, followed by incubation of the pellets in bacterial lysis buffer (50 mM Tris-
839 HCl pH 8, 300 mM NaCl, 5 mM Imidazole, 0.2 mM TCEP, 0.5 mM PMSF, 5% glycerol
840 and complete protease inhibitor) for 60 min on ice. The mixtures were then lysed by
841 three passes through an EmulsiFlex C3 high pressure homogenizer (Avestin). The
842 lysate was then cleared by centrifugation at 20,000 x g for 45 min at 4 °C. The
843 supernatant was applied onto a gravity column packed with TALON IMAC resin at 4 °C
844 to enable batch binding for 1 hour at 4 °C. The resin was washed with five column
845 volumes of wash buffer (50 mM Tris-HCl pH 8, 300 mM NaCl, 20 mM Imidazole, 0.1 mM
846 TCEP, 0.1 mM PMSF, 5% glycerol and cOmplete protease inhibitor). His-MBP-AcP10
847 was eluted with elution buffer (50 mM Tris-HCl pH 8.0, 300 mM NaCl, 200 mM
848 glutathione, 0.1 mM TCEP, and 5% glycerol) and concentrated at 4 °C using Amicon
849 Ultra centrifugal filters with repeated mixing to prevent aggregate formation. The purified
850 proteins were analyzed by SDS–PAGE and Coomassie brilliant blue staining. The
851 protein concentrations were calculated by measuring absorbance at 280 nm and
852 applying the Beer–Lambert law ($A = \varepsilon lc$; $\varepsilon = 82990$). In certain cases, proteins were
853 further purified by gel filtration chromatography using a Superdex 200 column attached
854 to an AKTA Pure FPLC (Cytiva) and running buffer containing 50 mM Tris-HCl pH 8.0,
855 300 mM NaCl and protease inhibitor cocktail. Elution fractions containing protein were
856 analysed by their A280 spectra, SDS–PAGE and Coomassie brilliant blue staining.
857
858 *eIF2 and eIF2-P*
859
860 Heretotrimeric eIF2 was generated by co-expression of full length eIF2α, N-term FLAG-
861 Tev tagged eIF2β (2-333, K79R, K80R, K81R, K83R, K84R), eIF2γ (91-472), CDC123
862 in Expi293F cells. Equimolar ratios of codon-optimized plasmids (0.75 µg of each
863 plasmid per mL of cell culture) were diluted in Opti-MEM media (Gibco) to a final
864 concentration of 18 µg/mL. The diluted plasmids were then combined with an equivalent
865 volume of PEI at 0.12 mg/mL in Opti-MEM. The mixture was added dropwise to cells at
866 a density of ~$3x10^6$ cells/mL to transfect the plasmids. The cells were grown for 20
867 hours on an orbital shaker at 37 °C, 8% CO_2 at a speed of 125 rpm before addition of
868 Expi Enhancer to the culture. Cell pellets were harvested by centrifugation 72 h after
869 transfection. Pellets were resuspended with 5 mL/g lysis buffer (20 mM HEPES KOH
870 pH 7.4, 300 mM KCl, 1 mM $MgCl_2$, 0.001 mM Triton X-100, 1 tablet/50 mL protease
871 inhibitor cocktail) and lysed by sonication (3 s on, 5 s off, 200 W for 100 cycles).
872 Lysates were clarified by two consecutive centrifugations for 30 mins at 20300 x g, 4

873 °C. The supernatant was incubated with anti-FLAG M2 affinity gel (Sigma) and bound
874 protein was eluted with 100 µg/ml of FLAG peptide. 1mM GDP was added to the
875 eluate and incubated for one hour. For phosphorylation, GST-PKR was added to the
876 solution at 1:20 (PKR:eIF2, w/w) and ATP was added to a final concentration of 1 mM.
877 The protein treated with/without PKR kinase was further purified by size exclusion
878 chromatography using a Superdex 200 Increase 10/300 GL (Cytiva) column and
879 concentrated by ultra-filtration (Amicon, MWCO 30 kD). The final protein was analyzed
880 using Phos-tag SDS-PAGE (Fujifilm) to determine the phosphorylation state, then flash
881 frozen in liquid nitrogen and stored at -80°C until use.
882
883 *eIF2α(NTD)-P*
884
885 The coding sequence of the human eIF2α subunit N-terminal domain (residues 2-187)
886 with an N-term 6xHis-Tev cut site tag was codon optimized, synthesized, and cloned
887 into a pET28(a) vector. The plasmid was transformed into chemically competent
888 OneShot Bl21 Star (DE3) *E. coli* and a single colony was picked to start an overnight
889 culture. Following overnight growth at 37 °C, the culture was used to inoculate 2 L
890 (1:250) of ZYP-5052 autoinduction media which was then grown for 20 hours at 20 °C.
891 Cell pellets were harvested by centrifugation for 10 mins at 4000 x g, washed once with
892 PBS and stored at -80 °C until use. Cells were resuspended in lysis buffer (20 mM Tris-
893 HCl pH 7.5, 500 mM NaCl, 20 mM imidazole, 1 mM PMSF, and 1 tablet/50 mL EDTA-
894 free protease inhibitor cocktail) and lysed by sonication using a Branson 450 sonifier
895 (pulses of 10 s on, 10 s off for 20 minutes at 60% power). Lysates were cleared by
896 centrifugation at 18000 x g for 30 min and passed through a 0.45 µm bottle-top filter
897 before loading onto an equilibrated HisTrap FF column (Cytiva) using an AKTA Pure
898 FPLC instrument. The column was then washed with 10 CV of eIF2α wash buffer (20
899 mM Tris-HCl pH 7.5, 500 mM NaCl) supplemented with 20 mM imidazole and a further
900 5 CV of buffer with 62.5 mM imidazole. Bound proteins were eluted with elution buffer
901 (wash buffer + 250 mM imidazole). The elution fraction was supplemented with 5 mM
902 $MgCl_2$ and 2.5 mM ATP (Sigma) then phosphorylated by addition of 5 µg recombinant
903 GST-PKR (Thermo) for 2 hours at 37 C with gentle stirring. The entire reaction was
904 syringe filtered (0.22 µm filter), concentrated to 1 mL, and purified further by size
905 exclusion chromatography using a Superdex 200 Increase pg 16/600 column.
906 Phosphorylation and purity of the final sample was evaluated by SDS PAGE using a
907 Phos-tag gel (Fujifilm). A typical yield was 2 mg of protein per liter of *E. coli* culture.
908
909 *eIF2α-P*
910
911 eIF2α-P was purified as previously described (*36*). N-terminally 6x-His-tagged human
912 eIF2α was transformed into One-Shot BL21 Star (DE3) chemically competent *E. coli*
913 cells and eIF2α expression was induced with 1 mM IPTG. The culture was grown
914 overnight at 16°C. Cell pellets were then lysed using the EmulsiFlex-C3 in a buffer
915 containing 100 mM HEPES-KOH, pH 7.5, 300 mM KCl, 2 mM dithiothreitol (DTT), 5 mM
916 MgCl2, 5 mM imidazole, 10% glycerol, 0.1% IGEPAL CA-630, and protease inhibitor
917 cocktail. The lysate was clarified at 20,000 rpm for 45 min at 4°C. Clarified lysate was
918 loaded onto a AKTA Pure 5 ml His-Trap FF Crude column, washed in a buffer

919 containing 20 mM HEPES-KOH, pH 7.5, 100 mM KCl, 5% glycerol, 1 mM DTT, 5 mM
920 MgCl2, 0.1% IGEPAL CA-630, and 20 mM imidazole, and eluted with 75 ml linear
921 gradient of 20 mM – 500 mM imidazole. The eIF2α-containing fractions were collected
922 and applied to a MonoQ HR 10/100 GL column equilibrated in a buffer containing 20
923 mM HEPES-KOH pH 7.5, 100 mM KCl, 1 mM DTT, 5% glycerol, and 5 mM MgCl2 for
924 anion exchange. The column was washed in the same buffer, and the protein was
925 eluted with a gradient of 100 mM to 1 M KCl. eIF2α-containing fractions were
926 concentrated with an Amicon Ultra-15 concentrator with a 30 kDa molecular mass
927 cutoff. eIF2α was phosphorylated by incubating the concentrate with 1 mM ATP and 1
928 mg of PKR-GST enzyme (amino acids 252-551) per milligram of eIF2α overnight at
929 4°C. eIF2α-P was then purified on a Superdex 75 10/300 GL column equilibrated in a
930 buffer containing 20 mM HEPES-KOH pH 7.5, 100 mM KCl, 1 mM DTT, 5 mM MgCl2,
931 and 5% glycerol, and concentrated again using an Amicon Ultra-15 concentrator with a
932 10 kDa molecular mass cutoff and the protein was flash frozen in liquid nitrogen and
933 stored at -80°C. Samples were run on a 12.5% PhosTag gel to verify phosphorylation
934 status.
935
936 ***Cryo-EM sample preparation and data collection***

937 eIF2B decamers were assembled on ice for 15 minutes by combining eIF2Bβγδε
938 tetramers (WT or Δ-latch) with eIF2Bα_2 at final concentrations of 12 μM and 9 μM,
939 respectively. Where applicable, ligands were added after complex assembly at the
940 following molar ratios to decamer: 3:1 eIF2α(NTD)-P, 2:1 MBP-AcP10, 15:1 ISRACT-01
941 (0.5% DMSO), 15:1 ISRACT-02 (0.5% DMSO). Following a 30-minute incubation on ice
942 with ligands, samples were vitrified using a Vitrobot Mark IV plunge freezer (Thermo)
943 set to 4 °C and 100% humidity. Quantifoil R 1.2/1.3, 300 mesh 25 nm gold grids were
944 glow discharged using an EasiGlow glow discharger (Pelco) for 30 s at 15 mA
945 immediately before use. 3.5 μL of sample was applied to a grid and excess liquid was
946 removed using dual-side blotting with a blot force of -5 for 1.5 s. The grids were
947 immediately plunged into liquid ethane then transferred to and stored in liquid nitrogen
948 until clipping and imaging. The apo-eIF2B^{WT}, eIF2B^{WT}-AcP10, eIF2B$^{\Delta\text{-latch}}$-ISRACT-01,
949 and eIF2B$^{\Delta\text{-latch}}$-ISRACT-02 datasets were collected using a Glacios TEM (Thermo)
950 operating at 200 keV while apo-eIF2B$^{\Delta\text{-latch}}$ and eIF2B$^{\Delta\text{-latch}}$ -AcP10 datasets were
951 collected using a Titan Krios G4 TEM (Thermo) operating at 300 keV. Both microscopes
952 are equipped with Falcon 4i detectors and SelectrisX energy filters with a slit width of 10
953 eV. The microscope and data collection parameters for each dataset are provided in
954 Supplemental table 1.
955
956 ***Cryo-EM image analysis***

957 The specific details of image analysis are displayed in supplemental figures S1
958 (eIF2B^{WT}), S4 (eIF2B$^{\Delta\text{-latch}}$), S7 (eIF2B^{WT}-AcP10), S12 (eIF2B$^{\Delta\text{-latch}}$-AcP10), S14
959 (eIF2B$^{\Delta\text{-latch}}$-ISRACT-01, eIF2B$^{D\text{-latch}}$-ISRACT-02) and CryoSPARC workflow files are
960 available at https://github.com/udalwadi/latch-helix. For all datasets, patch-based global
961 and local motion correction, and patch CTF estimation were performed within
962 CryoSPARC live (Structura Biotechnology) using default settings. All subsequent image
963 analysis was carried out using CryoSPARC v4.2 or newer (*91*). For the apo eIF2B^{WT}

964 dataset, particles were initially picked with the blob picker using a particle diameter
965 range of 160-220 Å and minimum separation distance of 0.7 diameters. Particles were
966 extracted with a box size of 512 pixels and Fourier cropped to 400 pixels, then
967 subjected to 2D classification into 50 classes with default settings. 2D classes
968 resembling eIF2B were selected, then used for template-based particle picking for all
969 datasets in this study, with a particle diameter of 220 Å. For all datasets, template-
970 picked particles were extracted and subjected to one round of 2D classification to
971 remove non-particles then subjected to *ab initio* reconstruction and heterogenous
972 refinement into multiple classes. Particles from the best-refining classes were subjected
973 to homogenous refinement with global and local CTF-refinement to generate the
974 consensus map for each dataset. The refined particles were then subjected to 3D
975 classification and 3DVA, where applicable, and each 3D class was refined further by
976 homogenous refinement and used for subsequent model building.
977
978
979 ***Model building, refinement, and analysis***

980 The initial apo eIF2B^{WT} A-state structural model was generated starting by global
981 relaxation of 7L7G into the map using ISOLDE (*92*) within UCSF ChimeraX (*93*) by
982 running the simulation with simple distance restraints enabled. Each chain and residue
983 were then manually refined to fit the experimental map and the residues comprising the
984 latch-helix were manually built and fit. This model was then used as a starting template
985 to build into all subsequent experimental maps containing eIF2B following the same
986 procedure. Models of ISRACT-01 and ISRACT-02 were imported to ChimeraX by their
987 SMILES codes, parameterized using ISOLDE and fit manually into observed cryo-EM
988 density. An AlphaFold prediction of the human uridine cytidine kinase UCK1 that shares
989 homology with AcP10 (*71*) was used as a template to build the structure into the
990 experimental density maps containing AcP10. A final refinement of all models was
991 carried out against half-maps using Servalcat (*94*) and the resulting statistics are
992 reported in **Supplemental table 1**. Experimental structures are deposited to the
993 wwPDB with accession codes PDB: 9Y3P, 9Y3U, 9Y3Q, 9Y3T, 9Y3V, 9Y3W, 9Y4B,
994 9Y5S, 9Y5R, 9Y5T, 9Y5U; EDM-72462, 72467, 72463, 72466, 72468, 72499, 72477,
995 72521, 72520, 72522, 72523. Measurements of all reported structural features were
996 done using the 'distance' command in ChimeraX between alpha-carbons of the
997 appropriate residues. All figures and movies including cryo-EM maps and models were
998 generated using ChimeraX.
999
1000 ***Targeted reanalysis of hydrogen-deuterium exchange coupled to mass***
1001 ***spectrometry on eIF2B to measure latch-helix dynamics***

1002 Hydrogen-deuterium exchange coupled to mass spectrometry (HDX-MS) datasets
1003 generated by Lawrence *et al.* (*67*) were mined to obtain measurements of relative latch-
1004 helix dynamics when eIF2B is in the apo-state compared to when it is stabilized in either
1005 the A-state (apo-eIF2B versus eIF2B:NSs complex) or the I-state (apo-eIF2B versus
1006 eIF2B:eIF2-P complex). The difference in deuteration levels (ΔD) of all detected
1007 peptides (n = 5) corresponding to different regions within amino acids 108 - 141 of
1008 eIF2Bβ at each exchange time point were plotted. Positive values represent peptides

1009 with less deuteration (more solvent protection) in eIF2B complexes with NSs/eIF2-P
1010 than in apo-eIF2B in isolation. Negative values represent peptides with more
1011 deuteration (less solvent protection) in eIF2B complexes with NSs/eIF2-P than in apo-
1012 eIF2B in isolation.
1013
1014 ***In vitro guanine nucleotide exchange assay***

1015 The nucleotide exchange activity of eIF2B was measured as either the loading of
1016 BODIPY-GDP to eIF2 ('loading') or subsequent exchange of GDP for BODIPY-GDP
1017 ('unloading') and the measurement is indicated in each relevant figure. Purified eIF2
1018 (100 nM) was incubated with 100 nM BODIPY-FL-GDP (Thermo Fisher Scientific) in
1019 assay buffer (100 mM HEPES-KOH (pH 7.5), 100 mM KCl, 5 mM $MgCl_2$, 1 mM TCEP
1020 and 1 mg/mL bovine serum albumin) to a volume of 500 µl in a black-walled 1.5-ml tube.
1021 eIF2B decamers were assembled for >45 minutes at room temperature with a molar
1022 ratio of eIF2Bβδγε tetramers to eIF2Bα dimers of 1.5 : 2.0. 10x concentrated GEF
1023 mixes were assembled with 100 mM eIF2B and a 10x concentration of any ligand as
1024 indicated in individual figures. 18 µL per well of the eIF2 - BODIPY-GDP - BSA mix was
1025 added to 384-square-well, black-walled, clear-bottom polystyrene assay plates (Corning
1026 #3766) and a baseline fluorescence intensity was measured for 30 seconds using a
1027 Clariostar Plus (BMG LabTech) plate reader (λ_{Ex} 497 nm, λ_{Em} 525 nm). 2 µl of the 10×
1028 GEF mixes were then spiked into the 384-well plate wells with a multichannel pipette to
1029 achieve the final concentration of proteins and drugs as indicated in each figure.
1030 Fluorescence intensity was recorded every 10 s for 60 min at room temperature. For
1031 unloading assays, wells were spiked with 1 mM GDP after completion of the loading
1032 reaction and fluorescence intensity measurement was resumed. Data collected were fit
1033 to a first-order exponential association ('loading') or first-order exponential decay
1034 ('unloading') with Prism (GraphPad) and the reaction half-time after curve fitting are
1035 reported as $t_{1/2}$.
1036
1037 ***FAM-ISRIB fluorescence polarization affinity assay***

1038 All fluorescence polarization measurements were performed in 20 µl reactions with
1039 2.5 nM FAM-ISRIB (Praxis Bioresearch) in FP buffer (20 mM HEPES-KOH (pH 7.5),
1040 100 mM KCl, 5 mM $MgCl_2$ and 1 mM TCEP) and measured in 384-well, non-stick black
1041 plates (Corning, 3820) using a ClarioStar Plus (BMG LabTech) plate reader at room
1042 temperature. Before the reaction setup, eIF2B decamers were assembled in FP buffer
1043 at 10 µM using eIF2Bβγδε and eIF2Bα_2 in a 2:1.5 molar ratio for at least 1 h at 4 °C.
1044 FAM-ISRIB, FAM-ISRACT-01, or FAM-ISRACT-02 were always first diluted to 2.5 µM in
1045 100% NMP before dilution to 50 nM in 2% NMP and then added to the reaction (0.1%
1046 NMP final). eIF2B decamers were serially diluted two-fold 10 times starting from 1.111
1047 µM and the 18 µL of the dilutions were transferred to the 384-well assay plate. 2 µL of
1048 the 50 nM fluorescent compound was then added to each well. The plate was incubated
1049 at room temperature for 30 min before measurement of parallel and perpendicular
1050 intensities (λ_{Ex} 482 nm, λ_{Em} 530 nm).
1051
1052 ***Analytical ultracentrifugation***

1053 Analytical ultracentrifugation sedimentation velocity experiments were performed using
1054 the Optima AUC (Beckman Coulter). Samples were loaded into cells in AUC buffer
1055 (20 mM HEPES-KOH (pH 7.5), 150 mM KCl, 1 mM TCEP and 5 mM $MgCl_2$) at 1 μM for
1056 eIF2Bβδγε tetramers and 0.75 μM for eIF2Bα dimers. A buffer-only reference control
1057 was also loaded. Samples were then centrifuged in an AN 50 Ti rotor at 40,000 r.p.m. at
1058 20 °C, and 280-nm absorbance was monitored for 100 scans every 100 s. Subsequent
1059 data analysis was conducted with Sedfit using a non-model-based continuous c(*S*)
1060 distribution and graphs were generated using Prism (GraphPad).
1061
1062 ***In vitro immunoprecipitation assays***

1063 Assays were performed with a modified protocol from a previous report (*65*). For MBP-
1064 tag pulldowns, purified His-MBP-AcP10, His-MBP-AcP10 mutants, eIF2B$(\alpha\beta\delta\gamma\varepsilon)_2$,
1065 eIF2Bβδγε, eIF2B$(\alpha\beta^{\Delta\text{-latch}}\delta\gamma\varepsilon)_2$, eIF2B$\beta^{\Delta\text{-latch}}\delta\gamma\varepsilon$ and eIF2Bα_2 were incubated (with
1066 gentle rotation at 4°C) with Amylose resin in Assay Buffer (20 mM HEPES-KOH, pH 7.5,
1067 150 mM KCl, 5 mM $MgCl_2$, 1 mM TCEP, 1 mg/ml bovine serum albumin (BSA), 5 mM
1068 $CaCl_2$). After 1 h, the resin was pelleted by benchtop centrifugation and the supernatant
1069 was removed. Resin was washed 3 times with 500 μl of ice cold Assay Buffer before
1070 resin was resuspended in Elution Buffer (Assay Buffer with 5 mM EDTA and 200mM
1071 Maltose) and incubated with gentle rocking for 30 minutes. The resin was then pelleted
1072 and the eluate was incubated with Laemmeli buffer and boiled. Samples were analyzed
1073 by Western Blotting.

1074
1075 For eIF2B pulldowns, purified eIF2Bβδγε tetramers with a Strepavidin-eIF2Bβ were
1076 used. Purified His-MBP-AcP10, His-MBP-AcP10 mutants and preassembled eIF2B^{WT}
1077 decamers were first incubated (with gentle rotation at 4°C) in Assay Buffer (20 mM
1078 HEPES-KOH pH 7.5, 150 mM KCl, 5 mM $MgCl_2$, 1 mM TCEP, 1 mg/ml bovine serum
1079 albumin (BSA), 5 mM $CaCl_2$). After 1 h, eIF2α-P was added to the samples where
1080 indicated for another hour at 4°C. Streptavidin-Sepharose resin was then added to the
1081 mixtures and incubated for a further hour with gentle rotation. The resin was pelleted by
1082 benchtop centrifugation and the supernatant was removed. Resin was washed 3 times
1083 with 500 μl of ice cold Assay Buffer before the resin was resuspended in Elution Buffer
1084 (Assay Buffer with 5 mM EDTA and 2.5 mM Desthiobiotin) and incubated with gentle
1085 rocking for 30 minutes. The resin was then pelleted and the eluate was incubated with
1086 Laemmeli buffer and boiled. Samples were analyzed by Western Blotting.
1087
1088 ***Crosslinking mass spectrometry of AcP10-eIF2B complexes***

1089 **PhoX crosslinking and protein digestion**
1090
1091 His-MBP-AcP10 was incubated with the eIF2B decamer at a molar ratio of 5:1 for 1
1092 hour at 25°C in a final volume of 40 μL. 10% of the input was removed for SDS-Page
1093 analysis, and Disuccinimidyl Phenyl Phosphonic Acid (DSPP or PhoX) was added to
1094 the remaining solution at a final concentration of 1mM. The crosslinking reaction was
1095 carried out at 25°C for 1 hour before quenching with Tris pH 8.5 to a final concentration
1096 of 20 mM. To check cross-linking efficiency, 2.5 μL of each sample (non-crosslinked

1097 and crosslinked) was mixed with 2.5 µL of 2x Laemmli loading buffer containing 5 mM
1098 TCEP (Bond-Breaker). Samples were then heated for 5 minutes at 95°C. 5 µL of the
1099 prepared SDS-PAGE samples were loaded onto a 12-well stain-free 4-15% Criterion
1100 gel. The gel was imaged under UV light using a Bio-Rad ChemiDoc system. Successful
1101 crosslinking was determined by the upward shift of the AcP10 and eIF2B bands.
1102
1103 Protein samples were reduced with 5 mM TCEP for 30 minutes at 37°C on a
1104 ThermoMixer shaking at 1000 rpm. Alkylation was then performed using 15mM 2-
1105 chloroacetamide for 30 minutes in the dark at 25°C on a ThermoMixer shaking at 1000
1106 rpm. Excess 2-chloroacetamide was quenched by DTT at a final concentration of 10mM
1107 and incubating for 30 minutes at 25°C. For protein precipitation, 300µL of cold acetone
1108 was added to each sample and vortexed briefly, followed by overnight precipitation at
1109 −30°C. Precipitated protein was centrifuged at 21,130 x g at 4°C for 20 minutes and
1110 acetone was removed carefully without disturbing the pellet. Samples were airdried for
1111 15 minutes at 25°C and resuspended in 25 µL of 8M Urea, 0.1M Tris pH 8.5. For
1112 digestion, LysC was added at a 1:40 ratio of enzyme:protein sample and incubated at
1113 25°C on a ThermoMixer at 1000rpm for 3 hours. To dilute the urea concentration down
1114 to 1M before trypsin digestion, 175µL of 0.1M Tris pH 8.5 was added to each sample.
1115 Trypsin was then added at a 1:40 enzyme:protein ratio and digested overnight at 25°C.
1116
1117 **Peptide C18 Clean-up and IMAC Enrichment**
1118
1119 Digested peptides were brought to 1% trifluoroacetic acid (TFA) by adding 22.2 µL of
1120 10% TFA in water. Samples were briefly vortexed, and droplets were collected by
1121 centrifugation. 210µL of each sample was then transferred to a LoBind 96-well plate.
1122 200µL of peptide sample was desalted by C18 clean-up performed on an AssayMAP
1123 Bravo automated liquid handling system (Agilent Technologies; Santa Clara, Ca).
1124 Peptides were eluted from the C18 cartridges with 25µL of 80% acetonitrile (ACN) in
1125 0.1% TFA. Crosslinked peptides were enriched on the AssayMAP Bravo using 5µL
1126 Fe(III)-NTA cartridges. The cartridges were primed with 200 µL of 0.1% TFA in ACN
1127 and equilibrated with 200 µL of loading buffer (80% ACN/0.1% TFA). Peptides were
1128 resuspended in a final volume of 210µL 80% ACN/0.1% TFA and 200µL was loaded
1129 onto the cartridge. The cartridges were washed with 50 µL of 80% ACN/0.1% TFA, and
1130 the crosslinked peptides were eluted with 25 µL of a 3:1 ratio of H_2O: NH_4OH into a 96-
1131 well LoBind plate containing 25µL of 10% formic acid in H_2O to immediately neutralize
1132 the pH. The plate was immediately dried using a speedvac and stored at -80°C. The
1133 peptides were resuspended in 3% ACN:0.1% formic acid and identified by LC-MS/MS
1134 analyses.
1135
1136 **Database Search**
1137
1138 Spectral raw data files were first processed using MSFragger (version 4.0) with a
1139 FASTA file combining the H. sapiens and E. coli proteomes (downloaded on April 11,
1140 2024, UP000005640 and UP000000625) including the relevant fusion protein
1141 sequences and a list of common contaminant proteins. Cysteine carbamidomethylation
1142 (57.02146) was set as fixed modification. Methionine oxidation (15.9949), protein N-

1143 term acetylation (42.0106), phosphorylation (79.96633 on S, T, Y), and hydrolysed and
1144 Tris-quenched PhoX crosslinker modifications (227.98238 and 331.0457 on K
1145 respectively) were set as dynamic modifications. The proteins identified by MSFragger
1146 were combined into a FASTA file to generate a searchable library that was
1147 subsequently used with the XlinkX node 3.0 of the Proteome Discoverer 3.0 software
1148 (Thermo Fisher Scientific) to identify crosslinked peptides using the noncleavable open
1149 search algorithm. The analysis was performed using cysteine carbamidomethylation as
1150 a fixed modification and methionine oxidation as a variable modification. PhoX
1151 (+209.97181 Da) was set as the crosslinker modification on lysine residue while also
1152 allowing protein N-terminus linkage with the following parameters: minimum peptide
1153 length 5, missed cleavages 2, precursor mass tolerance 10 ppm, fragment mass
1154 tolerance 20 ppm, and 5% FDR on CSM and cross-link levels. The crosslinks were
1155 visualized using the xMAS plugin in ChimeraX.
1156
1157 ***Cell lines and cell culture***
1158
1159 HEK293T (ATCC, CRL-3216), MEFs (gift from R. J. Kaufman, Sanford Burnham Prebys
1160 Medical Research Institute) and BJ fibroblasts (ATCC, CRL-2522) were cultured in
1161 DMEM-high glutamine medium. DMEM media was supplemented with 10% fetal bovine
1162 serum and the cells were maintained at 37 °C and 5% CO2. For the MEF and BJ
1163 fibroblast cell cultures, the DMEM medium was further supplemented with penicillin–
1164 streptomycin antibiotic, sodium pyruvate and non-essential amino-acid mixtures. The
1165 HEK293T cells were seeded in poly-L-lysine–treated plates. The cells were cultured to
1166 approximately 75–90% confluency for most experiments. Each cell line was routinely
1167 screened for mycoplasma contamination by the Tissue Culture Hub at Altos-BAI.
1168 HEK293T and BJ fibroblast cells from ATCC were authenticated by short-tandem-
1169 repeat profiling.
1170
1171 ***Transfection***
1172
1173 HEK293T cells were transfected with plasmid vectors using the TransIT-2020
1174 transfection reagent for 24 hours. Lipofectamine RNAiMax was used to carry out siRNA
1175 treatments in HEK293T cells for 72 hours. For co-expression of eIF2Bβ siRNA and
1176 eIF2Bβ siRNA resistant plasmids, HEK293T cells were first transfected in suspension
1177 with eIF2Bβ siRNA using Lipofectamine RNAiMax for 24 hours. The next day, the cell
1178 culture media was replaced with fresh media containing the eIF2Bβ siRNA resistant
1179 plasmid:TransIT-2020 mixture and cells were cultured for a further 48
1180 hours. Expression or knockdown efficiencies were checked in parallel for every
1181 experiment by immunoblotting. The eIF2Bβ siRNA sequence is provided in
1182 Supplementary Table 3. Plasmids with ORFs expressing AcP10, AcP10 mutants, NSs
1183 and siRNA resistant eIF2Bβ^{WT} and eIF2Bβ$^{\Delta\text{-latch}}$ were sequenced and verified before
1184 use. The ORF sequences are provided in Supplementary Table 3.
1185
1186 ***Puromycin pulse–chase assays***
1187

1188 Assays were performed as previously reported (*95*). Cells were treated with 2 μg/ml
1189 puromycin for 10 min, followed by puromycin wash out with PBS. The cells were chased
1190 with complete medium with or without the indicated stressor for 50 min, washed with
1191 PBS and lysed with RIPA buffer (1% Triton X-100, 20 mM Tris–HCl pH 8.0, 0.1% SDS,
1192 0.05% sodium deoxycholate, 150 mM NaCl, 10 mM Na3VO4, 40 mM β-
1193 glycerophosphate and 10 mM NaF). The lysates were then subjected to
1194 immunoblotting.
1195
1196 ***ISR activation assays with sodium arsenite***
1197
1198 HEK293T cells were treated with 50 μM of sodium arsenite (LabChem Cat.
1199 No.LC229001) dissolved in DMEM media supplemented with 10% FCS for 4 hours to
1200 induce the ISR.
1201
1202 ***Cell-extract preparation and immunoblotting***
1203
1204 Cells were washed three times with PBS and immediately collected at 4 °C in RIPA lysis
1205 buffer containing phosphatase inhibitors (1% Triton X-100, 20 mM Tris–HCl pH 8.0,
1206 0.1% SDS, 0.05% sodium deoxycholate, 150 mM NaCl, 10 mM Na3VO4, 40 mM β-
1207 glycerophosphate and 10 mM NaF) and complete protease inhibitors (Roche). The
1208 detergent-soluble supernatant fractions were immediately processed for SDS–PAGE
1209 and immunoblotting with antibodies. A list of antibodies used in this study are provided
1210 in Supplementary Table 4.
1211
1212 ***IncuCyte caspase assay***

1213 BJ fibroblasts were seeded in 96-well plates with 100 μL EMEM (ATCC, 30-2003)
1214 supplemented with 10% FBS (Omega Scientific, FB-01), 1x GlutaMAX (Thermo Fisher
1215 Scientific, 35050061), and 1x MEM non-essential amino acid (Thermo Fisher Scientific,
1216 11140035). The following day, the medium was changed to 80 μL of medium
1217 supplemented either with ISRIB (200 nM), ISRACT-01 (3 μM), or the control medium
1218 without ISRIB and ISRACT-01. After 4 hours of pre-incubation with ISRIB or ISRACT-
1219 01, tunicamycin treatment was started by adding 20 μL of the medium supplemented
1220 with tunicamycin (5 μM) and reagents for Incucyte analyses: Incucyte Caspase-3/7 Dye
1221 for Apoptosis (Sartorius, 4804, 1:1000 dilution) and Incucyte Nuclight Rapid NIR Dye for
1222 Live-Cell Nuclear Labelling (Sartorius, 4440, 1:1000 dilution). The final concentrations
1223 of the compounds were 1 μM for tunicamycin, 160 nM for ISRIB, and 2.4 μM for
1224 ISRACT-01. Immediately, the 96-well plates were placed in the Incucyte S3 Live-Cell
1225 Analysis System (Sartorius), and the cells were recorded with the 10X objective every 2
1226 hours for 5 days (excluding one time point every 24 hours). Using Incucyte Analysis
1227 Software (Sartorius), Caspase 3/7 intensity of each well was obtained as the area with
1228 the signal above a cutoff for Incucyte Caspase-3/7 Dye divided by the total cell count
1229 obtained from the Incucyte Nuclight Rapid NIR Dye.
1230
1231 ***Polysome profiling***

1232 Ribosome profiling was performed as we previously described with some modifications
1233 (*64*). Briefly, we prepared fresh 12 ml of 10 – 50% (m/v) sucrose gradients [20 mM Tris-
1234 HCl (pH 8), 5 mM $MgCl_2$, 150 mM KCl] in open-top Polyclear tubes (Seton Scientific,
1235 9/16x3-3/4 inch) with gradient master that comes with the fractionator (Biocomp; we
1236 used the long-cap protocol to accommodate the lysate volume). Gradients were kept at
1237 4 °C for at least 30 min before use. WT mouse fibroblasts in 15-cm dishes at ~80%
1238 confluency were treated with vehicle (DMSO), thapsigargin (50nM) or ISRACT-01
1239 (10μM) for 30 min before subject to a wash with cold PBS and lysis in 3x polysome lysis
1240 buffer [1x concentrations: 20 mM Tris-HCl (pH 8), 5 mM $MgCl_2$, 150 mM KCl, 1 mM
1241 DTT, 1% NP-40, 100 μg/ml cycloheximide, and EDTA-free protease inhibitors (Roche
1242 Indianapolis, IN)] and centrifuged at 14,000 rpm for 10 min at 4 °C. The supernatant
1243 was transferred to a pre-chilled tube. We normalized the input amount by RNA
1244 concentration measured by qubit (RNA broad range kit, Fisher Scientific). The
1245 supernatant was layered onto sucrose gradient carefully. Gradients were centrifuged in
1246 a SW-40Ti rotor at 40,000 rpm at 4 °C for 2 hr and then analyzed by piston gradient
1247 fractionator (Biocomp) and the absorbance of the material was monitored and recorded
1248 using Triax flow cell. Ribosome profile traces were then plotted using Prism
1249 (GraphPad).
1250
1251 ***Chemical synthesis***

1252 Visual schematics of chemical synthesis are provided in Fig. S13.
1253
1254 *ISRACT-01*
1255
1256 *Step 1*. Tert-butyl N-[trans-4-[N-benzyl-2-(4-
1257 chlorophenoxy)acetamido]cyclohexyl]carbamate

1258 To a stirred solution of tert-butyl N-[trans-4-(benzylamino)cyclohexyl]carbamate (3.00 g,
1259 9.85 mmol, 1.00 equiv) and TEA (2.99 g, 29.6 mmol, 3.00 equiv) in DCM (30 mL) was
1260 added 4-chlorophenoxyacetyl chloride (2.22 g, 10.8 mmol, 1.10 equiv) at 0 °C. The
1261 reaction was stirred for 2 h at 0 °C. The reaction was quenched with water (40 mL). The
1262 resulting mixture was extracted with DCM (2 x 40 mL). The combined organic layers
1263 were washed with brine (30 mL), dried over anhydrous Na_2SO_4. After filtration, the
1264 filtrate was concentrated under reduced pressure to give tert-butyl N-[trans-4-[N-benzyl-
1265 2-(4-chlorophenoxy)acetamido]cyclohexyl]carbamate (3.70 g, 79% yield) as a white
1266 solid. LCMS (ES, m/z): 473.20, 475.20 $[M+H]^+$

1267 *Step 2*. N-benzyl-2-(4-chlorophenoxy)-N-[trans-4-aminocyclohexyl]acetamide
1268 hydrochloride

1269 To a stirred solution of tert-butyl N-[trans-4-[N-benzyl-2-(4-
1270 chlorophenoxy)acetamido]cyclohexyl]carbamate (2.00 g, 4.23 mmol, 1.00 equiv) in ethyl
1271 acetate (10 mL) was added HCl (4 M in 1,4-dioxane) (10.6 mL, 42.3 mmol, 10.0 equiv)
1272 at 25 °C. The reaction was stirred for 2 h at 25 °C. The mixture was concentrated and
1273 washed with Et_2O (20 mL) to give N-benzyl-2-(4-chlorophenoxy)-N-[trans-4-

aminocyclohexyl]acetamide hydrochloride (1.5 g, 87% yield) as a white solid. LCMS (ES, m/z): 373.20, 375.20 $[M-HCl+H]^+$

Step 3. 3-(4-Chlorophenoxy)-N-[trans-4-[N-benzyl-2-(4-chlorophenoxy)acetamido]cyclohexyl]propanamide

To a stirred solution of N-benzyl-2-(4-chlorophenoxy)-N-[trans-4-aminocyclohexyl]acetamide hydrochloride (2.00 g, 4.90 mmol, 1.00 equiv) and 3-(4-chlorophenoxy)propanoic acid (1.18 g, 5.88 mmol, 1.20 equiv) in DMF (20 mL) was added DIEA (1.88 g, 14.7 mmol, 3.00 equiv) and HATU (2.42 g, 6.37 mmol, 1.30 equiv) at 25 °C. The reaction was stirred for 2 h at 25 °C. The reaction was purified by reversed flash chromatography (column: C18 column, 120 g, 20-35 μm; mobile phase, A: water (10 mM NH_4HCO_3) and B: ACN (0% to 75% gradient in 30 min); detector: 254/220 nm). The collected fraction was lyophilized to give 3-(4-chlorophenoxy)-N-[trans-4-[N-benzyl-2-(4-chlorophenoxy)acetamido]cyclohexyl]propanamide (1.08 g, 36% yield, 98.8% purity) as a white solid.

ISRACT-02

Step 1. 2-(4-Chlorophenoxy)-N-[trans-4-[(pyridin-4-ylmethyl)amino]cyclohexyl]acetamide

To a stirred solution of 2-(4-chlorophenoxy)-N-[trans-4-aminocyclohexyl]acetamide (440 mg, 1.56 mmol, 1.00 equiv) in DCM (5.0 mL) was added 4-formylpyridine (168 mg, 1.56 mmol, 1.00 equiv) and AcOH (9.4 mg, 0.156 mmol, 0.10 equiv) at 25 °C. The reaction was stirred for 0.5 h at 25 °C. Then STAB (996 mg, 4.68 mmol, 3.00 equiv) was added and the mixture was stirred for 2 h at 25 °C. The reaction was quenched with water (20 mL). The mixture was extracted with DCM (2 x 20 mL). The combined organic layers were washed with brine (30 mL), dried over anhydrous Na_2SO_4. After filtration, the filtrate was concentrated under reduced pressure. The crude product was purified by silica gel column, eluting with PE/EA (1:2) to afford 2-(4-chlorophenoxy)-N-[trans-4-[(pyridin-4-ylmethyl)amino]cyclohexyl]acetamide (300 mg, 50% yield) as a white solid. LCMS (ES, m/z):374.15, 376.15 $[M+H]^+$

Step 2. 3-(4-Chlorophenoxy)-N-(pyridin-4-ylmethyl)-N-[trans-4-[2-(4-chlorophenoxy)acetamido]cyclohexyl]propanamide

To a solution of 2-(4-chlorophenoxy)-N-[trans-4-[(pyridin-4-ylmethyl)amino]cyclohexyl]acetamide (240 mg, 0.642 mmol, 1.00 equiv), 3-(4-chlorophenoxy)propanoic acid (193 mg, 0.963 mmol, 1.50 equiv) in DCM (4.0 mL) was added HOBt (173 mg, 1.28 mmol, 2.00 equiv) and EDCI (185 mg, 0.963 mmol, 1.50 equiv) at 25°C. The reaction was stirred for 2 h at 25 °C and concentrated under reduced pressure. The residue was purified by reversed flash chromatography (column: C18 column, 40 g, 20-35 μm; mobile phase, A: water (10 mM NH_4HCO_3) and B: ACN (10% to 70% gradient in 40 min); detector: 254/220 nm). The collected fraction was lyophilized to afford 3-(4-chlorophenoxy)-N-(pyridin-4-ylmethyl)-N-[trans-4-[2-(4-

1313 chlorophenoxy)acetamido]cyclohexyl]propanamide (41.0 mg, 11% yield, 97.3% purity)
1314 as a white solid.

1315 ***Data Reproducibility***

1316 The number of replicates for each experiment are ≥ 2 and statistical parameters for
1317 each experiment are listed in the corresponding figure legends. No statistical methods
1318 were used to pre-determine sample sizes. Data distribution was assumed to be normal,
1319 but this was not formally tested. Experimental design and data collection was
1320 randomized. For each experiment with multiple conditions, recombinant protein
1321 preparations or cultured cells were from the same batch and allocated at random in
1322 test-tubes or culture dishes. The independent variable was controlled by direct
1323 manipulation. All other sources of extraneous variability were controlled by
1324 randomization or chance. As a collaborative study, each investigator was blinded from
1325 experiments and data collection conducted by every other investigator. Data collection
1326 and analysis by an individual investigator was however not performed blind to the
1327 conditions of the experiments. For the densitometric analysis of western blots, protein
1328 bands on membranes were captured on a BioRad Chemidoc Touch or a LI-COR
1329 Chemidoc apparatus. The exposure times were varied to obtain appropriate signal
1330 intensities of the protein bands. The intensities of each of the bands were quantitated
1331 using the Image-J gel analysis tool.
1332

Supplementary Figure Legends

Fig S1. Cryo-EM analysis and structural modeling of eIF2B
(A) Representative micrographs from two datasets of apo-eIF2B. (B) Data processing pipeline employed for both datasets to generate a 2.6 Å consensus map of eIF2B. Steps prior to 2D classification were carried out using CryoSPARC live and all subsequent steps were done using CryoSPARC v4.4+. (C) 3D classification of particles used to generate the consensus map into 10 classes and subsequent homogenous refinement of volumes. Distribution of particles into each class are indicated below the class images. The reported interface distances were measured between Cα of βN132 (interface 3) and δR250 (interface 4) from structural models of eIF2B fit into every refined map using ISOLDE. Class 1 and Class 7 were designated A-state and I-state, respectively, and were used to generate images for figures within this manuscript. (D) A zoom-in of the density and model of the eIF2Bβ latch-helix with α-helix defining backbone H-bonds indicated by dashed lines. (E) Display of cryo-EM map quality surrounding the areas of interest used to evaluate A- to I-state conformational changes in the eIF2α binding interface, and the latch-helix binding pocket. (F) Fourier shell correlation after FSC mask auto-tightening within CryoSPARC between half-maps of the consensus, class 1, and class 7 maps. Frequency at a correlation of 0.143 was used to determine the map resolutions displayed.

Fig S2. Analysis of A- and I-state structural hallmarks of apo-eIF2B
(A) A zoomed-in view of the ISRIB-binding pocket of two classes of apo-eIF2B in the A-state (class 1; gray) and the I-state (class 7; colored). The location of ISRIB binding is overlaid on the class 1 structure from PDB:7L7G. The symmetry axis between two halves of eIF2B is indicated by a dashed red line and the difference in pocket width is indicated by the dashed arrow. (B) An isolated view of the fulcrum-helix from the class 1 (eIF2Bα: red, eIF2Bδ: tan) and class 7 (gray) structures aligned on the δ-subunit. Key residues and conformation switches are labeled within the panel. (C) A view along the eIF2B tetramer-tetramer interface of the class 1 (A-state, gray), class 7 (I-state, red), and H160D mutant (PDB: 7RLO, green) structures. The (‘) denotes subunits of the opposing tetramer of eIF2B. Arrow depicts conformational change in the H160 rotamer during A- to I- state-transition. (D) Cryo-EM structures of two asymmetrical 3D classes of apo-eIF2B viewed from opposite directions showing the lack of latch-helix density on one side. A- and I-state structural hallmarks of these classes are summarized in Table 2.

Fig S3. HDX-MS analysis of the eIF2B latch-helix.
The difference in the number of deuterons exchanged over time in five peptides encompassing amino acids of the eIF2Bβ latch-helix. apo:NSs - deuteration difference between apo-eIF2B versus NSs-bound eIF2B (A-state); apo:eIF2-P - deuteration difference between apo-eIF2B versus eIF2-P-bound eIF2B (I-state). Values > 0 indicate peptide protection (less deuteration) in the second listed state compared to the first listed state. Values < 0 indicate solvent exposure of peptide (more deuteration) in the second listed state compared to the first listed state.

Fig S4. Cryo-EM analysis and modeling of eIF2B$^{\Delta\text{-latch}}$
(A) Representative micrograph from the dataset of apo eIF2B$^{\Delta\text{-latch}}$. (B) Data processing pipeline employed to generate a 2.1 Å consensus map of eIF2B$^{\Delta\text{-latch}}$. Steps prior to 2D classification were carried out using CryoSPARC live and all subsequent steps were done using CryoSPARC v4.4+. The final consensus map is colored by local resolution following the legend to the left. (C) 3D classification of particles into 8 classes and subsequent heterogenous reconstruction of volumes. Distribution of particles into each class are indicated below the class images. The reported interface distances were measured between Cα of βN132 (interface 3) and δR250 (interface 4) from structural models of eIF2B fit into every refined map using ISOLDE. (D) Class 4 and Class 8 were designated I-state and A-like-state, respectively, and processed further by homogenous refinement. The maps are colored by local resolution following the legend at the bottom. (E) Analysis of cryo-EM map quality surrounding the areas of interest: the eIF2α binding interface, the latch-helix binding pocket, and the fulcrum-helix. (F) Fourier shell correlation after FSC mask auto-tightening within CryoSPARC between half-maps of the consensus, class 4, and class 8 maps. Frequency at a correlation of 0.143 was used to determine the map resolutions displayed.

Fig S5. Evolution of the latch-helix in eIF2Bβ steers the A-state stabilization of eIF2Bα.
(A) MSA of eIF2Bβ, δ, and α subunits generated using the PDB pairwise structural alignment tool and displayed in relation to eIF2Bβ secondary structure using ESPript3. (B) Structural model of human eIF2Bβ colored with a rainbow palette by secondary structure elements. N-terminus, C-terminus, and α-helices 4, 5, and the latch-helix are labeled. (C) Comparison of crystal structures of human mannose-6-phosphate-bound eIF2Bα (PDB: 7KMA, blue) and an archaeal eIF2B-related protein (PDB: 1VB5, violet) with cryo-EM structures of A-state eIF2Bα (olive) and I-state eIF2Bα (gray). Amino acids αL303 and αF75 are highlighted. Arrows chart A- to I-state transitions. (D) The sequences of eIF2Bβ from various eukaryotes and an evolutionarily related archaeal aIF2B aligned to human eIF2Bβ around the latch-helix using Clustal Omega. The alignments are displayed in relation to eIF2Bβ secondary structure using ESPript3. (E) Alignment of eIF2Bα residues comprising the latch-helix binding pocket (denoted with red arrows) aligned using Clustal Omega. The alignments are displayed in relation to eIF2Bα secondary structure using ESPript3.

Fig S6. Binding of NSs to eIF2B maintains latch-helix order
Cryo-EM structure of eIF2B (colored by subunit) in complex with the Sandfly Fever Sicilian Virus protein NSs (blue) (EMD-24535) showing an ordered latch-helix (cyan).

Fig S7. Purification of AcP10 and cryo-EM of AcP10-eIF2B^{WT} complex.
(A) SDS-PAGE and Coomassie staining analysis of overexpressed MBP-AcP10 purified from *E. coli*. (B) Gel filtration chromatogram of MBP-AcP10 purified using a Superdex200 Increase column. (C) Representative micrograph from the dataset of eIF2B^{WT}-MBP-AcP10. (D) Data processing pipeline employed to generate a 2.9 Å consensus map of eIF2B^{WT}-AcP10. Preprocessing represents the following analysis

done using CryoSPARC live: patch motion correction, patch CTF estimation, template picking, particle extraction, and 2D classification. All subsequent steps were done using CryoSPARC v4.4+. The non-uniform refined consensus and 3D classified maps are colored in gray with density for AcP10 highlighted orange. (C) The final map of eIF2B$^{\Delta\text{-latch}}$ with two copies of AcP10 bound (class 1) colored by subunit (left) and by local resolution (right). (D) Particles from classes 1-4 were combined and refined further to generate the eIF2B^{WT}-AcP10 structure. The final map is colored by subunit (left) and by local resolution (right) following the displayed legend. (E) Fourier shell correlation after FSC mask auto-tightening within CryoSPARC between half-maps of the final reconstruction. Frequency at a correlation of 0.143 was used to determine the reported resolution. (F) Analysis of cryo-EM map quality surrounding the areas of interest: the latch-helix and the fulcrum-helix in the A-state. (G) Analysis of cryo-EM map quality and model building surrounding key AcP10 residues as labeled. eIF2B subunits are colored following the same scheme as panel (D).

Fig S8. XL-MS mapping of the eIF2B-AcP10 complex

(A) Preassembled eIF2B decamers (3.75 μM) and MBP-AcP10 (7.5 μM) crosslinked with PhoX (1mM) and subjected to SDS-PAGE electrophoresis followed by Coomassie brilliant blue staining (n=3; Rep - Replicate). (B) Crosslinked samples from (A) were analyzed by mass spectrometry. Crosslinks (dashed lines) across 3 replicates were mapped onto the eIF2B^{WT}-AcP10 structure using the XMAS plugin in Chimera X. (C) Schematic representation of the crosslinks between eIF2Bα and eIF2Bδ with AcP10. Pseudobond distances were calculated based on the consensus structure of eIF2B bound to AcP10 and measure the approximate bond distance created by the Pho-X crosslinker accounting for molecular flexibility.

Fig S9. AcP10 contacts the eIF2-P binding pocket in eIF2B and competes with eIF2α-P.

(A) Schematic representation of the surface area on eIF2B buried by AcP10. AcP10 residues that contact eIF2B are highlighted. (B) *In vitro* pulldowns of preassembled eIF2B$(\alpha\beta\delta\gamma\varepsilon)_2$ (200 nM) with MBP-AcP10 or interface mutants (1 μM). Data are representative of two independent experiments. (C) GEF activity as measured by BODIPY-GDP unloading from eIF2 (100 nM) by eIF2B^{WT} decamers (10 nM) with or without the addition of eIF2α-P (4 μM)/MBP-AcP10, as indicated. Shown are means.e.m. of $t_{1/2}$ values derived from a one-phase decay fit for two experimental replicates. (D) *In vitro* pulldowns of eIF2α-P (0.5 μM) incubated with/without MBP-AcP10^{WT} (2 μM) or MBP-AcP10^{H193A,H200A} (2 μM) using preassembled StrepII-tagged eIF2B$(\alpha\beta\delta\gamma\varepsilon)_2$ decamers (200 nM). Data are representative of two independent experiments.

Fig S10. Convergent evolution of viral ISR inhibitors at targeting a 'hotspot' on eIF2B.

Zoomed-in views of the AcP10-eIF2B interaction interface (top left) compared with the NSs-eIF2B interaction interface (top right). Key residues on AcP10 and NSs contacting eIF2Bα are highlighted. In keeping with the schematic theme introduced in (*69*), cartoons of the AcP10 and NSs aromatic 'fingers' grasping onto an eIF2Bα 'branch' are

shown. AcP10, in addition, presents polar ‘knuckles’ to buttress the adjacent eIF2Bδ ‘branch’.

Fig S11. AcP10 interacts with both eIF2B^{WT} and eIF2B$^{\Delta\text{-latch}}$
(A) *In vitro* pulldowns of purified eIF2Bα_2 (200 nM), eIF2Bβδγε (400 nM), eIF2Bβ$^{\Delta\text{-latch}}$δγε (400 nM), eIF2B$(\alpha\beta\delta\gamma\varepsilon)_2$ (200 nM) or eIF2B$(\alpha\beta^{\Delta\text{-latch}}\delta\gamma\varepsilon)_2$ with MBP-FLAG (1 μM) and MBP-AcP10 (1 μM). Data are representative of two independent experiments.

Fig S12. Cryo-EM of the AcP10-eIF2B$^{\Delta\text{-latch}}$ complex.
(A) Representative micrograph from the dataset of eIF2B$^{\Delta\text{-latch}}$-MBP-AcP10. (B) Data processing pipeline employed to generate a consensus map of eIF2B$^{\Delta\text{-latch}}$-AcP10. Preprocessing represents the following analysis done using CryoSPARC live: patch motion correction, patch CTF estimation, template picking, particle extraction, and 2D classification. All subsequent steps were done using CryoSPARC v4.4+. The consensus map is colored in gray with density for AcP10 highlighted orange. (C) The final map of eIF2B$^{\Delta\text{-latch}}$ with two copies of AcP10 bound (class 1) colored by subunit (left) and by local resolution (right). (D) Fourier shell correlation after FSC mask auto-tightening within CryoSPARC between half-maps of the final reconstruction. Frequency at a correlation of 0.143 was used to determine the reported resolution. (E) Models were fit into volumes from class 1, 2, and 3 from 3D classification and the distance between βN132 and δ’R250 were measured. eIF2 binding interface distances of consensus models of eIF2B^{WT} and eIF2B$^{\Delta\text{-latch}}$ are indicated by dashed lines. (F) Analysis of cryo-EM map quality and model building surrounding key AcP10 residues as labeled for eIF2B bound symmetrically to two AcP10 molecules (class 1) and eIF2B asymmetrically bound to one AcP10 molecule (class 2). Side 1 and Side 2 for class 2 are indicated above in panel (B). eIF2B subunits are colored following the same scheme as panel (D).

Fig S13. Chemical synthesis and diagnostics of ISRACT
(A) The chemical structure of ISRIB, represented as a scaffold with locations of proposed modifications shown in red. (B) Schematic representation of the chemical modifications which produce compounds ISRACT-01 and ISRACT-02. (C) Chemical synthesis workflow employed to generate compound ISRACT-01. (D) Chemical synthesis workflow used to produce compound ISRACT-02. A detailed protocol of chemical synthesis is provided in Materials and Methods.

Fig S14. Cryo-EM of ISRACT compounds in complex with eIF2B.
(A) Representative micrograph from the dataset of ISRACT-01 - eIF2B$^{\Delta\text{-latch}}$. (B) Data processing pipeline employed to generate a consensus map of ISRACT-01 - eIF2B$^{\Delta\text{-latch}}$ complex which had minimal density for the compound in the binding pocket. Pre-processing includes the following analysis done using CryoSPARC live: patch motion correction, patch CTF estimation, template picking, particle extraction, and 2D classification. All subsequent steps were done using CryoSPARC v4.4+. (C) 3D classification of particles into 4 classes and subsequent homogeneous refinement produced one volume with clear compound density. Distribution of particles into each class are indicated below the class images. (D) Representative micrograph from the

1516 dataset of ISRACT-02 - eIF2B$^{\Delta\text{-latch}}$. (E) Data processing pipeline employed to generate
1517 a consensus map of ISRACT-02 - eIF2B$^{\Delta\text{-latch}}$ complex which had compound density in
1518 multiple conformations. Pre-processing includes the following analysis done using
1519 CryoSPARC live: patch motion correction, patch CTF estimation, template picking,
1520 particle extraction, and 2D classification. All subsequent steps were done using
1521 CryoSPARC v4.4+. (F) 3D classification of particles into 4 classes and homogeneous
1522 refinement produced two volumes with clear compound density. Classes 1 and 3 show
1523 clear separation of the two binding poses of the compound. Distribution of particles into
1524 each class are indicated below the class images. (G) Display of cryo-EM map quality
1525 surrounding the compounds in each indicated volume. (H) Fourier shell correlation after
1526 FSC mask auto-tightening within CryoSPARC between half-maps of the ISRACT-01
1527 class 1, ISRACT-02 class 2, and ISRACT-02 class 3 structures. Reciprocal of frequency
1528 at a correlation of 0.143 was used to determine the map resolutions displayed. (I)
1529 Fluorescence polarization-based binding assay to measure binding of fluorescein
1530 conjugated ISRACT-01 and ISRACT-02 to eIF2B^{WT} and eIF2B$^{\Delta\text{-latch}}$. 2 to 2000 nM of
1531 eIF2B decamers were titrated against 2.5 nM of the fluorescent compounds.
1532
1533 **Fig S15. ISRACT-01 promotes adaptation to ER-stress by augmenting**
1534 **cytoprotective ISR activation through inhibition of protein synthesis.**
1535 (A) BJ Fibroblasts pre-treated with 200 nM of ISRIB or 3 μM of ISRACT-01 for 5 hours
1536 followed by addition of 1 μM tunicamycin (Tm). Caspase 3/7 activation and cell counts
1537 were measured and reported as a ratio per well. (B) Polysome gradient analysis upon
1538 treatment with 50 nM thapsigargin. (C) Polysome gradient analysis upon treatment with
1539 10 μM ISRACT-01.
1540
1541 **Supplementary Movies**
1542
1543 **Movie S1. 3D variability analyses of eIF2B motion.**
1544
1545 **Movie S2. Conformational change in eIF2Bβ H160 during A- to I- state transition.**
1546
1547 **Movie S3. Rotation of fulcrum-helix stabilizes the remodeled I-state latch-helix**
1548 **pocket.**
1549
1550 **Movie S4. The allosteric signaling axis regulating eIF2B state-transitions.**
1551
1552
1553
1554

1555 **Supplemental Table 1.1: Cryo-EM data collection, analysis, and refinement**
1556 **statistics of wild-type and Δ-latch eIF2B**
1557

	eIF2B^{WT}		eIF2B$^{\Delta\text{-latch}}$	
	A-state	I-state	I-state	A-state
	PDB: 9Y3P EMD-72462	PDB: 9Y3Q EMD-72463	PDB: 9Y3U EMD-72467	PDB: 9Y3T EMD-72466
Data collection and processing				
Microscope	Thermo Scientific Glacios TEM		Thermo Scientific Krios G4 TEM	
Magnification	130,000x			
Voltage (kV)	200		300	
Election exposure ($e^-/Å^2$)	50			
Defocus range (μm)	-0.6 to -1.6			
Pixel size (Å)	0.8936		0.9286	
Symmetry imposed	C1			
Initial particle images (no.)	890,578		907,870	
Final particle images (no.)	60,012	55,475	96,151	88,960
Map resolution (Å)	2.94	3.30	2.42	2.50
FSC threshold	0.143			
Map resolution range (Å)	2.52-38.2	2.50-42.7	2.05-31.8	2.03-35.7
Refinement				
Initial model used (PDB code)	7L7G	7L7G	7L7G	7L7G
Map sharpening B factor ($Å^2$)	56.3	56.8	47.2	48.4

Model composition				
Nonhydrogen atoms	28946	28563	28169	28492
Protein residues	3709	3709	3613	3657
Ligands	15	15	4	8
Root mean square deviations				
Bond lengths (Å)	0.008	0.0073	0.0078	0.0073
Bond anlges (°)	1.715	1.609	1.625	1.6
Validation				
MolProbity score	1.01	1.13	1.13	1.31
Clashscore	0.81	1.27	1.58	1.74
Poor rotamers (%)	1.27	0.94	1.18	1.32
Ramachandran				
Favoured (%)	96.95	95.86	97.03	95.89
Allowed (%)	3	4	3	4
Disallowed (%)	0.05	0.06	0.03	0.19

1562 **Supplemental Table 1.2: Cryo-EM data collection, analysis, and refinement of**
1563 **wild-type and Δ-latch eIF2B bound to ligands**
1564

	eIF2B^{WT}-AcP10	eIF2B$^{\Delta\text{-latch}}$ – AcP10		eIF2B$^{\Delta\text{-latch}}$ – ISRACT-01	eIF2B$^{\Delta\text{-latch}}$ – ISRACT-02	
	2 AcP10	2 AcP10	1 AcP10	I-state	A-state	I-state
	PDB: 9Y3V EMD-72468	PDB: 9Y4B EMD-72477	PDB: 9Y4W EMD-72499	PDB: 9Y5S EMD-72521	PDB: 9Y5T EMD-72522	PDB: 9Y5U EMD-72523
Data collection and processing						
Microscope	Thermo Scientific Glacios TEM	Thermo Scientific Krios G4 TEM		Thermo Scientific Glacios TEM		
Magnification	130,000x					
Voltage (kV)	200	300		200		
Election exposure (e^-/Å^2)	50					
Defocus range (μm)	-0.6 to -1.6					
Pixel size (Å)	0.8936	0.9286		0.8936		
Symmetry imposed	C1					
Initial particle images (no.)	1,805,332	867,729		2,714,171	2,376,924	
Final particle images (no.)	220,193	171,498	112,494	157,984	418,565	325,317
Map resolution (Å)	2.90	2.13	2.42	3.10	2.78	2.90
FSC threshold	0.143					
Map resolution range (Å)	1.93-34.8	2.08-27.8	2.05-31.7	1.92-39.6	1.93-30.6	1.93-35.0
Refinement						

Initial models used (PDB code)	7L7G, AF-Q9HA47-F1			7L7G		
Map sharpening B factor (Å^2)	100.5	37.4	43.6	82.3	87.4	85.2
Model composition						
Nonhydrogen atoms	32247	32179	30512	28748	28652	28658
Protein residues	4126	4076	3869	3650	3631	3634
Ligands	3	13	10	11	7	5
Root mean square deviations						
Bond lengths (Å)	0.0095	0.0081	0.0076	0.0081	0.0092	0.008
Bond anlges (°)	1.796	1.655	1.607	1.709	1.840	1.71
Validation						
MolProbity score	1.13	0.95	0.95	1.30	1.19	1.28
Clashscore	1.15	1.19	1.04	1.62	1.39	1.58
Poor rotamers (%)	1.48	0.76	0	1.5	1.51	1.50
Ramachandran						
Favoured (%)	97.02	97.4	97.2	96.16	96.9	96.3
Allowed (%)	3	3	3	4	3	4
Disallowed (%)	0.05	0	0.03	0.08	0.03	0.08

1565

1566 **Supplemental Table 2: Apo eIF2B^{WT} 3D classification model A- and I-state**
1567 **analysis**

Class	Particles	Substrate interface		Fulcrum-helix		Latch-helix	
		Side 1	Side 2	Side 1	Side 2	Side 1	Side 2
1	54965	32.8	33.2	A-state	A-state	Present	Present
2	57555	33.4	33.5	A-state	A-state	Absent	Present
3	54977	33.4	33.1	A-state	A-state	Present	Present
4	55271	N/A	N/A	N/A	N/A	N/A	N/A
5	57477	32.7	33.5	A-state	A-state	Present	Absent
6	57885	33.1	33.0	A-state	A-state	Present	Present
7	59301	N/A	N/A	N/A	N/A	N/A	N/A
8	55468	35.7	35.4	I-state/ A-state	I-state/ A-state	Absent	Absent
9	59983	33.3	33.4	A-state	A-state	Present	Present
10	56533	33.9	33.6	A-state	A-state	Present	Present

1568
1569

1570 **Supplemental Table 3: siRNA and plasmid ORF sequences**
1571
1572 **siRNA sequences**
1573

Gene target	siRNA/commercial product
Control siRNA	Mission siRNA Universal Negative control (Sigma-Aldrich Cat #SIC001)
EIF2B2	5'-CCAACATCATTGAGGCGAT-3' (SASI_Hs01_00046766/EIF2B2)

1574
1575 **Plasmid ORF sequences**
1576

Plasmid	ORF
siRNA resistant *eIF2Bβ*^{WT} *-synonymous mutations introduced for siRNA resistance are underlined.	ATGCCGGGATCCGCAGCGAAGGGCTCGGAGTTGTCAGAGAGGATCGAG AGCTTCGTGGAGACCCTGAAGCGGGGTGGTGGGCCGCGCAGCTCCGA GGAAATGGCTCGGGAGACCCTAGGGTTGCTGCGCCAGATCATCACGGA CCACCGCTGGAGCAACGCGGGGGAGCTGATGGAGCTGATCCGCAGAG AGGGCAGGAGGATGACGGCCGCTCAGCCCTCCGAGACCACCGTGGGC AACATGGTGCGGAGAGTGCTCAAGATTATCCGGGAGGAGTATGGCAGA CTCCATGGACGCAGCGACGAGAGTGATCAGCAGGAGTCCCTGCACAAA CTGTTGACATCCGGAGGCCTAAACGAGGATTTCAGCTTCCATTATGCCC AACTCCAGAGCAATATAATCGAAGCCATCAATGAGCTGCTAGTGGAGCT GGAAGGGACAATGGAGAACATTGCAGCCCAGGCTCTGGAGCACATTCA CTCCAATGAGGTGATCATGACCATTGGCTTCTCCCGAACAGTAGAGGCC TTCCTCAAAGAGGCTGCCCGAAAGAGGAAATTCCATGTCATTGTAGCAG AGTGTGCTCCTTTCTGCCAGGGTCATGAAATGGCTGTGAATTTGTCCAAA GCAGGTATTGAGACAACTGTCATGACTGATGCTGCCATTTTTGCCGTTAT GTCAAGAGTCAACAAGGTGATCATTGGCACGAAGACCATCCTGGCCAAT GGGGCCCTGAGAGCTGTGACAGGAACTCACACTCTGGCACTGGCAGCA AAACACCATTCCACCCCACTCATCGTCTGTGCACCTATGTTCAAACTTTC TCCACAGTTCCCCAATGAAGAAGACTCATTTCATAAGTTTGTGGCTCCTG AAGAAGTCCTGCCATTCACAGAAGGGGACATTCTGGAGAAGGTCAGCGT GCATTGCCCTGTGTTTGACTACGTTCCCCCAGAGCTCATTACCCTCTTTA TCTCCAACATTGGTGGGAATGCACCTTCCTACATCTACCGCCTGATGAGT GAACTCTACCATCCTGATGATCATGTTTTA
siRNA resistant *eIF2Bβ*$^{\Delta\text{-latch}}$ *-synonymous mutations introduced for siRNA resistance are underlined.	ATGCCGGGATCCGCAGCGAAGGGCTCGGAGTTGTCAGAGAGGATCGAG AGCTTCGTGGAGACCCTGAAGCGGGGTGGTGGGCCGCGCAGCTCCGA GGAAATGGCTCGGGAGACCCTAGGGTTGCTGCGCCAGATCATCACGGA CCACCGCTGGAGCAACGCGGGGGAGCTGATGGAGCTGATCCGCAGAG AGGGCAGGAGGATGACGGCCGCTCAGCCCTCCGAGACCACCGTGGGC AACATGGTGCGGAGAGTGCTCAAGATTATCCGGGAGGAGTATGGCAGA CTCCATGGACGCggaagtgggagcggaCTAAACGAGGATTTCAGCTTCCATTA TGCCCAACTCCAGAGCAATATAATCGAAGCCATCAATGAGCTGCTAGTG GAGCTGGAAGGGACAATGGAGAACATTGCAGCCCAGGCTCTGGAGCAC ATTCACTCCAATGAGGTGATCATGACCATTGGCTTCTCCCGAACAGTAGA GGCCTTCCTCAAAGAGGCTGCCCGAAAGAGGAAATTCCATGTCATTGTA GCAGAGTGTGCTCCTTTCTGCCAGGGTCATGAAATGGCTGTGAATTTGT

	CCAAAGCAGGTATTGAGACAACTGTCATGACTGATGCTGCCATTTTTGCC GTTATGTCAAGAGTCAACAAGGTGATCATTGGCACGAAGACCATCCTGG CCAATGGGGCCCTGAGAGCTGTGACAGGAACTCACACTCTGGCACTGG CAGCAAAACACCATTCCACCCCACTCATCGTCTGTGCACCTATGTTCAAA CTTTCTCCACAGTTCCCCAATGAAGAAGACTCATTTCATAAGTTTGTGGC TCCTGAAGAAGTCCTGCCATTCACAGAAGGGGACATTCTGGAGAAGGTC AGCGTGCATTGCCCTGTGTTTGACTACGTTCCCCCAGAGCTCATTACCC TCTTTATCTCCAACATTGGTGGGAATGCACCTTCCTACATCTACCGCCTG ATGAGTGAACTCTACCATCCTGATGATCATGTTTTA
AcP10	ATGAAACCCTATATTATTGGGATTTCCGGGATTAGTGGATCTGGTAAATC AACTTTTGCAGCCAATTTGAAAACTAAGTGTGGAGATTTTTACGCTGGGG ATGTTGTGATTATTAATTTAGATGGGTTTTATCGCAGCATTAATGAGGAC GATATGTGCCTTGTTAAAGCTGGTGAGTATAATTTTGATCATCCCTATGC AATAGATTTAGATCATGCACGTAGGTGTATTTCAGCTATAGCTGATGGCC ACCTTGTTGCAGTTCCTATTTATGATTTTGAGAAAAAGAAATGTGTTGGG CACTATGAGGTGAACAACCCTAGAGTAGTGATTGTGGAGGGAATACATG CACTCCACCCCAAGCTTTTTCCATTGTATGATATTACAGCATTTCTAGAG GTACCGATGAGTGTGGCACTTTCTAGACGTGCTGTTAGAGATAATAAAG AAAGAGGTAGAACACCAGAGGATACAGCAGAGATGTTCCGCAAATTTGT TCTCCCCATGTATAAATTACATGTTGAACCCAATGTTAAGAAGGCGGCCA TTCTTGTGAATGGACTAAACACTGGTGTTCATATTAATATGCTCTATGAGC ACATTAAGCCCCTATTGATTTATCCACGCTTT
AcP10 F30A Y31A	ATGAAACCCTATATTATTGGGATTTCCGGGATTAGTGGATCTGGTAAATC AACTTTTGCAGCCAATTTGAAAACTAAGTGTGGAGATGCGGCAGCTGGG GATGTTGTGATTATTAATTTAGATGGGTTTTATCGCAGCATTAATGAGGA CGATATGTGCCTTGTTAAAGCTGGTGAGTATAATTTTGATCATCCCTATG CAATAGATTTAGATCATGCACGTAGGTGTATTTCAGCTATAGCTGATGGC CACCTTGTTGCAGTTCCTATTTATGATTTTGAGAAAAAGAAATGTGTTGG GCACTATGAGGTGAACAACCCTAGAGTAGTGATTGTGGAGGGAATACAT GCACTCCACCCCAAGCTTTTTCCATTGTATGATATTACAGCATTTCTAGA GGTACCGATGAGTGTGGCACTTTCTAGACGTGCTGTTAGAGATAATAAA GAAAGAGGTAGAACACCAGAGGATACAGCAGAGATGTTCCGCAAATTTG TTCTCCCCATGTATAAATTACATGTTGAACCCAATGTTAAGAAGGCGGCC ATTCTTGTGAATGGACTAAACACTGGTGTTCATATTAATATGCTCTATGAG CACATTAAGCCCCTATTGATTTATCCACGCTTTTAA
AcP10 H193A H200A	ATGAAACCCTATATTATTGGGATTTCCGGGATTAGTGGATCTGGTAAATC AACTTTTGCAGCCAATTTGAAAACTAAGTGTGGAGATTTTTACGCTGGGG ATGTTGTGATTATTAATTTAGATGGGTTTTATCGCAGCATTAATGAGGAC GATATGTGCCTTGTTAAAGCTGGTGAGTATAATTTTGATCATCCCTATGC AATAGATTTAGATCATGCACGTAGGTGTATTTCAGCTATAGCTGATGGCC ACCTTGTTGCAGTTCCTATTTATGATTTTGAGAAAAAGAAATGTGTTGGG CACTATGAGGTGAACAACCCTAGAGTAGTGATTGTGGAGGGAATACATG CACTCCACCCCAAGCTTTTTCCATTGTATGATATTACAGCATTTCTAGAG GTACCGATGAGTGTGGCACTTTCTAGACGTGCTGTTAGAGATAATAAAG AAAGAGGTAGAACACCAGAGGATACAGCAGAGATGTTCCGCAAATTTGT TCTCCCCATGTATAAATTACATGTTGAACCCAATGTTAAGAAGGCGGCCA TTCTTGTGAATGGACTAAACACTGGTGTTGCTATTAATATGCTCTATGAG GCTATTAAGCCCCTATTGATTTATCCACGCTTT
AcP10 Y207A F210A	ATGAAACCCTATATTATTGGGATTTCCGGGATTAGTGGATCTGGTAAATC AACTTTTGCAGCCAATTTGAAAACTAAGTGTGGAGATTTTTACGCTGGGG ATGTTGTGATTATTAATTTAGATGGGTTTTATCGCAGCATTAATGAGGAC

	GATATGTGCCTTGTTAAAGCTGGTGAGTATAATTTTGATCATCCCTATGC AATAGATTTAGATCATGCACGTAGGTGTATTTCAGCTATAGCTGATGGCC ACCTTGTTGCAGTTCCTATTTATGATTTTGAGAAAAAGAAATGTGTTGGG CACTATGAGGTGAACAACCCTAGAGTAGTGATTGTGGAGGGAATACATG CACTCCACCCCAAGCTTTTTCCATTGTATGATATTACAGCATTTCTAGAG GTACCGATGAGTGTGGCACTTTCTAGACGTGCTGTTAGAGATAATAAAG AAAGAGGTAGAACACCAGAGGATACAGCAGAGATGTTCCGCAAATTTGT TCTCCCCATGTATAAATTACATGTTGAACCCAATGTTAAGAAGGCGGCCA TTCTTGTGAATGGACTAAACACTGGTGTTCATATTAATATGCTCTATGAGC ACATTAAGCCCCTATTGATTGCTCCACGCGCG
NSs	ATGATGAACAGCCAGTACATGTTTGACTACCCGGCAATTAACATTGATGT GAGGTGTCATAGACTCCTCTCCAGTGTGTCTTATGTTGCCTACAATAAAT TTCACACTCATGACGTTTCAACTTATGAGCATTGTGAAATACCACTAGAG AAGTTAAGACTTGGGTTTGGACGCAGAAACTCACTGGCTGACTTTTATTC CCTTGGAGAGTTGCCAGCTTCTTGGGGCCCAGCATGCTATTTTAGTTCT GTCAAGCCTATGATGTATACCTTCCAAGGTATGGCAAGTGACCTCTCCA GGTTTGACCTCACAAGTTTCTCTAGAAAGGGGCTGCCAAATGTCCTGAA GGCTCTTAGCTGGCCACTAGGTATCCCTGATTGTGAGATCTTTAGCATAT GCAGTGATAGATTTGTGAGAGGGCTACAAACAAGGGATCAGCTAATGTC TTACATTCTGAGAATGGGGGATTCACATAGCTTGGATGAGTGCATAGTTC AGGCACACAAAAAGATACTACAAGAAGCTAGGAGGTTGGGTCTTAGTGA TGAGCATTACAATGGATACGATCTATTTAGAGAGATAGGATCTCTGGTTT GTCTCAGACTTATCAATGCAGAGCCTTTTGACACTGCCTCCTCTGGGGA GGCACTTGATGTAAGAACAGTGATTAGATCCTATAGAGCAAGTGACCCTT CTACTGGCCTCACCGAGTATGGCAATTCTCTTTGGACCCCAATACACAGT CATGTGGATGAAAATGATGAGAGCTCGTCTGACTCTGACTT

1582 **Supplemental Table 4: Immunoblotting antibodies used in this study**

1583

Antibody	SOURCE	IDENTIFIER
eIF2Bα Dilution: 1:3000	Proteintech	(Proteintech Cat# 18010-1-AP, RRID:AB_2261996)
eIF2Bβ Dilution 1:3000	Proteintech	(Proteintech Cat# 11034-1-AP, RRID:AB_2096016)
eIF2Bγ Dilution 1:3000	Proteintech	(Proteintech Cat# 11296-2-AP, RRID:AB_2096142)
eIF2Bδ Dilution: 1:3000	Proteintech	(Proteintech Cat# 11332-1-AP, RRID:AB_2277640)
eIF2Bε Dilution: 1:3000	Santa Cruz Biotech	(Santa Cruz Biotechnology Cat# sc-55558, RRID:AB_831253)
ATF4 Dilution 1:2000	Cell Signaling Technology	(Cell Signaling Technology Cat# 11815, RRID:AB_2616025)
Vinculin Dilution 1:5000	Abcam	(Cell Signaling Technology Cat# 11815, RRID:AB_2616025)
FLAG Dilution: 1:3000	Sigma	(Sigma-Aldrich Cat# F1804, RRID:AB_262044)
MBP Dilution: 1:2000	NEB	(New England Biolabs Cat# E8032, RRID:AB_1559730)
Puromycin	Millipore	

Dilution: 1:1000		(Sigma-Aldrich Cat# MABE343, RRID:AB_2566826)
eIF2α-P Dilution: 1:1000	Abcam	(Abcam Cat# ab32157, RRID:AB_732117)
eIF2α Dilution: 1:1000	Cell Signaling Technology	(Cell Signaling Technology Cat# 9722, RRID:AB_2230924)
GFP Dilution: 1:3000	Santa Cruz Biotech	(Santa Cruz Biotechnology Cat# sc-9996, RRID:AB_627695)
GAPDH Dilution: 1:10000	Proteintech	(Proteintech Cat# 60004-1-Ig, RRID:AB_2107436)

1586 **References**

1587 1. K. Kashiwagi, M. Takahashi, M. Nishimoto, T. B. Hiyama, T. Higo, T. Umehara, K.
1588 Sakamoto, T. Ito, S. Yokoyama, Crystal structure of eukaryotic translation initiation factor
1589 2B. *Nature* **531**, 122–125 (2016).

1590 2. Y. Gordiyenko, C. Schmidt, M. D. Jennings, D. Matak-Vinkovic, G. D. Pavitt, C. V.
1591 Robinson, eIF2B is a decameric guanine nucleotide exchange factor with a γ2ε2 tetrameric
1592 core. *Nat. Commun.* **5**, 3902 (2014).

1593 3. N. C. Wortham, M. Martinez, Y. Gordiyenko, C. V. Robinson, C. G. Proud, Analysis of the
1594 subunit organization of the eIF2B complex reveals new insights into its structure and
1595 regulation. *FASEB J.* **28**, 2225–2237 (2014).

1596 4. A. F. Zyryanova, F. Weis, A. Faille, A. A. Alard, A. Crespillo-Casado, Y. Sekine, H. P.
1597 Harding, F. Allen, L. Parts, C. Fromont, P. M. Fischer, A. J. Warren, D. Ron, Binding of
1598 ISRIB reveals a regulatory site in the nucleotide exchange factor eIF2B. *Science* **359**,
1599 1533–1536 (2018).

1600 5. J. C. Tsai, L. E. Miller-Vedam, A. A. Anand, P. Jaishankar, H. C. Nguyen, A. R. Renslo, A.
1601 Frost, P. Walter, Structure of the nucleotide exchange factor eIF2B reveals mechanism of
1602 memory-enhancing molecule. *Science* **359** (2018).

1603 6. A. Konieczny, B. Safer, Purification of the eukaryotic initiation factor 2-eukaryotic initiation
1604 factor 2B complex and characterization of its guanine nucleotide exchange activity during
1605 protein synthesis initiation. *J. Biol. Chem.* **258**, 3402–3408 (1983).

1606 7. A. G. Rowlands, R. Panniers, E. C. Henshaw, The catalytic mechanism of guanine
1607 nucleotide exchange factor action and competitive inhibition by phosphorylated eukaryotic
1608 initiation factor 2. *J. Biol. Chem.* **263**, 5526–5533 (1988).

1609 8. T. V. Pestova, V. G. Kolupaeva, The roles of individual eukaryotic translation initiation
1610 factors in ribosomal scanning and initiation codon selection. *Genes Dev.* **16**, 2906–2922
1611 (2002).

1612 9. J. R. Lorsch, D. Herschlag, Kinetic dissection of fundamental processes of eukaryotic
1613 translation initiation in vitro. *EMBO J.* **18**, 6705–6717 (1999).

1614 10. T. F. Donahue, A. M. Cigan, E. K. Pabich, B. C. Valavicius, Mutations at a Zn(II) finger
1615 motif in the yeast eIF-2 beta gene alter ribosomal start-site selection during the scanning
1616 process. *Cell* **54**, 621–632 (1988).

1617 11. M. Kozak, The scanning model for translation: an update. *J. Cell Biol.* **108**, 229–241
1618 (1989).

1619 12. R. J. Jackson, C. U. T. Hellen, T. V. Pestova, The mechanism of eukaryotic translation
1620 initiation and principles of its regulation. *Nat. Rev. Mol. Cell Biol.* **11**, 113–127 (2010).

1621 13. M. A. García, E. F. Meurs, M. Esteban, The dsRNA protein kinase PKR: virus and cell
1622 control. *Biochimie* **89**, 799–811 (2007).

1623 14. S. Balachandran, P. C. Roberts, L. E. Brown, H. Truong, A. K. Pattnaik, D. R. Archer, G. N.

1624 Barber, Essential role for the dsRNA-dependent protein kinase PKR in innate immunity to
1625 viral infection. *Immunity* **13**, 129–141 (2000).

1626 15. C. C.-C. Wu, A. Peterson, B. Zinshteyn, S. Regot, R. Green, Ribosome collisions trigger
1627 general stress responses to regulate cell fate. *Cell* **182**, 404-416.e14 (2020).

1628 16. R. Ishimura, G. Nagy, I. Dotu, J. H. Chuang, S. L. Ackerman, Activation of GCN2 kinase by
1629 ribosome stalling links translation elongation with translation initiation. *Elife* **5** (2016).

1630 17. H. P. Harding, Y. Zhang, D. Ron, Protein translation and folding are coupled by an
1631 endoplasmic-reticulum-resident kinase. *Nature* **397**, 271–274 (1999).

1632 18. R. Sood, A. C. Porter, K. Ma, L. A. Quilliam, R. C. Wek, Pancreatic eukaryotic initiation
1633 factor-2alpha kinase (PEK) homologues in humans, Drosophila melanogaster and
1634 Caenorhabditis elegans that mediate translational control in response to endoplasmic
1635 reticulum stress. *Biochem. J.* **346 Pt 2**, 281–293 (2000).

1636 19. A. Subramanian, A. Capalbo, N. R. Iyengar, R. Rizzo, A. di Campli, R. Di Martino, M. Lo
1637 Monte, A. R. Beccari, A. Yerudkar, C. Del Vecchio, L. Glielmo, G. Turacchio, M. Pirozzi, S.
1638 G. Kim, P. Henklein, J. Cancino, S. Parashuraman, D. Diviani, F. Fanelli, M. Sallese, A.
1639 Luini, Auto-regulation of secretory flux by sensing and responding to the folded cargo
1640 protein load in the endoplasmic reticulum. *Cell* **176**, 1461-1476.e23 (2019).

1641 20. L. Lu, A. P. Han, J. J. Chen, Translation initiation control by heme-regulated eukaryotic
1642 initiation factor 2alpha kinase in erythroid cells under cytoplasmic stresses. *Mol. Cell. Biol.*
1643 **21**, 7971–7980 (2001).

1644 21. H. P. Harding, Y. Zhang, H. Zeng, I. Novoa, P. D. Lu, M. Calfon, N. Sadri, C. Yun, B.
1645 Popko, R. Paules, D. F. Stojdl, J. C. Bell, T. Hettmann, J. M. Leiden, D. Ron, An integrated
1646 stress response regulates amino acid metabolism and resistance to oxidative stress. *Mol.*
1647 *Cell* **11**, 619–633 (2003).

1648 22. X. Guo, G. Aviles, Y. Liu, R. Tian, B. A. Unger, Y.-H. T. Lin, A. P. Wiita, K. Xu, M. A.
1649 Correia, M. Kampmann, Mitochondrial stress is relayed to the cytosol by an OMA1-DELE1-
1650 HRI pathway. *Nature* **579**, 427–432 (2020).

1651 23. E. Fessler, E.-M. Eckl, S. Schmitt, I. A. Mancilla, M. F. Meyer-Bender, M. Hanf, J.
1652 Philippou-Massier, S. Krebs, H. Zischka, L. T. Jae, A pathway coordinated by DELE1
1653 relays mitochondrial stress to the cytosol. *Nature* **579**, 433–437 (2020).

1654 24. C. Koumenis, C. Naczki, M. Koritzinsky, S. Rastani, A. Diehl, N. Sonenberg, A. Koromilas,
1655 B. G. Wouters, Regulation of protein synthesis by hypoxia via activation of the
1656 endoplasmic reticulum kinase PERK and phosphorylation of the translation initiation factor
1657 eIF2alpha. *Mol. Cell. Biol.* **22**, 7405–7416 (2002).

1658 25. J. D. Blais, V. Filipenko, M. Bi, H. P. Harding, D. Ron, C. Koumenis, B. G. Wouters, J. C.
1659 Bell, Activating transcription factor 4 is translationally regulated by hypoxic stress. *Mol.*
1660 *Cell. Biol.* **24**, 7469–7482 (2004).

1661 26. H. P. Harding, A. Ordonez, F. Allen, L. Parts, A. J. Inglis, R. L. Williams, D. Ron, The
1662 ribosomal P-stalk couples amino acid starvation to GCN2 activation in mammalian cells.

1663 *Elife* **8** (2019).

1664 27. A. G. Hinnebusch, Translational regulation of GCN4 and the general amino acid control of
1665 yeast. *Annu. Rev. Microbiol.* **59**, 407–450 (2005).

1666 28. J. Ye, M. Kumanova, L. S. Hart, K. Sloane, H. Zhang, D. N. De Panis, E. Bobrovnikova-
1667 Marjon, J. A. Diehl, D. Ron, C. Koumenis, The GCN2-ATF4 pathway is critical for tumour
1668 cell survival and proliferation in response to nutrient deprivation. *EMBO J.* **29**, 2082–2096
1669 (2010).

1670 29. A. J. Inglis, G. R. Masson, S. Shao, O. Perisic, S. H. McLaughlin, R. S. Hegde, R. L.
1671 Williams, Activation of GCN2 by the ribosomal P-stalk. *Proc. Natl. Acad. Sci. U. S. A.* **116**,
1672 4946–4954 (2019).

1673 30. R. Sood, A. C. Porter, D. A. Olsen, D. R. Cavener, R. C. Wek, A mammalian homologue of
1674 GCN2 protein kinase important for translational control by phosphorylation of eukaryotic
1675 initiation factor-2alpha. *Genetics* **154**, 787–801 (2000).

1676 31. T. E. Dever, L. Feng, R. C. Wek, A. M. Cigan, T. F. Donahue, A. G. Hinnebusch,
1677 Phosphorylation of initiation factor 2 alpha by protein kinase GCN2 mediates gene-specific
1678 translational control of GCN4 in yeast. *Cell* **68**, 585–596 (1992).

1679 32. A. G. Hinnebusch, Gene-specific translational control of the yeast GCN4 gene by
1680 phosphorylation of eukaryotic initiation factor 2. *Mol. Microbiol.* **10**, 215–223 (1993).

1681 33. T. Krishnamoorthy, G. D. Pavitt, F. Zhang, T. E. Dever, A. G. Hinnebusch, Tight binding of
1682 the phosphorylated alpha subunit of initiation factor 2 (eIF2alpha) to the regulatory
1683 subunits of guanine nucleotide exchange factor eIF2B is required for inhibition of
1684 translation initiation. *Mol. Cell. Biol.* **21**, 5018–5030 (2001).

1685 34. A. Sudhakar, A. Ramachandran, S. Ghosh, S. E. Hasnain, R. J. Kaufman, K. V. Ramaiah,
1686 Phosphorylation of serine 51 in initiation factor 2 alpha (eIF2 alpha) promotes complex
1687 formation between eIF2 alpha(P) and eIF2B and causes inhibition in the guanine
1688 nucleotide exchange activity of eIF2B. *Biochemistry* **39**, 12929–12938 (2000).

1689 35. M. Costa-Mattioli, P. Walter, The integrated stress response: From mechanism to disease.
1690 *Science* **368**, eaat5314 (2020).

1691 36. L. R. Kenner, A. A. Anand, H. C. Nguyen, A. G. Myasnikov, C. J. Klose, L. A. McGeever, J.
1692 C. Tsai, L. E. Miller-Vedam, P. Walter, A. Frost, eIF2B-catalyzed nucleotide exchange and
1693 phosphoregulation by the integrated stress response. *Science* **364**, 491–495 (2019).

1694 37. K. Kashiwagi, T. Yokoyama, M. Nishimoto, M. Takahashi, A. Sakamoto, M. Yonemochi, M.
1695 Shirouzu, T. Ito, Structural basis for eIF2B inhibition in integrated stress response. *Science*
1696 **364**, 495–499 (2019).

1697 38. P. P. Mueller, A. G. Hinnebusch, Multiple upstream AUG codons mediate translational
1698 control of GCN4. *Cell* **45**, 201–207 (1986).

1699 39. H. P. Harding, I. Novoa, Y. Zhang, H. Zeng, R. Wek, M. Schapira, D. Ron, Regulated
1700 translation initiation controls stress-induced gene expression in mammalian cells. *Mol. Cell*

1701 **6**, 1099–1108 (2000).

1702 40. S. K. Young, R. C. Wek, Upstream open reading frames differentially regulate gene-
1703 specific translation in the integrated stress response. *J. Biol. Chem.* **291**, 16927–16935
1704 (2016).

1705 41. C. Sidrauski, A. M. McGeachy, N. T. Ingolia, P. Walter, The small molecule ISRIB reverses
1706 the effects of eIF2α phosphorylation on translation and stress granule assembly. *Elife* **4**
1707 (2015).

1708 42. P. D. Lu, H. P. Harding, D. Ron, Translation reinitiation at alternative open reading frames
1709 regulates gene expression in an integrated stress response. *J. Cell Biol.* **167**, 27–33
1710 (2004).

1711 43. K. M. Vattem, R. C. Wek, Reinitiation involving upstream ORFs regulates ATF4 mRNA
1712 translation in mammalian cells. *Proc. Natl. Acad. Sci. U. S. A.* **101**, 11269–11274 (2004).

1713 44. J. Han, S. H. Back, J. Hur, Y.-H. Lin, R. Gildersleeve, J. Shan, C. L. Yuan, D. Krokowski,
1714 S. Wang, M. Hatzoglou, M. S. Kilberg, M. A. Sartor, R. J. Kaufman, ER-stress-induced
1715 transcriptional regulation increases protein synthesis leading to cell death. *Nat. Cell Biol.*
1716 **15**, 481–490 (2013).

1717 45. F. Siu, P. J. Bain, R. LeBlanc-Chaffin, H. Chen, M. S. Kilberg, ATF4 is a mediator of the
1718 nutrient-sensing response pathway that activates the human asparagine synthetase gene.
1719 *J. Biol. Chem.* **277**, 24120–24127 (2002).

1720 46. K. Labbé, L. LeBon, B. King, N. Vu, E. H. Stoops, N. Ly, A. E. Y. T. Lefebvre, P. Seitzer, S.
1721 Krishnan, J.-M. Heo, B. Bennett, C. Sidrauski, Specific activation of the integrated stress
1722 response uncovers regulation of central carbon metabolism and lipid droplet biogenesis.
1723 *Nat. Commun.* **15**, 8301 (2024).

1724 47. I. Novoa, H. Zeng, H. P. Harding, D. Ron, Feedback inhibition of the unfolded protein
1725 response by GADD34-mediated dephosphorylation of eIF2alpha. *J. Cell Biol.* **153**, 1011–
1726 1022 (2001).

1727 48. P. D. Lu, C. Jousse, S. J. Marciniak, Y. Zhang, I. Novoa, D. Scheuner, R. J. Kaufman, D.
1728 Ron, H. P. Harding, Cytoprotection by pre-emptive conditional phosphorylation of
1729 translation initiation factor 2. *EMBO J.* **23**, 169–179 (2004).

1730 49. C. Sidrauski, D. Acosta-Alvear, A. Khoutorsky, P. Vedantham, B. R. Hearn, H. Li, K.
1731 Gamache, C. M. Gallagher, K. K.-H. Ang, C. Wilson, V. Okreglak, A. Ashkenazi, B. Hann,
1732 K. Nader, M. R. Arkin, A. R. Renslo, N. Sonenberg, P. Walter, Pharmacological brake-
1733 release of mRNA translation enhances cognitive memory. *Elife* **2**, e00498 (2013).

1734 50. A. Fogli, R. Schiffmann, E. Bertini, S. Ughetto, P. Combes, E. Eymard-Pierre, C. R.
1735 Kaneski, M. Pineda, M. Troncoso, G. Uziel, R. Surtees, D. Pugin, M.-P. Chaunu, D.
1736 Rodriguez, O. Boespflug-Tanguy, The effect of genotype on the natural history of eIF2B-
1737 related leukodystrophies. *Neurology* **62**, 1509–1517 (2004).

1738 51. P. A. Leegwater, G. Vermeulen, A. A. Könst, S. Naidu, J. Mulders, A. Visser, P.
1739 Kersbergen, D. Mobach, D. Fonds, C. G. van Berkel, R. J. Lemmers, R. R. Frants, C. B.

1740 Oudejans, R. B. Schutgens, J. C. Pronk, M. S. van der Knaap, Subunits of the translation
1741 initiation factor eIF2B are mutant in leukoencephalopathy with vanishing white matter. *Nat.*
1742 *Genet.* **29**, 383–388 (2001).

1743 52. B. van Kollenburg, J. van Dijk, J. Garbern, A. A. M. Thomas, G. C. Scheper, J. M. Powers,
1744 M. S. van der Knaap, Glia-specific activation of all pathways of the unfolded protein
1745 response in vanishing white matter disease. *J. Neuropathol. Exp. Neurol.* **65**, 707–715
1746 (2006).

1747 53. W. Li, X. Wang, M. S. Van Der Knaap, C. G. Proud, Mutations linked to
1748 leukoencephalopathy with vanishing white matter impair the function of the eukaryotic
1749 initiation factor 2B complex in diverse ways. *Mol. Cell. Biol.* **24**, 3295–3306 (2004).

1750 54. Y. L. Wong, L. LeBon, A. M. Basso, K. L. Kohlhaas, A. L. Nikkel, H. M. Robb, D. L.
1751 Donnelly-Roberts, J. Prakash, A. M. Swensen, N. D. Rubinstein, S. Krishnan, F. E.
1752 McAllister, N. V. Haste, J. J. O'Brien, M. Roy, A. Ireland, J. M. Frost, L. Shi, S. Riedmaier,
1753 K. Martin, M. J. Dart, C. Sidrauski, eIF2B activator prevents neurological defects caused by
1754 a chronic integrated stress response. *Elife* **8** (2019).

1755 55. N. Ghaddar, S. Wang, B. Woodvine, J. Krishnamoorthy, V. van Hoef, C. Darini, U.
1756 Kazimierczak, N. Ah-Son, H. Popper, M. Johnson, L. Officer, A. Teodósio, M. Broggini, K.
1757 K. Mann, M. Hatzoglou, I. Topisirovic, O. Larsson, J. Le Quesne, A. E. Koromilas, The
1758 integrated stress response is tumorigenic and constitutes a therapeutic liability in KRAS-
1759 driven lung cancer. *Nat. Commun.* **12**, 4651 (2021).

1760 56. K. M. Rouschop, L. J. Dubois, T. G. Keulers, T. van den Beucken, P. Lambin, J. Bussink,
1761 A. J. van der Kogel, M. Koritzinsky, B. G. Wouters, PERK/eIF2α signaling protects therapy
1762 resistant hypoxic cells through induction of glutathione synthesis and protection against
1763 ROS. *Proc. Natl. Acad. Sci. U. S. A.* **110**, 4622–4627 (2013).

1764 57. L. R. Palam, J. Gore, K. E. Craven, J. L. Wilson, M. Korc, Integrated stress response is
1765 critical for gemcitabine resistance in pancreatic ductal adenocarcinoma. *Cell Death Dis.* **6**,
1766 e1913 (2015).

1767 58. T. Ma, M. A. Trinh, A. J. Wexler, C. Bourbon, E. Gatti, P. Pierre, D. R. Cavener, E. Klann,
1768 Suppression of eIF2α kinases alleviates Alzheimer's disease-related plasticity and memory
1769 deficits. *Nat. Neurosci.* **16**, 1299–1305 (2013).

1770 59. M. M. Oliveira, M. V. Lourenco, F. Longo, N. P. Kasica, W. Yang, G. Ureta, D. D. P.
1771 Ferreira, P. H. J. Mendonça, S. Bernales, T. Ma, F. G. De Felice, E. Klann, S. T. Ferreira,
1772 Correction of eIF2-dependent defects in brain protein synthesis, synaptic plasticity, and
1773 memory in mouse models of Alzheimer's disease. *Sci. Signal.* **14**, eabc5429 (2021).

1774 60. A. Flury, L. Aljayousi, H.-J. Park, M. Khakpour, J. Mechler, S. Aziz, J. D. McGrath, P.
1775 Deme, C. Sandberg, F. González Ibáñez, O. Braniff, T. Ngo, S. Smith, M. Velez, D. M.
1776 Ramirez, D. Avnon-Klein, J. W. Murray, J. Liu, M. Parent, S. Mingote, N. J. Haughey, S.
1777 Werneburg, M.-È. Tremblay, P. Ayata, A neurodegenerative cellular stress response linked
1778 to dark microglia and toxic lipid secretion. *Neuron* **113**, 554-571.e14 (2025).

1779 61. R. C. C. Chang, A. K. Y. Wong, H.-K. Ng, J. Hugon, Phosphorylation of eukaryotic initiation
1780 factor-2alpha (eIF2alpha) is associated with neuronal degeneration in Alzheimer's disease.

Neuroreport **13**, 2429–2432 (2002).

62. T. O'Connor, K. R. Sadleir, E. Maus, R. A. Velliquette, J. Zhao, S. L. Cole, W. A. Eimer, B. Hitt, L. A. Bembinster, S. Lammich, S. F. Lichtenthaler, S. S. Hébert, B. De Strooper, C. Haass, D. A. Bennett, R. Vassar, Phosphorylation of the translation initiation factor eIF2alpha increases BACE1 levels and promotes amyloidogenesis. *Neuron* **60**, 988–1009 (2008).

63. A. Chou, K. Krukowski, T. Jopson, P. J. Zhu, M. Costa-Mattioli, P. Walter, S. Rosi, Inhibition of the integrated stress response reverses cognitive deficits after traumatic brain injury. *Proc. Natl. Acad. Sci. U. S. A.* **114**, E6420–E6426 (2017).

64. P. J. Zhu, S. Khatiwada, Y. Cui, L. C. Reineke, S. W. Dooling, J. J. Kim, W. Li, P. Walter, M. Costa-Mattioli, Activation of the ISR mediates the behavioral and neurophysiological abnormalities in Down syndrome. *Science* **366**, 843–849 (2019).

65. M. Schoof, M. Boone, L. Wang, R. Lawrence, A. Frost, P. Walter, eIF2B conformation and assembly state regulate the integrated stress response. *Elife* **10** (2021).

66. A. F. Zyryanova, K. Kashiwagi, C. Rato, H. P. Harding, A. Crespillo-Casado, L. A. Perera, A. Sakamoto, M. Nishimoto, M. Yonemochi, M. Shirouzu, T. Ito, D. Ron, ISRIB Blunts the Integrated Stress Response by Allosterically Antagonising the Inhibitory Effect of Phosphorylated eIF2 on eIF2B. *Mol Cell* **81**, 88-103.e6 (2021).

67. R. E. Lawrence, S. R. Shoemaker, A. Deal, S. Sangwan, A. A. Anand, L. Wang, S. Marqusee, P. Walter, A helical fulcrum in eIF2B coordinates allosteric regulation of stress signaling. *Nat. Chem. Biol.* **20**, 422–431 (2024).

68. J. D. Wuerth, M. Habjan, M. Kainulainen, B. Berisha, D. Bertheloot, G. Superti-Furga, A. Pichlmair, F. Weber, EIF2B as a target for viral evasion of PKR-mediated translation inhibition. *MBio* **11** (2020).

69. M. Schoof, L. Wang, J. Z. Cogan, R. E. Lawrence, M. Boone, J. D. Wuerth, A. Frost, P. Walter, Viral evasion of the integrated stress response through antagonism of eIF2-P binding to eIF2B. *Nat. Commun.* **12**, 7103 (2021).

70. K. Kashiwagi, Y. Shichino, T. Osaki, A. Sakamoto, M. Nishimoto, M. Takahashi, M. Mito, F. Weber, Y. Ikeuchi, S. Iwasaki, T. Ito, eIF2B-capturing viral protein NSs suppresses the integrated stress response. *Nat. Commun.* **12**, 7102 (2021).

71. H. H. Rabouw, L. J. Visser, T. C. Passchier, M. A. Langereis, F. Liu, P. Giansanti, A. L. W. van Vliet, J. G. Dekker, S. G. van der Grein, J. G. Saucedo, A. A. Anand, M. E. Trellet, A. M. J. J. Bonvin, P. Walter, A. J. R. Heck, R. J. de Groot, F. J. M. van Kuppeveld, Inhibition of the integrated stress response by viral proteins that block p-eIF2-eIF2B association. *Nat. Microbiol.* **5**, 1361–1373 (2020).

72. M. Boone, L. Wang, R. E. Lawrence, A. Frost, P. Walter, M. Schoof, A point mutation in the nucleotide exchange factor eIF2B constitutively activates the integrated stress response by allosteric modulation. *Elife* **11** (2022).

73. Q. Hao, J.-M. Heo, B. P. Nocek, K. G. Hicks, V. S. Stoll, C. Remarcik, S. Hackett, L.

1820 LeBon, R. Jain, D. Eaton, J. Rutter, Y. L. Wong, C. Sidrauski, Sugar phosphate activation
1821 of the stress sensor eIF2B. *Nat. Commun.* **12**, 3440 (2021).

1822 74. T. B. Hiyama, T. Ito, H. Imataka, S. Yokoyama, Crystal structure of the alpha subunit of
1823 human translation initiation factor 2B. *J. Mol. Biol.* **392**, 937–951 (2009).

1824 75. E. McEwen, N. Kedersha, B. Song, D. Scheuner, N. Gilks, A. Han, J.-J. Chen, P.
1825 Anderson, R. J. Kaufman, Heme-regulated inhibitor kinase-mediated phosphorylation of
1826 eukaryotic translation initiation factor 2 inhibits translation, induces stress granule
1827 formation, and mediates survival upon arsenite exposure. *J. Biol. Chem.* **280**, 16925–
1828 16933 (2005).

1829 76. B. R. Hearn, P. Jaishankar, C. Sidrauski, J. C. Tsai, P. Vedantham, S. D. Fontaine, P.
1830 Walter, A. R. Renslo, Structure-Activity Studies of Bis-O-Arylglycolamides: Inhibitors of the
1831 Integrated Stress Response. *ChemMedChem* **11**, 870–880 (2016).

1832 77. D. Scheuner, B. Song, E. McEwen, C. Liu, R. Laybutt, P. Gillespie, T. Saunders, S.
1833 Bonner-Weir, R. J. Kaufman, Translational control is required for the unfolded protein
1834 response and in vivo glucose homeostasis. *Mol. Cell* **7**, 1165–1176 (2001).

1835 78. J. Monod, J. Wyman, J. P. Changeux, On the nature of allosteric transitions: A plausible
1836 model. *J. Mol. Biol.* **12**, 88–118 (1965).

1837 79. K. Dev, T. J. Santangelo, S. Rothenburg, D. Neculai, M. Dey, F. Sicheri, T. E. Dever, J. N.
1838 Reeve, A. G. Hinnebusch, Archaeal aIF2B interacts with eukaryotic translation initiation
1839 factors eIF2alpha and eIF2Balpha: Implications for aIF2B function and eIF2B regulation. *J.*
1840 *Mol. Biol.* **392**, 701–722 (2009).

1841 80. Y. Kakuta, M. Tahara, S. Maetani, M. Yao, I. Tanaka, M. Kimura, Crystal structure of the
1842 regulatory subunit of archaeal initiation factor 2B (aIF2B) from hyperthermophilic archaeon
1843 Pyrococcus horikoshii OT3: a proposed structure of the regulatory subcomplex of
1844 eukaryotic IF2B. *Biochem. Biophys. Res. Commun.* **319**, 725–732 (2004).

1845 81. P. Gogoi, S. P. Kanaujia, A presumed homologue of the regulatory subunits of eIF2B
1846 functions as ribose-1,5-bisphosphate isomerase in Pyrococcus horikoshii OT3. *Sci. Rep.* **8**,
1847 1891 (2018).

1848 82. F. A. Fellouse, C. Wiesmann, S. S. Sidhu, Synthetic antibodies from a four-amino-acid
1849 code: a dominant role for tyrosine in antigen recognition. *Proc. Natl. Acad. Sci. U. S. A.*
1850 **101**, 12467–12472 (2004).

1851 83. S. K. Burley, G. A. Petsko, Amino-aromatic interactions in proteins. *FEBS Lett.* **203**, 139–
1852 143 (1986).

1853 84. Y. Sekine, A. Zyryanova, A. Crespillo-Casado, P. M. Fischer, H. P. Harding, D. Ron, Stress
1854 responses. Mutations in a translation initiation factor identify the target of a memory-
1855 enhancing compound. *Science* **348**, 1027–1030 (2015).

1856 85. S. B. Cullinan, D. Zhang, M. Hannink, E. Arvisais, R. J. Kaufman, J. A. Diehl, Nrf2 is a
1857 direct PERK substrate and effector of PERK-dependent cell survival. *Mol. Cell. Biol.* **23**,
1858 7198–7209 (2003).

86. N. H. Kwon, T. Kang, J. Y. Lee, H. H. Kim, H. R. Kim, J. Hong, Y. S. Oh, J. M. Han, M. J. Ku, S. Y. Lee, S. Kim, Dual role of methionyl-tRNA synthetase in the regulation of translation and tumor suppressor activity of aminoacyl-tRNA synthetase-interacting multifunctional protein-3. *Proc. Natl. Acad. Sci. U. S. A.* **108**, 19635–19640 (2011).

87. M. Boyce, K. F. Bryant, C. Jousse, K. Long, H. P. Harding, D. Scheuner, R. J. Kaufman, D. Ma, D. M. Coen, D. Ron, J. Yuan, A selective inhibitor of eIF2alpha dephosphorylation protects cells from ER stress. *Science* **307**, 935–939 (2005).

88. M. D'Antonio, N. Musner, C. Scapin, D. Ungaro, U. Del Carro, D. Ron, M. L. Feltri, L. Wrabetz, Resetting translational homeostasis restores myelination in Charcot-Marie-Tooth disease type 1B mice. *J. Exp. Med.* **210**, 821–838 (2013).

89. C. K. Hahn, C. H. Lowrey, Induction of fetal hemoglobin through enhanced translation efficiency of γ-globin mRNA. *Blood* **124**, 2730–2734 (2014).

90. S. Rai, M. Szaruga, A. P. Pitera, A. Bertolotti, Integrated stress response activator halofuginone protects mice from diabetes-like phenotypes. *J. Cell Biol.* **223** (2024).

91. A. Punjani, J. L. Rubinstein, D. J. Fleet, M. A. Brubaker, cryoSPARC: algorithms for rapid unsupervised cryo-EM structure determination. *Nat. Methods* **14**, 290–296 (2017).

92. T. I. Croll, ISOLDE: a physically realistic environment for model building into low-resolution electron-density maps. *Acta Crystallogr. D Struct. Biol.* **74**, 519–530 (2018).

93. E. F. Pettersen, T. D. Goddard, C. C. Huang, E. C. Meng, G. S. Couch, T. I. Croll, J. H. Morris, T. E. Ferrin, UCSF ChimeraX: Structure visualization for researchers, educators, and developers. *Protein Sci.* **30**, 70–82 (2021).

94. K. Yamashita, C. M. Palmer, T. Burnley, G. N. Murshudov, Cryo-EM single-particle structure refinement and map calculation using Servalcat. *Acta Crystallogr. D Struct. Biol.* **77**, 1282–1291 (2021).

95. A. Subramanian, L. Wang, T. Moss, M. Voorhies, S. Sangwan, E. Stevenson, E. H. Pulido, S. Kwok, R. J. Chalkley, K. H. Li, N. J. Krogan, D. L. Swaney, A. L. Burlingame, S. N. Floor, A. Sil, P. Walter, S. Mukherjee, A Legionella toxin exhibits tRNA mimicry and glycosyl transferase activity to target the translation machinery and trigger a ribotoxic stress response. *Nat. Cell Biol.* **25**, 1600–1615 (2023).

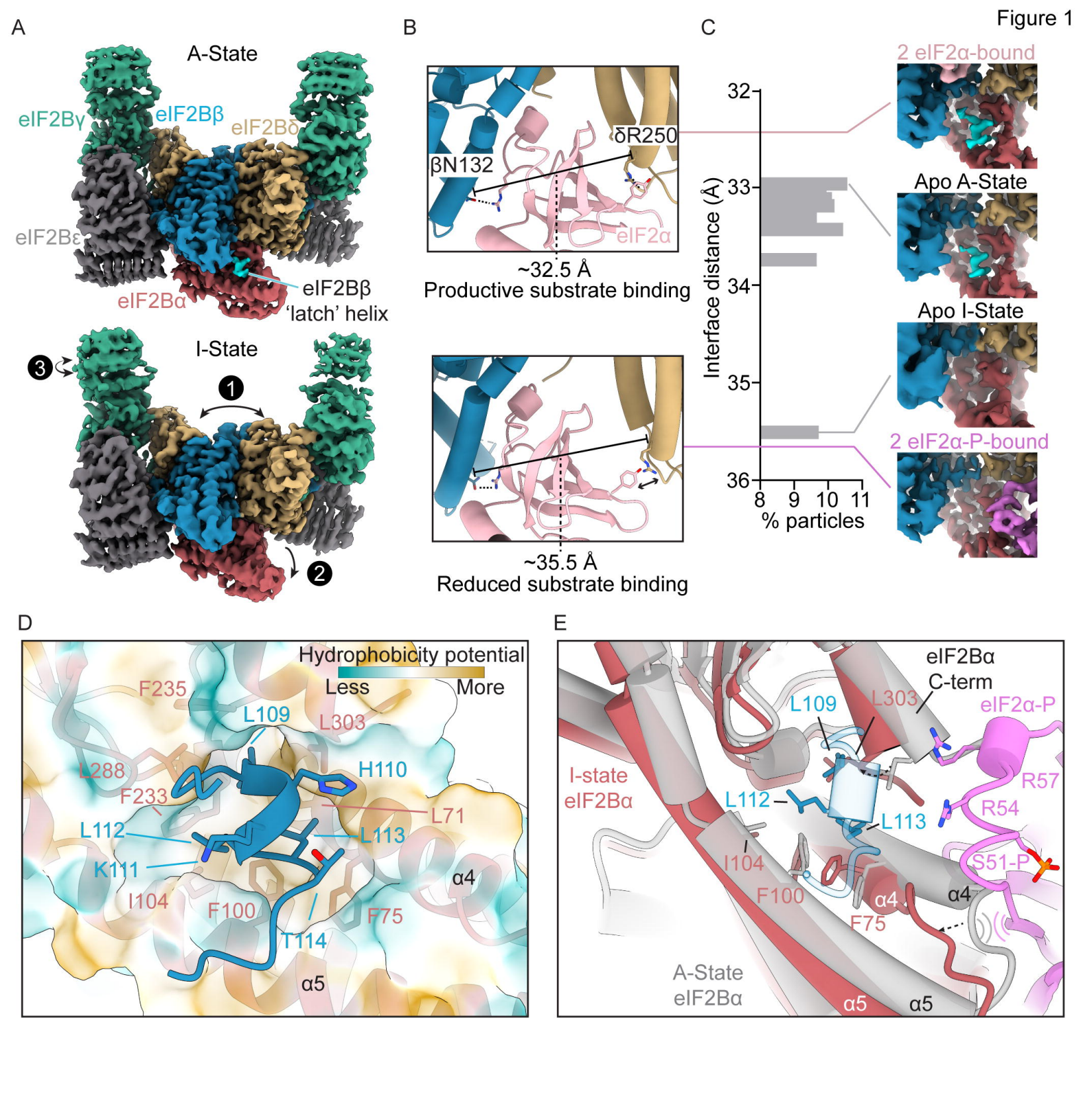
Figure 1
A
A-State
eIF2Bγ
eIF2Bβ
eIF2Bδ
eIF2Bε
eIF2Bα
eIF2Bβ
'latch' helix
I-State
1
2
3
B
βN132
δR250
eIF2α
~32.5 Å
Productive substrate binding
~35.5 Å
Reduced substrate binding
C
2 eIF2α-bound
Apo A-State
Apo I-State
2 eIF2α-P-bound
Interface distance (Å)
32
33
34
35
36
8
9
10
11
% particles
D
Hydrophobicity potential
Less
More
F235
L109
L303
L288
H110
F233
L71
L112
L113
K111
α4
I104
F100
F75
T114
α5
E
eIF2Bα
C-term
L109
L303
eIF2α-P
I-state
eIF2Bα
R57
L112
R54
L113
I104
S51-P
F100
α4
α4
F75
A-State
eIF2Bα
α5
α5

Figure 2

A

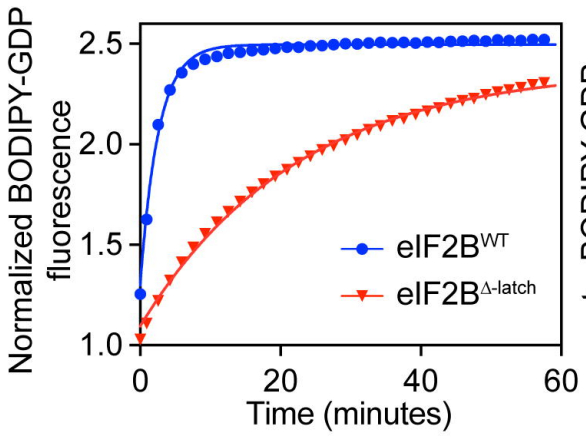

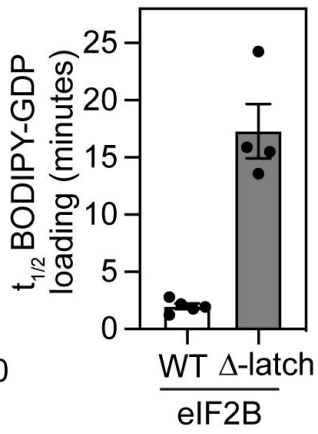

B

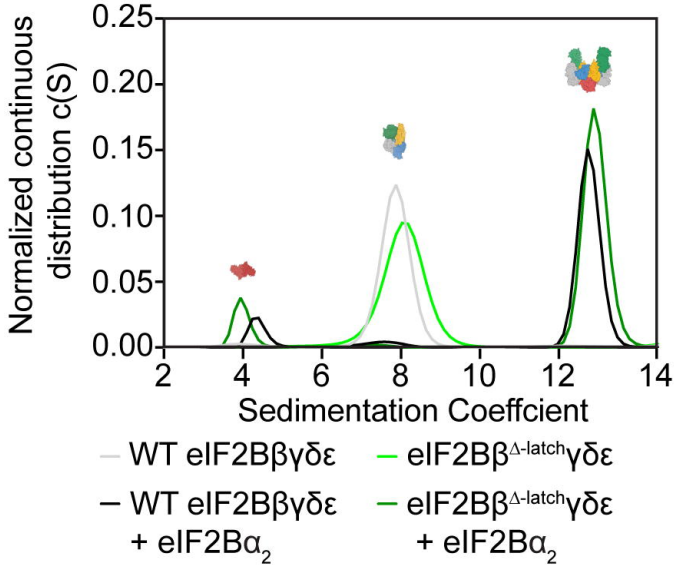

C

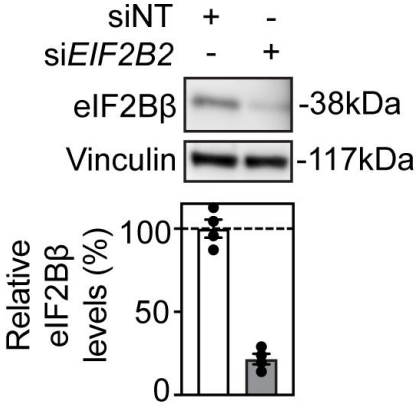

D

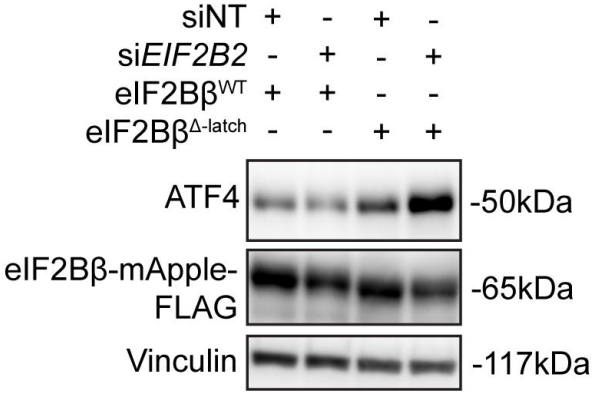

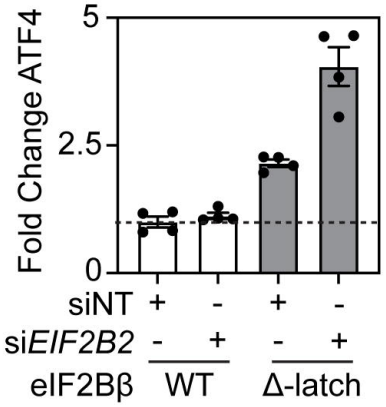

E

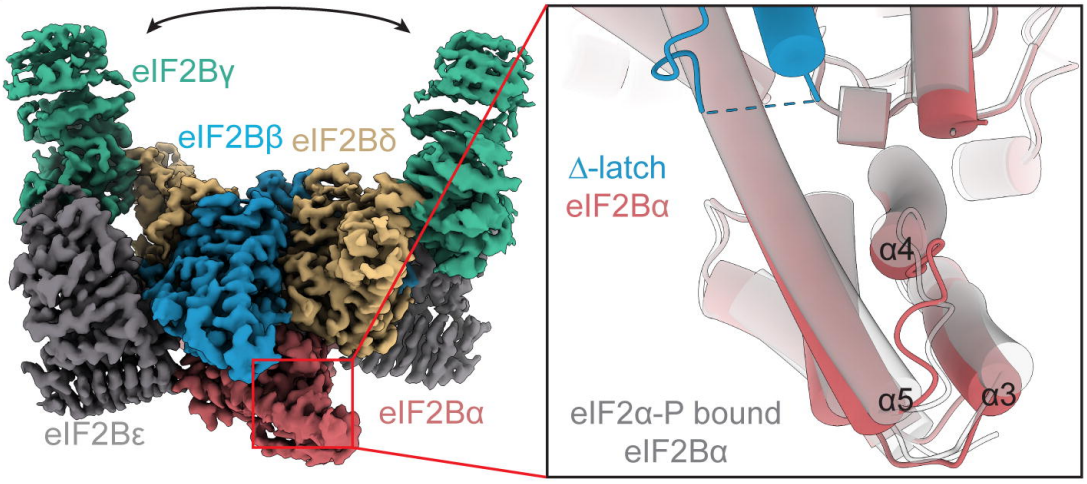

F

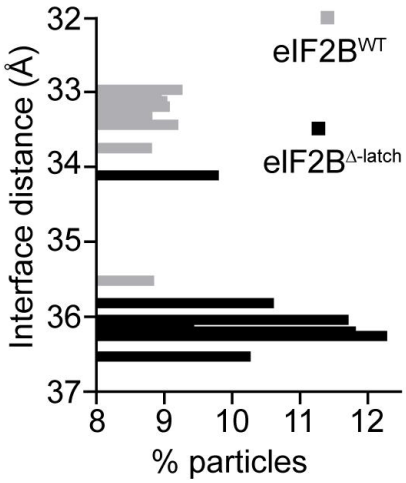

Figure 3

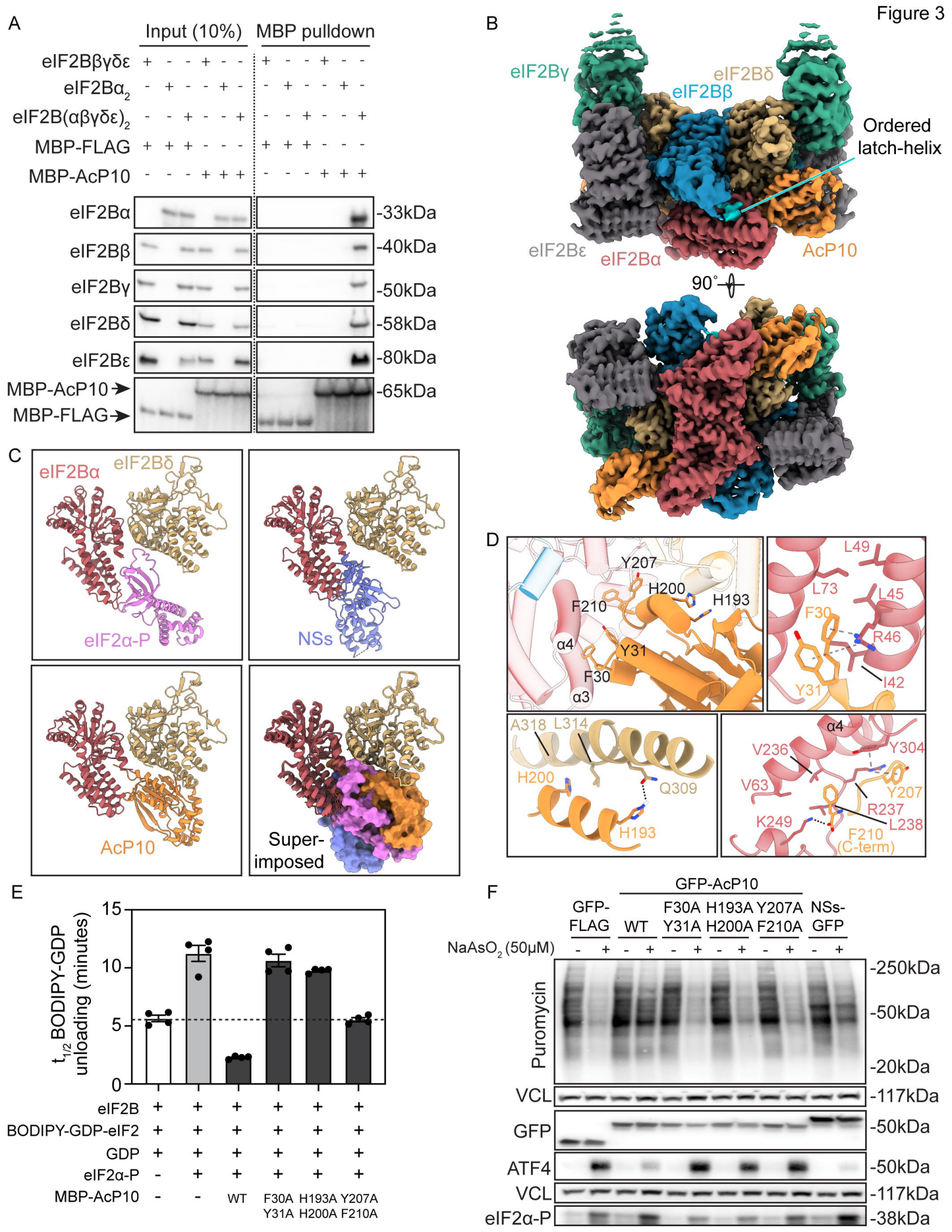
A
Input (10%)
MBP pulldown
eIF2Bβγδε
eIF2Bα2
eIF2B(αβγδε)2
MBP-FLAG
MBP-AcP10
eIF2Bα
eIF2Bβ
eIF2Bγ
eIF2Bδ
eIF2Bε
MBP-AcP10
MBP-FLAG
-33kDa
-40kDa
-50kDa
-58kDa
-80kDa
-65kDa
B
eIF2Bγ
eIF2Bδ
eIF2Bβ
Ordered latch-helix
eIF2Bε
eIF2Bα
AcP10
90°
C
eIF2Bα
eIF2Bδ
eIF2α-P
NSs
AcP10
Super-imposed
D
Y207
H200
H193
F210
α4
Y31
F30
α3
L49
L73
L45
F30
R46
Y31
I42
A318
L314
H200
Q309
H193
α4
V236
Y304
V63
Y207
R237
K249
L238
F210 (C-term)
E
$t_{1/2}$ BODIPY-GDP unloading (minutes)
15
10
5
0
eIF2B
BODIPY-GDP-eIF2
GDP
eIF2α-P
MBP-AcP10
WT
F30A Y31A
H193A H200A
Y207A F210A
F
GFP-AcP10
GFP-FLAG
WT
F30A Y31A
H193A H200A
Y207A F210A
NSs-GFP
NaAsO2 (50μM)
Puromycin
VCL
GFP
ATF4
VCL
eIF2α-P
-250kDa
-50kDa
-20kDa
-117kDa
-50kDa
-50kDa
-117kDa
-38kDa

Figure 4

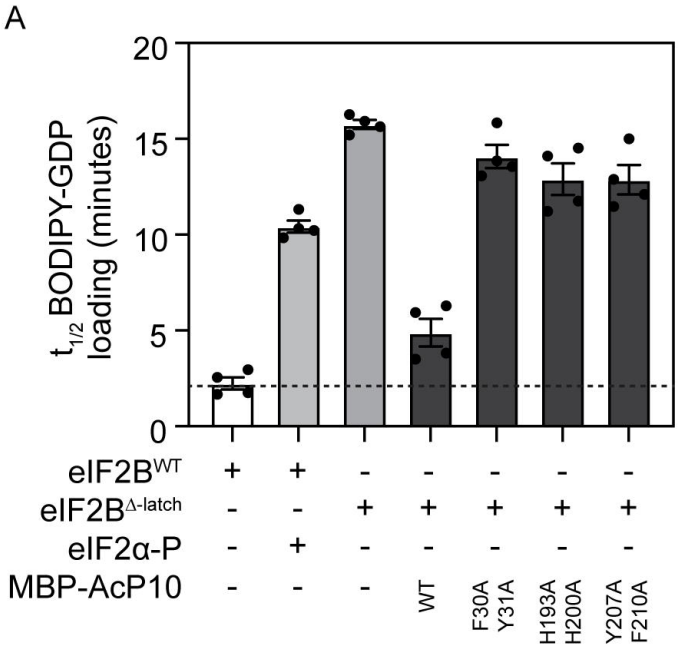
A
$t_{1/2}$ BODIPY-GDP loading (minutes)
20
15
10
5
0
eIF2B^{WT} + + - - - - -
eIF2B$^{\Delta\text{-latch}}$ - - + + + + +
eIF2α-P - + - - - - -
MBP-AcP10 - - - WT F30A Y31A H193A H200A Y207A F210A

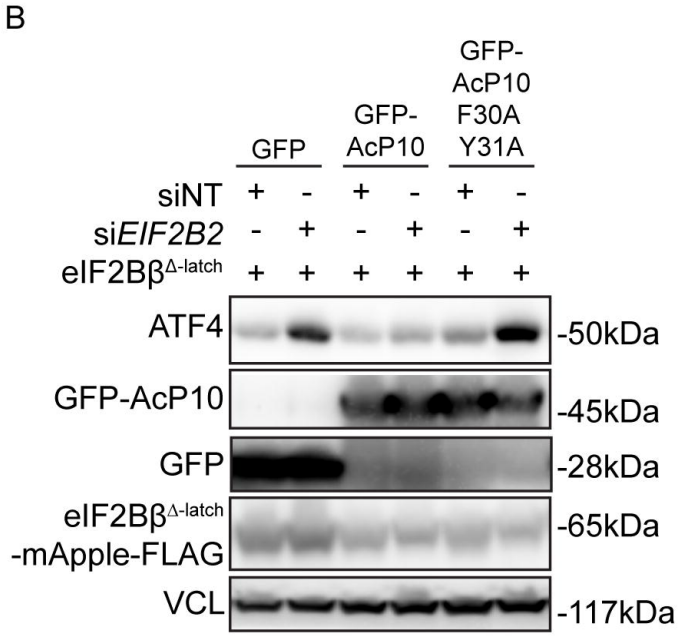
B
GFP
GFP-AcP10
GFP-AcP10 F30A Y31A
siNT + - + - + -
si*EIF2B2* - + - + - +
eIF2Bβ$^{\Delta\text{-latch}}$ + + + + + +
ATF4
-50kDa
GFP-AcP10
-45kDa
GFP
-28kDa
eIF2Bβ$^{\Delta\text{-latch}}$ -mApple-FLAG
-65kDa
VCL
-117kDa

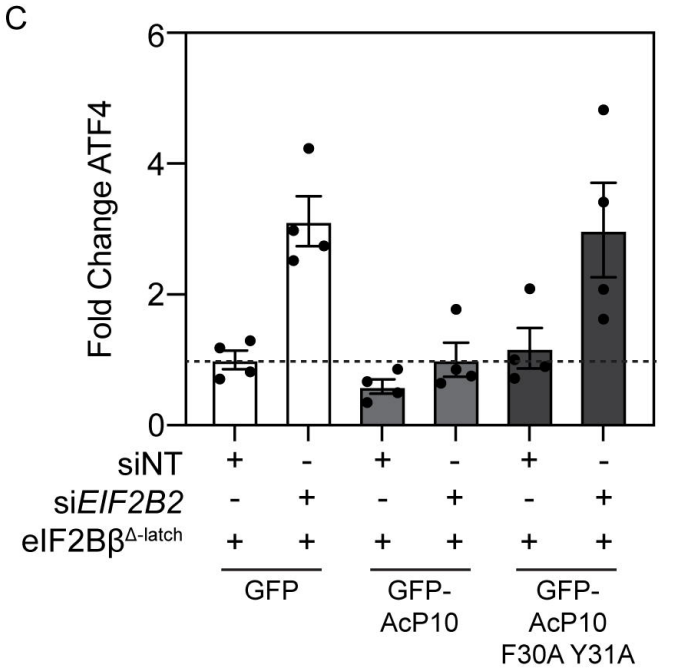
C
Fold Change ATF4
6
4
2
0
siNT + - + - + -
si*EIF2B2* - + - + - +
eIF2Bβ$^{\Delta\text{-latch}}$ + + + + + +
GFP
GFP-AcP10
GFP-AcP10 F30A Y31A

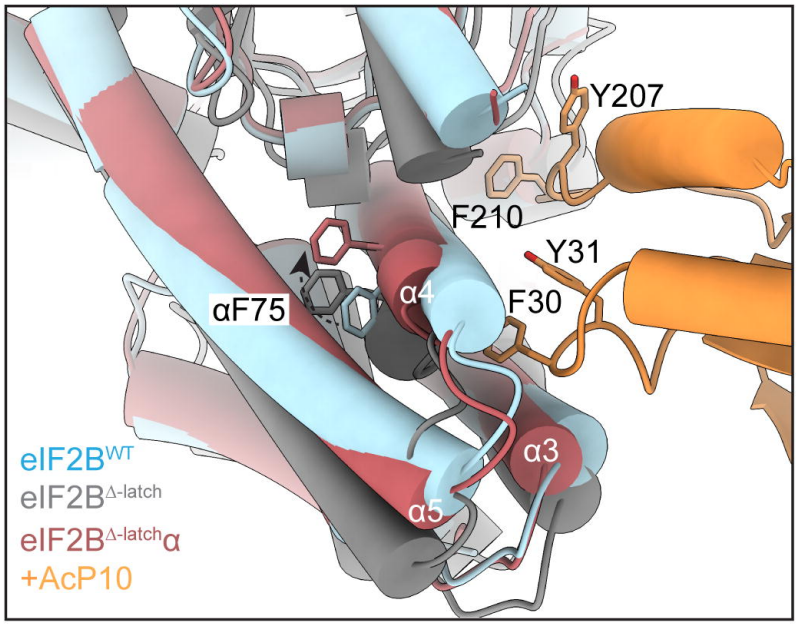
D
Y207
F210
Y31
F30
αF75
α4
α3
α5
eIF2B^{WT}
eIF2B$^{\Delta\text{-latch}}$
eIF2B$^{\Delta\text{-latch}}$α
+AcP10

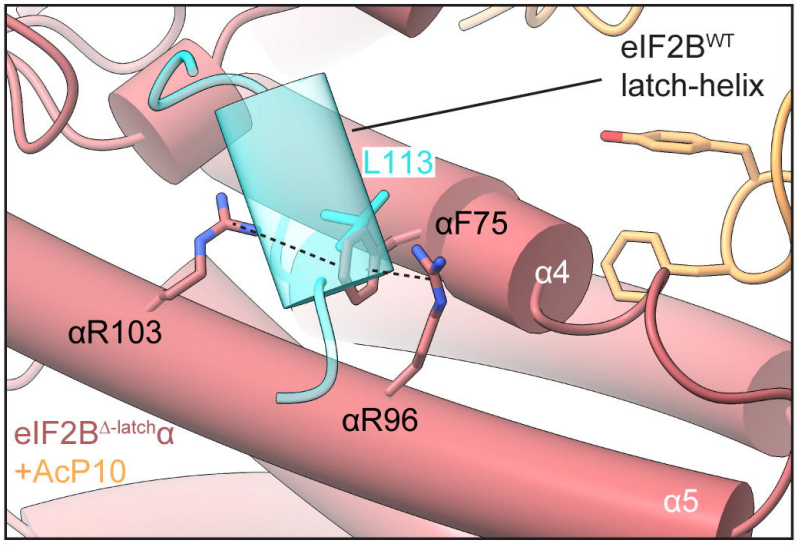
E
eIF2B^{WT} latch-helix
L113
αF75
α4
αR103
αR96
eIF2B$^{\Delta\text{-latch}}$α
+AcP10
α5

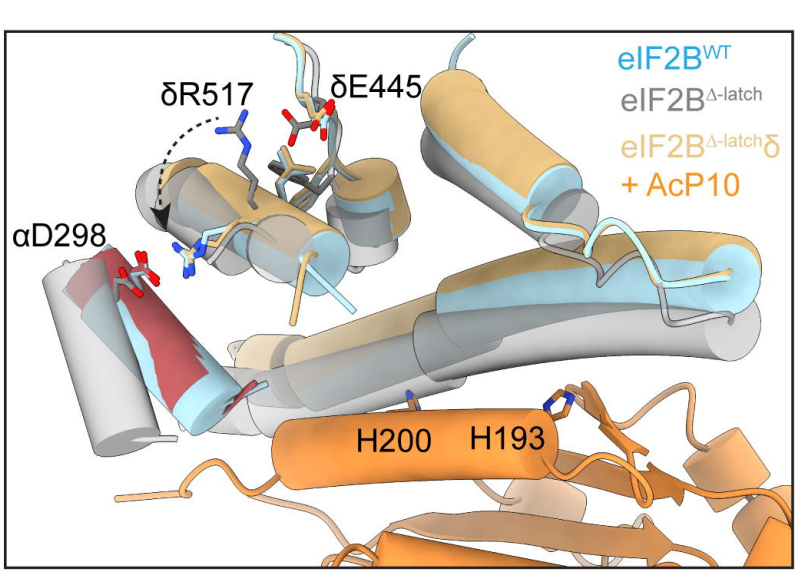
F
δR517
δE445
eIF2B^{WT}
eIF2B$^{\Delta\text{-latch}}$
eIF2B$^{\Delta\text{-latch}}$δ
+ AcP10
αD298
H200
H193

Figure 5

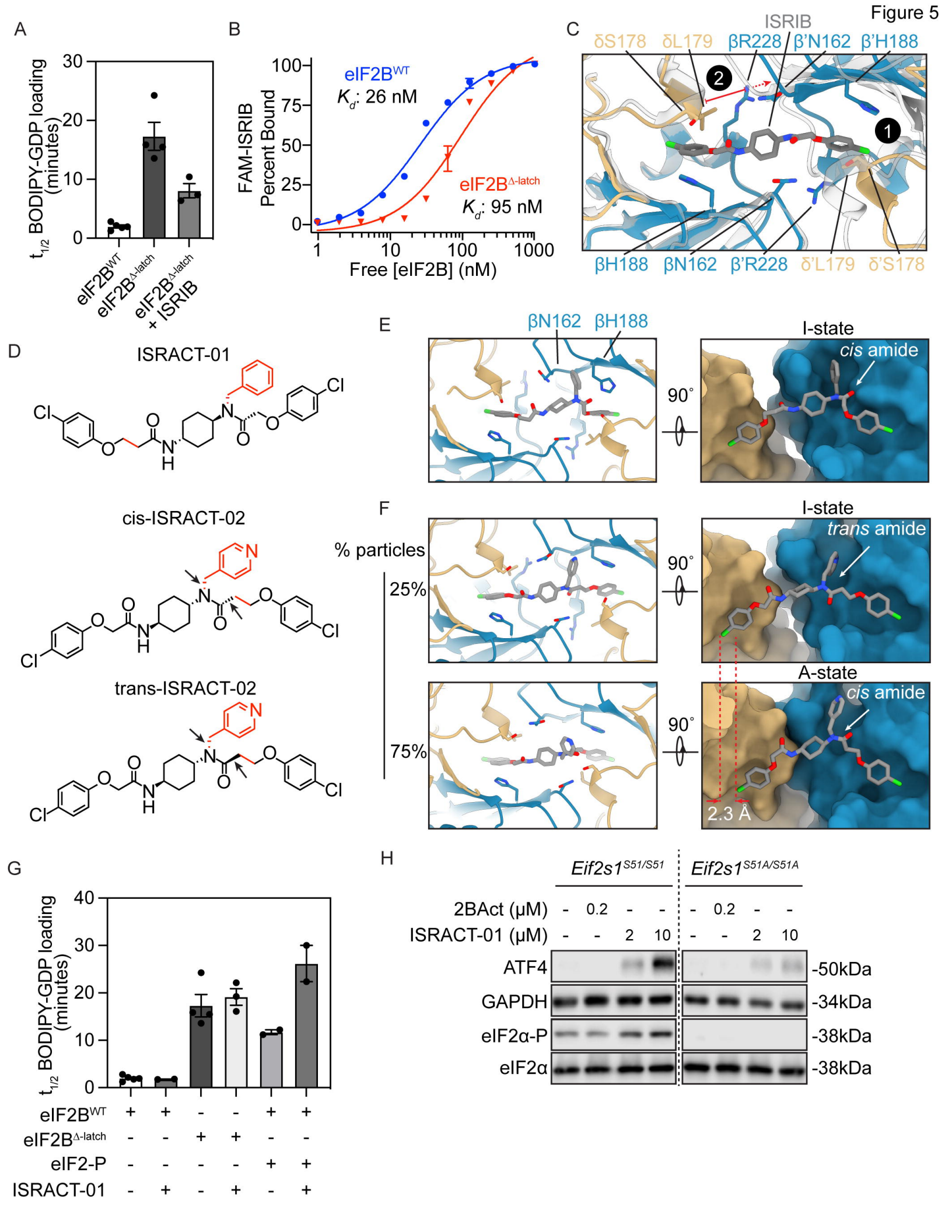
A
$t_{1/2}$ BODIPY-GDP loading (minutes)
eIF2B^WT
eIF2B^Δ-latch
eIF2B^Δ-latch + ISRIB
B
FAM-ISRIB Percent Bound
eIF2B^WT
K_d: 26 nM
eIF2B^Δ-latch
K_d: 95 nM
Free [eIF2B] (nM)
C
ISRIB
δS178
δL179
βR228
β'N162
β'H188
βH188
βN162
β'R228
δ'L179
δ'S178
D
ISRACT-01
cis-ISRACT-02
trans-ISRACT-02
E
βN162
βH188
I-state
cis amide
90°
F
% particles
25%
75%
I-state
trans amide
A-state
cis amide
2.3 Å
G
$t_{1/2}$ BODIPY-GDP loading (minutes)
eIF2B^WT
eIF2B^Δ-latch
eIF2-P
ISRACT-01
H
Eif2s1^S51/S51
Eif2s1^S51A/S51A
2BAct (μM)
ISRACT-01 (μM)
ATF4
GAPDH
eIF2α-P
eIF2α
-50kDa
-34kDa
-38kDa
-38kDa

Figure 6

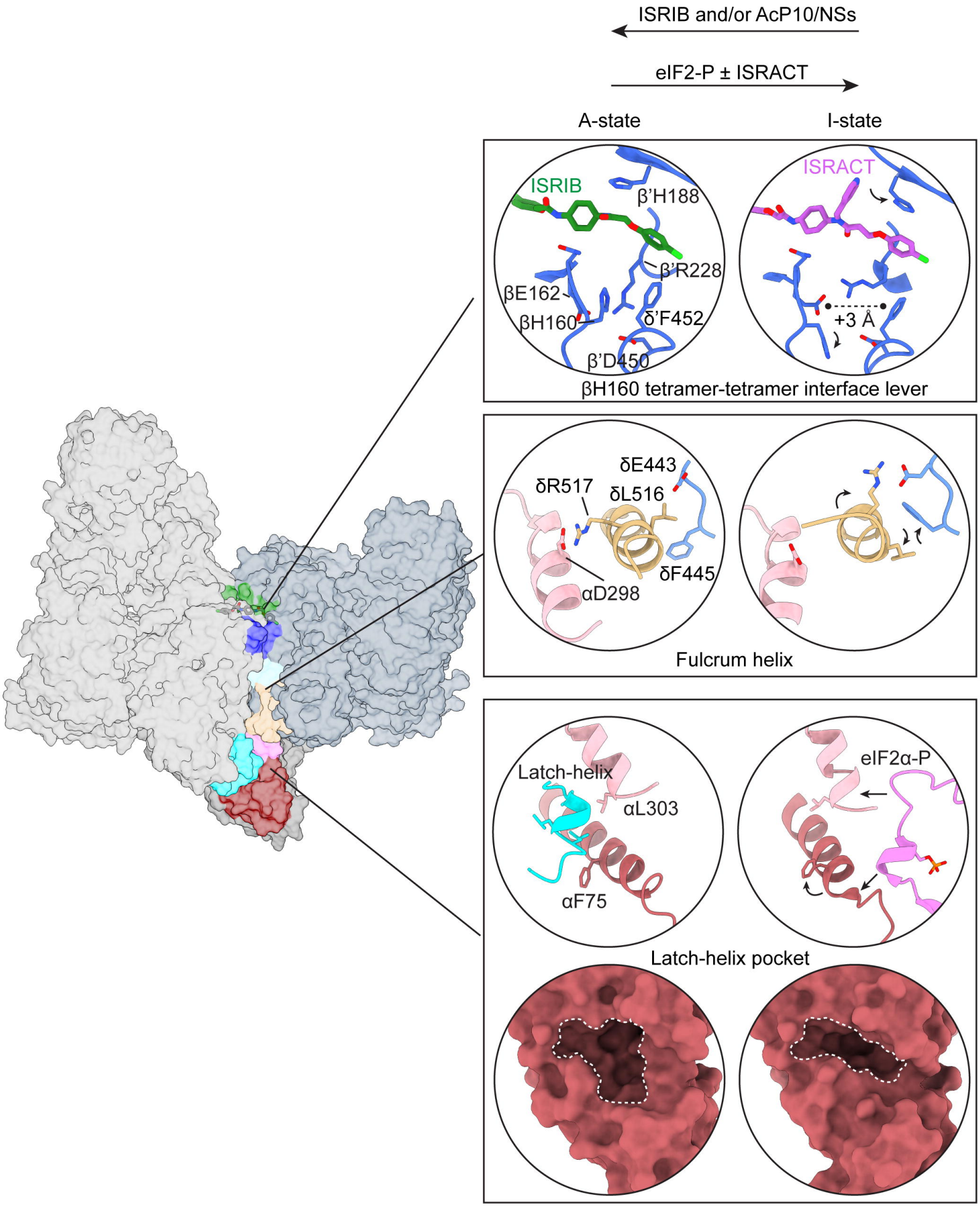
ISRIB and/or AcP10/NSs
eIF2-P ± ISRACT
A-state
I-state
ISRIB
β'H188
β'R228
βE162
βH160
δ'F452
β'D450
ISRACT
+3 Å
βH160 tetramer-tetramer interface lever
δE443
δR517
δL516
δF445
αD298
Fulcrum helix
Latch-helix
αL303
αF75
eIF2α-P
Latch-helix pocket